Theses and Dissertations   1. Thesis and Dissertation Collection, all items

2010-03

Power beaming, orbital debris removal, and other space applications of a ground based free electron laser

Wilder, Benjamin A.

Monterey, California. Naval Postgraduate School

NAVAL POSTGRADUATE SCHOOL

MONTEREY, CALIFORNIA

THESIS

POWER BEAMING, ORBITAL DEBRIS REMOVAL, AND OTHER SPACE APPLICATIONS OF A GROUND BASED FREE ELECTRON LASER

by

Benjamin Wilder

March 2010

Thesis Co-Advisors:	William B. Colson
	James H. Newman

Approved for public release; distribution is unlimited

THIS PAGE INTENTIONALLY LEFT BLANK

REPORT DOCUMENTATION PAGE		*Form Approved OMB No. 0704-0188*
Public reporting burden for this collection of information is estimated to average 1 hour per response, including the time for reviewing instruction, searching existing data sources, gathering and maintaining the data needed, and completing and reviewing the collection of information. Send comments regarding this burden estimate or any other aspect of this collection of information, including suggestions for reducing this burden, to Washington headquarters Services, Directorate for Information Operations and Reports, 1215 Jefferson Davis Highway, Suite 1204, Arlington, VA 22202-4302, and to the Office of Management and Budget, Paperwork Reduction Project (0704-0188) Washington DC 20503.		

1. AGENCY USE ONLY *(Leave blank)*	2. REPORT DATE March 2010	3. REPORT TYPE AND DATES COVERED Master's Thesis

4. TITLE AND SUBTITLE Power Beaming, Orbital Debris Removal, and Other Space Applications of a Ground Based Free Electron Laser	5. FUNDING NUMBERS
6. AUTHOR(S) Benjamin A. Wilder	

7. PERFORMING ORGANIZATION NAME(S) AND ADDRESS(ES) Naval Postgraduate School Monterey, CA 93943-5000	8. PERFORMING ORGANIZATION REPORT NUMBER

9. SPONSORING /MONITORING AGENCY NAME(S) AND ADDRESS(ES) N/A	10. SPONSORING/MONITORING AGENCY REPORT NUMBER

11. SUPPLEMENTARY NOTES The views expressed in this thesis are those of the author and do not reflect the official policy or position of the Department of Defense or the U.S. Government.

12a. DISTRIBUTION / AVAILABILITY STATEMENT Approved for public release; distribution is unlimited	12b. DISTRIBUTION CODE

13. ABSTRACT (maximum 200 words)

When compared to other laser types, the Free Electron Laser (FEL) provides optimal beam quality for successful atmospheric propagation. Assuming the development and deployment of a mega-watt (MW) class, ground or sea based FEL, this thesis investigates several proposed space applications including power beaming to satellites, the removal of orbital debris, laser illumination of objects within the solar system for scientific study, and interstellar laser illumination for communications. Power beaming simulations are conducted within the Satellite Tool Kit (STK) program to determine the frequency of accesses between a satellite and one or more ground stations for multiple orbital profiles. FEL illumination of orbital debris is modeled to determine the thermal effects on a representative aluminum debris particle. FEL illumination of the Lunar and Martian surfaces is modeled to determine the relative laser and solar spectral intensities at these ranges. FEL illumination at interstellar ranges is modeled and discussed to determine our ability to communicate or detect laser communications over interstellar ranges.

14. SUBJECT TERMS Free Electron Laser, FEL, Laser, Power Beaming, Satellites, Orbital Debris, Interstellar Communication, SETI, Laser Illumination, Meteoroid, Asteroid	15. NUMBER OF PAGES 183
	16. PRICE CODE

17. SECURITY CLASSIFICATION OF REPORT Unclassified	18. SECURITY CLASSIFICATION OF THIS PAGE Unclassified	19. SECURITY CLASSIFICATION OF ABSTRACT Unclassified	20. LIMITATION OF ABSTRACT UU

THIS PAGE INTENTIONALLY LEFT BLANK

POWER BEAMING, ORBITAL DEBRIS REMOVAL, AND OTHER SPACE APPLICATIONS OF A GROUND BASED FREE ELECTRON LASER

Benjamin A. Wilder
Lieutenant Commander, United States Navy
B.S., University of South Alabama, 1999

Submitted in partial fulfillment of the
requirements for the degree of

MASTER OF SCIENCE IN PHYSICS

from the

**NAVAL POSTGRADUATE SCHOOL
March 2010**

Author: Benjamin A. Wilder

Approved by: William B. Colson
                      Thesis Co-Advisor

                      James H. Newman
                      Thesis Co-Advisor

                      Andres Larraza
                      Chairman, Department of Physics

THIS PAGE INTENTIONALLY LEFT BLANK

ABSTRACT

When compared to other laser types, the Free Electron Laser (FEL) provides optimal beam quality for successful atmospheric propagation. Assuming the development and deployment of a mega-watt (MW) class, ground or sea based FEL, this thesis investigates several proposed space applications including power beaming to satellites, the removal of orbital debris, laser illumination of objects within the solar system for scientific study, and interstellar laser illumination for communications. Power beaming simulations are conducted within the Satellite Tool Kit (STK) program to determine the frequency of accesses between a satellite and one or more ground stations for multiple orbital profiles. FEL illumination of orbital debris is modeled to determine the thermal effects on a representative aluminum debris particle. FEL illumination of the Lunar and Martian surfaces is modeled to determine the relative laser and solar spectral intensities at these ranges. FEL illumination at interstellar ranges is modeled and discussed to determine our ability to communicate or detect laser communications over interstellar ranges.

THIS PAGE INTENTIONALLY LEFT BLANK

TABLE OF CONTENTS

THIS PAGE INTENTIONALLY LEFT BLANK

LIST OF FIGURES

THIS PAGE INTENTIONALLY LEFT BLANK

LIST OF TABLES

THIS PAGE INTENTIONALLY LEFT BLANK

LIST OF ACRONYMS AND ABBREVIATIONS

AC   Alternating Current

BOL   Beginning of Life

DC   Direct Current

DoD   Department of Defense

EOL   End of Life

FEL   Free Electron Laser

GEO   Geosynchronous Earth Orbit

GPS   Global Positioning System

HEO   Highly Elliptical Orbit

HVAC   High Voltage Alternating Current

JLAB   Thomas Jefferson National Laboratory

kW   kilowatt

Laser   Light Amplification by the Stimulated Emission of Radiation

LEO   Low Earth Orbit

LINAC   Linear Accelerator

MA   Mean Anomaly

Maser   Microwave Amplification by the Stimulated Emission of Radiation

MEO   Medium Earth Orbit

MMOD   Micrometeoroid and Orbital Debris

MW   Megawatt

NASA   National Aeronautics and Space Administration

PRF   Pulse Repetition Frequency

RF   Radio Frequency

SLAC   Stanford Linear Accelerator

SNR   Signal to Noise Ratio

SSP   Sub-Satellite Point

STK   Satellite Tool Kit

RAAN   Right Ascension of the Ascending Node

THIS PAGE INTENTIONALLY LEFT BLANK

LIST OF SYMBOLS

$\vec{A}$	Vector Potential for Optical Field
A	Area
A_s	Beam Spot Size (Area)
a	Dimensionless optical field
a_o	Initial optical field amplitude in undulator
a_s	Orbital Semi-major Axis
B_m	Undulator Magnetic Field Strength
$\vec{B}_L$	Laser's magnetic field
$\vec{B}_{op}$	Optical magnetic field
$\vec{B}_u$	Undulator magnetic field
B_{rms}	Root Mean Squared Value of the Undulator Magnetic Field
C_n	refractive index structure coefficient
C_T	Temperature structure parameter
c	Speed of light
e	Charge of an electron
E	Optical field magnitude
$\vec{E}_L$	Laser's electric field
$\vec{E}_{op}$	Optical electric field
h	Specific angular momentum
j	Dimensionless current density
$J_{\perp}$	Transverse current density
k	Optical wave number
k_o	Undulator magnetic wave number
K	Dimensionless undulator parameter
L	Undulator length
m_e	Mass of an electron
N	Number of undulator magnetic periods
$n \ / \ n_o$	Index of refraction $ / $ Initial index of refraction
P	Power
P_P	Atmospheric Pressure
P_{dp}	Power radiated by a dipole
p_o	Maximum value of the dipole momentum
R	Range
R_S	Stagnation Range

R_{sun}	Solar Radiated Power
$R_{Sun\lambda}$	Solar Monochromatic Radiated Power
r	Range from the Earth's center to satellite center
$\hat{r}$	Unit vector pointing in the direction of r
T / T_o	Temperature / Initial temperature
T_{sat}	Orbital Period
t	Time
v	Electron beam phase velocity
v_e / v_o	Electron velocity / Initial electron phase velocity
v_d	Electron drift velocity
v_{sat}	Satellite velocity
w	Beam radius at the target
w_o	Beam radius at the waist
x	Orthogonal distance from the beam axis
z	Range from the optical beam waist to target
z	Rayleigh range
z_u	Distance along the undulator axis
$\vec{\beta}$	Dimensionless electron velocity
β_s	Angle between a satellite's orbital plane and the sun
β_z	Z component of the Dimensionless electron velocity
$\beta_\perp$	Transverse component of $\vec{\beta}$
γ	Lorentz factor
ε	Emissivity
λ_o	Magnetic period length
λ	Optical wave length
ψ	Time varying optical phase
ϕ	Initial optical phase
ρ / ρ_o	Density / Initial Density
ρ_e	Electron beam density
σ	Stefan-Boltzman Constant
τ	Dimensionless time
μ	Earth's gravitational parameter
μ_o	Permeability of free space
ω_f	Frequency of incident radiation
ω_{op}	Optical frequency
ζ / ζ_o	Electron beam phase / Initial electron beam phase
θ	Optical beam divergence angle

ACKNOWLEDGMENTS

This work and my life as a whole are dedicated to my Creator for bringing me into this world and for filling it with the wonderful blessings of family, friends, mentors, and heroes. The first among these is my wife, Nicole. Her beauty, grace, and elegance are only surpassed by her compassion, good humor, and warm spirit. For her, I wake each day striving to be a better man. I thank my son, Jacob, for his giving heart and noble nature. From his youngest days, Jacob has shown empathy for others that I can only hope to emulate. I thank my son, Justin, for showing me how to "seize the day" and suck the marrow out of life. I am truly blessed to have witnessed a soul with such a passion for life, growth, and humor despite adversity. I thank my daughter, Katie, for her vivacity and adventurous spirit. She is always the first to forge ahead through a scary wood or to chomp down on a strange new food. I try to approach the opportunities in my life with the same bravado and positive nature. I thank my daughter, Meghan, who as the youngest of our clan was born into a tempest of noise and activity, but somehow stands above it all at only 30 inches tall. I hope to learn her patience and resiliency. I thank my mother, Judy, for rising above the challenges in her life and providing me with an unlimited future. She gave me the self-confidence to reach for my dreams and the grounding to work hard for them. She is the wind beneath my wings. I thank my father, Richard, for caring enough to stay in the ring with me. He has taught me that the most important thing a father can give is himself and his time, and as a man, I could have no better role model in life. He is my hero.

I thank my mother-in-law, Beth, for dropping everything to help our family through the seizures, the surgeries, the hurricane, and the challenges of a lifetime. I can't imagine the financial and personal difficulties that she must have faced to help my family to grow and thrive. She is the glue that keeps us all together. I thank my father-in-law, Kevin, for being a quiet and constant companion in my adult life. As I picked up the pieces of my life after Katrina wearing a mask of strength, his character, fortitude, and

devotion to our family helped to keep me on my feet. What I say with words, he says through actions—and I'm proud to have him and his life as an example for my children. He is the rock that I built my family on.

I thank my sister, Erica, for her love and support over the years. I have loved her since the first time that Mom and Dad let me hold her; but lately, I am overcome with pride at the woman, wife, and mother that she has become. Her willing love for and devotion to Connor, her strength in recovering from Katrina, and her limitless faith are a testament to the content of her character. I thank my sister-in-law, Amanda, for her love, dedication to family, and good humor. She is the only woman I know, without kids of her own, who can and/or would "pinch hit" for a mother of four on a moment's notice. She is an amazingly talented and driven woman, a role model for my daughters, and a true friend.

Of my friends, I thank my cousin and blood-brother, Ben #2, for providing me a lifetime of friendship and a role model in being a husband, father, and military officer. I thank my friend, Sean, for his unfaltering friendship, constant guidance, and his battle rifle. He is the most professional officer that I have ever met. I thank my brother-in-law, Chris, for his humor, character, and willingness to listen. He has buoyed my soul during the dark times and lifted me higher in the good times, often by just being there to listen. I thank my brother-in-law, Scott, for his humor, work ethic, and dedication to my sister. Seeing his infinite character reflected in Connor and in Erica as she grew into womanhood, I am amazed at his soft-spoken ability to influence others to better themselves. I hope to be half the man, husband, and parent that he has been.

Of my mentors, I thank Professor William "Archimedes" Colson for his unmatched expertise, unlimited patience, and unfaltering confidence in my ability. No matter the place or time of day, he always had the time to help and provide an encouraging word. I thank Professor James Newman for his knowledge, "sea stories," and constant support of my studies. I thank Professor Joe Blau for making time outside of class and for his positive nature. I thank Professor Brett Borden for his dedication to teaching and his enthusiastic support of my future.

I. INTRODUCTION

The development of high average power free electron lasers (FELs), with their nearly unlimited range and excellent beam quality, offers the potential to revolutionize the exploration and utilization of space. This thesis will investigate the utilization of an FEL for power beaming to satellites, orbital debris clearance, and illuminating extraterrestrial bodies for scientific study or communication. Additionally, recently published Chinese forays into anti-satellite warfare suggest other, offensive and defensive, military applications of high energy lasers, such as blinding electro-optical satellites, engaging ballistic missiles, or damaging enemy satellites in wartime. Implementation of such capabilities would violate international law and treaties, and they will not be explored here.

A high average power laser could be used to beam power over large distances to Unmanned Aerial Vehicles (UAVs), satellites, or even a future lunar base, but this thesis will focus primarily on satellite applications. For satellites, the loss of solar power during eclipse often forces the implementation of a restrictive power budget, and additional power provided by a high energy laser could affect the operation and design of future spacecraft. Utilizing specially designed photovoltaic cells, this method could power satellites with much greater efficiency than current solar cell technology. It would remain impractical for steady power applications and might only be useful or significant for emergent or wartime utilization.

By combining a high power laser with advanced sensors, a system can be deployed that finally matches the range and speed of its sensors allowing for rapid illumination of multiple targets. If applied to the growing problem of orbital debris, a high-peak power laser could be used to apply a small change in orbital velocity over several orbits. By changing the orbital profile to lower the perigee and, therefore, increasing atmospheric drag, the laser could greatly decrease the time it takes for debris to reenter. Similarly, a high average power FEL could melt and then vaporize some of

the debris material, resulting in a smaller and less dangerous particle and making near-Earth space safer for satellites and manned missions.

When applied to extraterrestrial illumination, i.e., the illumination of any non-terrestrial natural body such as the moon, other planets, comets, asteroids, or even interstellar dust, a high average power laser allows for the transmission of long and complex pulses with good coherence, leading to improved scientific observation of these bodies over a specific bandwidth. If applied to the search for extraterrestrial intelligence, a high average power, continuous wave laser could be used to send signals to extra-solar planets that have the potential to support life. Despite the many difficulties of interstellar transmission, the coherence, power spectral density, and directionality of a laser beam provides the best opportunity for successfully transmitting a discernable and uniquely intelligent signal across interstellar distances.

Supporting the applications listed above, the first four chapters in this thesis review the history and basic theories of laser applications, FELs, laser propagation, and orbital mechanics. This background and theory is intended to lay a foundation of knowledge and understanding for the analyses performed in subsequent chapters while highlighting any specific results or differences that apply to a high power FEL. The thesis begins with a basic discussion of laser history in Chapter I, followed by a description of the specific qualities, components, and understanding of an FEL in Chapter II. Chapter III discusses the propagation of an electromagnetic wave across free space and through a turbulent medium, e.g., Earth's atmosphere. Chapter IV reviews orbital mechanics, describes commonly used orbits, and discusses the perturbative forces that act on an orbiting object.

Chapter V examines the use of a high power FEL for beaming energy to LEO satellites. Assuming the successful development and deployment of a high power FEL, operational concepts for power beaming are explored and simulated to investigate the possible utilization, costs, and benefits of a deployed ground or sea-based infrastructure. Chapter VI proposes the use of a high power FEL for the clearance of orbital debris. A discussion of the debris types and the motivation for removal is followed by calculations of laser energy required to vaporize a significant portion of the debris material. Chapter

VII investigates the utilization of a high power FEL for Lunar or Martian illumination and possible applications in sending interstellar communications. Building on the propagation equations outlined in Chapter III, calculations of the beam spot size, bandwidth, intensity, and comparisons to solar illumination at the target are detailed. Similar calculations are included for interstellar communications with the goal of transmitting a clear and unique signal to extra-solar planets that might harbor life.

The potential applications of high energy lasers in the not-so-distant future are exciting, and each application abounds in interesting scientific theory, engineering challenges, and detailed operational considerations. For a naval officer, the militaristic applications are especially intriguing due to the laser weapon's ability to match the speed and efficacy of its radar sensor, i.e., the weapon can engage and destroy missiles at nearly the same range that the sensor acquires them and the engagement takes approximately two seconds instead of ~45 seconds. This thesis performs an initial theoretical and operational analysis of a few near-term and several long-term applications of the next generations of FELs.

A. LASER HISTORY

Despite their deep entrenchment in our popular culture and science fiction, the concept of Light Amplification by the Stimulated Emission of Radiation (LASER) and directed energy weapons in general are very recent scientific developments. Although some reports claim that the Greek scholar Archimedes utilized large mirrors to set fire to enemy ships, the first verifiable uses of directed energy were entirely scientific [1]. In the late 1800s and early 1900s, the invention of the cathode ray tube and later the discovery of the medical utility of X-rays prompted a burst in scientific exploration into directed energy. The first true laser wasn't developed until the mid-20th century, and battlefield lasers are only now becoming commonplace.

Perhaps the most important discovery leading to the development of functional maser and laser devices was the principle of stimulated emission proposed by Albert Einstein in his 1917 paper "On the Quantum Theory of Radiation." Prior to Einstein's paper, the scientific community only recognized two fundamental and limited

interactions between a photon and an atom in one of multiple available (but discrete) energy states. In the first case, "absorption," the atom was initially in a lower energy state when it absorbed a photon with exactly the right amount of energy to move the atom into a higher, "excited" state. In the second case, "spontaneous emission," the atom was initially in a higher energy state when it spontaneously dropped to a lower energy state by emitting a photon whose energy exactly matched the difference in states.

Detailing a third alternative in his paper, Einstein postulated that if a photon with the appropriate energy arrived when the atom was in the higher energy level, it could stimulate the atom to emit another photon of the same energy, and drop to the lower energy state. Although pivotal to the eventual development of the laser, this process of "stimulated emission" was initially ignored by most scientists because it seemed to be a very unusual event. The primary hurdle to the scientific exploration of Einstein's stimulated emission was the concept of "thermodynamic equilibrium." For most of the early 1900s, scientists believed that in any population of atoms most physical and chemical processes would quickly reach steady-state equilibrium, thereby limiting the proportion of atoms that exist in a higher energy state. With most atoms confined to a minimum energy (ground) state, the process of absorption would dominate any contributions from stimulated emission, and lasing would be impossible.

Despite these conceptual limitations, scientists of the 1930s learned to utilize microwave cavities to generate coherent radiation with an electron beam which prompted the rapidly developing radar technologies of World War II. The microwave tube utilized a beam of free, non-relativistic electrons and a closed resonant cavity to produce a fairly long wavelength electromagnetic beam with good efficiencies. Still, the physical limitations of their microwave tubes meant that shorter wavelengths would remain out of reach for the foreseeable future, so most researchers focused their efforts on microwave wavelengths and technologies. Building on the process of stimulated emission and his experience with surplus military microwave equipment, Charles Townes created the first "ammonia" maser in 1954 at Columbia University. This maser—short for Microwave Amplification by the Stimulated Emission of Radiation—directed a beam of excited

ammonia molecules into a cavity resonant at the 24 GHz frequency of the ammonia transition to couple the emitted spontaneous radiation with the ammonia molecules and thus provide more amplification [2].

In order to generate coherent radiation at shorter wavelengths, scientists devised a way to pump bound electrons in an open optical resonator into excited states within a crystal medium, and in 1960, while working at Hughes Research Laboratories, Theodore Maiman produced a small flash-lamp pumped ruby laser at 694nm (a wavelength in the deep red) [2]. Further developments in gas, dye, chemical, and other exotic lasing mediums followed until in the 1970s, scientists at Stanford developed the first free electron laser (FEL) which utilized a relativistic beam of electrons as a lasing medium, thus avoiding the traditional thermal limitations of a static medium [3]. Building on a 1951 proposal and later demonstrations by Hans Motz in the millimeter wavelengths, John M. J. Madey proposed and developed the first FEL, which produced optical waves by passing an electron beam and an external carbon-dioxide "seed" laser pulse through a series of alternating magnetic fields [2].

Since their initial development in the 1950s, lasers have become commonplace devices in every home, office, and lab; with applications ranging from industrial welding to laser hair removal. However, it is often too easy to overlook the scientific and technological significance of their invention. In their over half-century of existence, lasers have expanded the boundaries of coherent electronics from the millimeter wavelength range, using microwave tubes and transistors, to include the submillimeter, infrared, visible, ultraviolet, and portions of the X-ray spectrum [4]. Scientists and engineers now have access to coherent radiation at frequencies up to a million times higher (and wavelengths up to a million times shorter) than previously possible.

B.   BASIC LASER CONCEPTS

In the broadest sense, a laser could be defined as any device that generates or amplifies coherent light through the process of stimulated emission. However, this definition requires an equally broad definition of the term "light" due to the wide spectrum of wavelengths accessible to modern lasers (from X-ray to microwave).

Generally, laser light exhibits remarkable coherence, spectral purity, directionality, and intensity, but specifically, there are three essential elements to every laser: a gain medium, a pumping process, and an optical feedback process.

1. Essential Elements

While all lasers combine these three basic elements to generate or amplify an optical wave, each element or process can be constructed in a variety of ways. The lasing medium can be any appropriate collection of atoms, molecules, ions, electrons, or even a semi-conductive crystal with multiple quantum energy states. The pumping process must have some way of repeatedly exciting the medium into a higher energy state to replenish the laser between passes. The optical feedback process must amplify a beam of radiation as it passes through the lasing medium over one long pass (as in a laser amplifier) or multiple repeated passes (as in a laser oscillator, shown in Figure 1) to maximize the interaction between the optical wave and the gain medium.
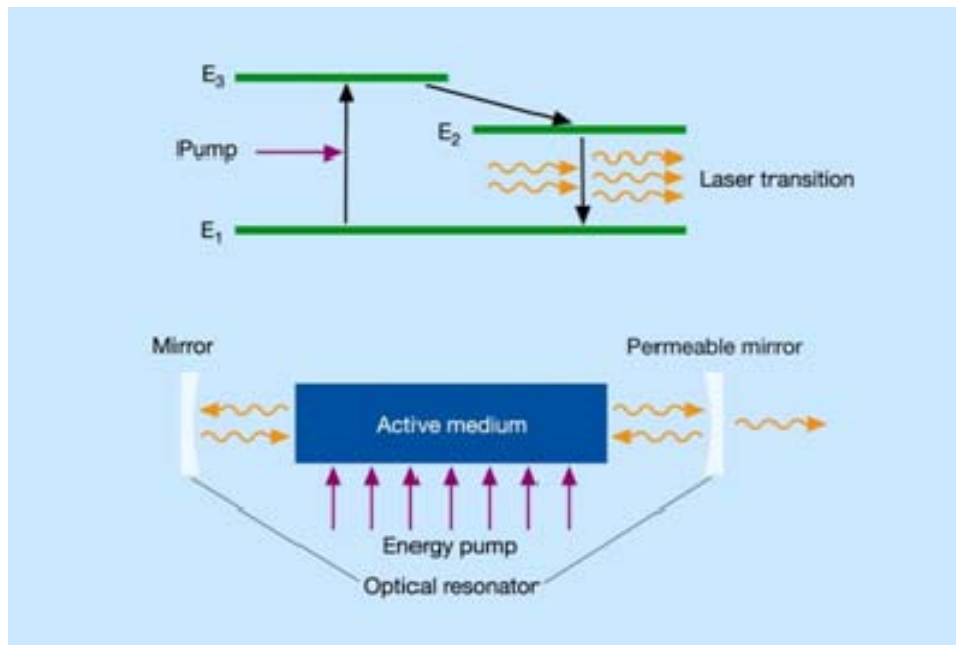
Figure 1.   Basic Schematic of a Conventional Laser. From [5]

2.   Population Inversion

The stimulated transition process within a gain medium can either absorb or amplify an applied optical signal. In absorption, atoms initially in the lower state are stimulated by an applied signal to transition upward to the higher state; in amplification, atoms initially in the higher state are stimulated to make the transition downward to the lower state. The stimulated transition probability produced by an applied signal is exactly the same in both directions. Therefore, although both processes take place simultaneously, the net flow of stimulated transitions is always from the energy level with a larger population to the energy level with a smaller population. In order to produce laser amplification and to overcome the thermodynamic equilibrium described above, the pumping process must create a condition called a *population inversion*, in which more atoms are in the higher energy level than are in the lower energy level [4].

3.   The Pumping Process

As shown in the upper portion of Figure 1, most conventional lasers utilize the difference in quantum energy states within their gain medium to produce an optical beam with a narrow wavelength range. By "pumping" electrons into the higher energy states, the optical output of both spontaneous and stimulated emission becomes highly predictable, but not perfectly so, due to small differences in the allowed energy levels. In modern lasers, pumping can be accomplished through many familiar and sometimes exotic methods such as chemical reactions, gas discharges, direct electrical pumping, and nuclear pumping. In most lasers, however, the pumping process occurs through the use of optical pumping methods such as the use of flash lamps or even other lasers.

4.   Coherence

As an optical signal is applied to the laser's gain medium, the electromagnetic fields within the wave cause a resonant response of the atomic wave functions to the applied signal. In a classical sense, each atom of the medium undergoes internal oscillations that follow the driving optical signal coherently, matching it precisely in amplitude and phase. As these oscillating atoms reradiate, the fields reradiated by the

individual atoms combine with the applied fields to produce absorption or amplification in a manner that is both spatially and spectrally coherent.

5. Laser Limitations

Due to the limitations of the lasing medium, a typical laser is limited in the range of available output wavelengths, the width of the output optical spectrum, the total output power, and the overall system efficiency. The output wavelengths are limited because there are a limited number of transitions available in a particular gain medium. The width of the output optical spectrum is affected by many slight variations in allowable quantum-mechanical energy states. The optical output power is limited because of the thermal stresses within the gain medium. Thermal effects within the gain medium can decrease the optical beam quality, and at extremely high powers, the growing thermal stresses can cause damage to the medium or cavity and thereby result in a catastrophic failure of the laser. The overall system efficiency is limited in two ways: first, waste heat deposited in the medium must be removed; and second, the pumping process can also excite unwanted energy transitions within the medium. These unwanted energy transitions produce photons outside of the desired output range, which can contribute to the laser's thermal loads or degrade the overall beam quality.

II.   THE FREE ELECTRON LASER

Although largely differentiated from other classes of laser in size, function, and complexity, the FEL still combines the three basic components of a laser to generate and amplify coherent light. In an FEL, the lasing medium is actually a high energy beam of relativistic electrons traveling through an undulator at nearly the speed of light. Avoiding the thermal complications that plague other laser types in their media, the FEL capitalizes on the principle of synchrotron radiation to deliver a high power laser beam limited in power primarily by the thermal properties of the laser optics. With this advantage, FELs have the potential to be much more powerful than other classes of laser once FEL technologies are fully developed. Likewise, by freeing themselves of the limited atomic transitions within a standard medium, FELs can be easily tuned over a broad range of wavelengths.

The pumping process in an FEL is provided through the addition of radio frequency (RF) accelerating cavities that continually raise the electron beam to relativistic energies. These RF cavities and the large cooling systems needed to maintain them are the greatest contributors to the added size, weight, and complexity of FEL design. The cavities can add significantly to the "wall-plug" efficiency of the complete system by recapturing most of the energy of the returning electron beam when the beam is recirculated.

Much like other laser types, the optical feedback process in an FEL can occur in both the amplifier and oscillator designs. In the amplifier, a long undulator maximizes the interaction time between the electron beam and light generated either by a seed laser or by spontaneous emission. In the oscillator, the optical feedback is provided by a resonator formed by two mirrors bracketing the undulator in order to maximize the light and electron beam interaction.

A.   FEL COMPONENTS

In terms of the basic laser theory described above, the FEL is categorized as a laser because it consists of an electron beam used as a gain medium, a pumping method of accelerating these electrons to relativistic energies, and a method to provide optical feedback and amplification through prolonged interaction between the electron beam and the optical wave. These statements are simplified to connect basic lasing principles to the FEL, but in terms of actual components, there are two general FEL designs: the oscillator and the amplifier. As shown in Figure 2, the basic components of an oscillator FEL design are: an electron source, an electron accelerator, undulator magnets, resonator mirrors, and an electron dump. In contrast, the amplifier design has an electron source, an electron accelerator, a longer undulator, a seed laser, and an electron dump. As the names imply, the primary difference between oscillator and amplifier designs is the removal of the optical resonator; therefore in an amplifier, all of the laser's gain must occur in a single pass through the undulator, and the initial optical pulse is often provided by the addition of a seed laser.
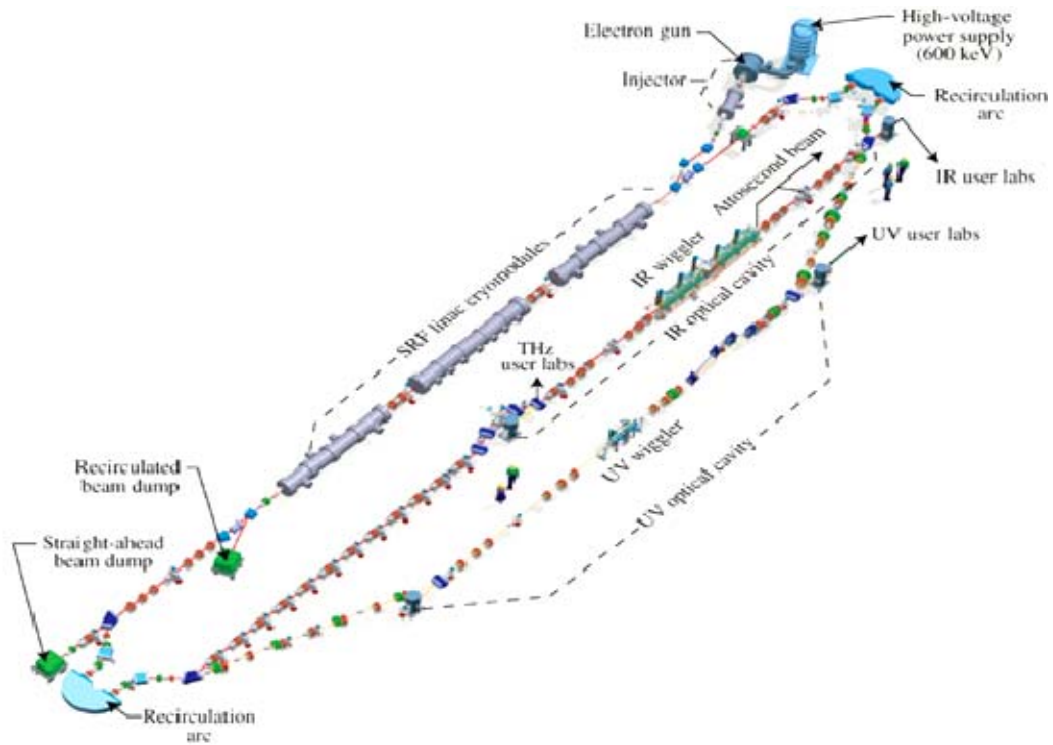
Figure 2.   JLAB Energy Recovery LINAC and Oscillator FEL. From [6]

1. Injector

The first and often most limiting component in any FEL is the injector, which generates the electrons that later become the FEL gain medium. An ideal injector would emit a narrow and very dense beam of electrons for later acceleration by the accelerating cavities. Due to the repelling effects of the Coulomb force, larger electron densities tend to increase the initial beam emittance, the product of the radius and angular spread of the electron beam. FELs can utilize several types of cathode inside their injector—the photocathode, the thermionic cathode, and the field emission cathode are examples. As shown in Figure 3, a typical photocathode utilizes the photoelectric effect to liberate electrons from the metallic cathode surface by illuminating it with a pulsed laser. Similarly, the thermionic cathode imparts kinetic energy to the electrons through a heating element to dislodge electrons from the cathode. A field emission cathode relies on the application of an exceptionally high external, electric field to produce tunneling and thereby emit electrons from the cathode surface. In all of these cases, once the electrons are released from the cathode surface, a high voltage field inside the injector's housing quickly accelerates them away from the cathode and toward the accelerating cavities.
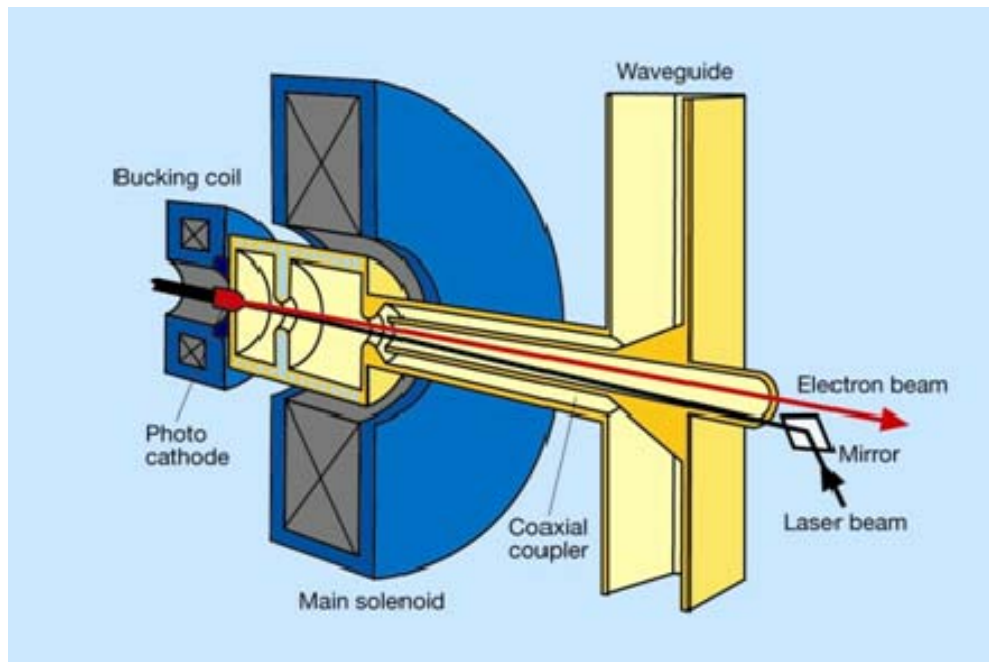
Figure 3.   Typical Photocathode. From [5]

2. Accelerating Cavities

After departing the electron gun, the electrons are accelerated to the required relativistic velocities through the use of radio frequency (RF) accelerating cavities. This acceleration is necessary to produce an electron beam with enough energy to create laser output at the desired wavelength. FELs have operated with linear accelerators (LINACs) consisting of either "normal" copper cavities or superconducting cavities, and either design has various benefits depending on the FEL's intended wavelength and output power. In both cases, the addition of RF cavities and their associated cooling systems adds considerable weight and volume to the overall FEL system design.

Despite the added cooling requirements, the superconducting accelerator cavity is generally preferred for high-power applications [7]. By reducing the resistive losses in the cavity wall, the RF energy that would have been lost as heat in a room temperature linear accelerator can now be applied to accelerate electrons, thereby improving overall cavity efficiency. Likewise, the higher average-power gradients created by superconducting cavities allow for shorter overall accelerating structures.

The accelerating cavities play an additional role in energy recovery linac (ERL) designs by allowing for the recovery of unused kinetic energy in the electron beam. For FEL designs at optical wavelengths, very high electron beam energy is required, but only a small fraction of this energy is actually utilized in the production of light by each electron bunch. Therefore, without some mechanism for energy recovery, a large amount of initial energy would go to waste in the beam dump. By carefully timing the arrival of returning electrons in the accelerator to be approximately 180 degrees out of phase with the oscillating RF fields, the electrons will actually decelerate and transfer most of their kinetic energy back to the accelerator. This allows for the recovery and reuse of a major portion of the original input power and reduces the thermal and radioactive contributions at the beam dump.

The models and picture in Figure 4 display the construction of a typical superconducting RF cavity. The upper figure is a single accelerating cavity with the electric fields, magnetic fields, and electron beam graphically depicted. In the center

figure, multiple cavities are combined, and the alternating electric fields and electron beam are displayed. The bottom figure is a photo of a typical accelerating cavity.
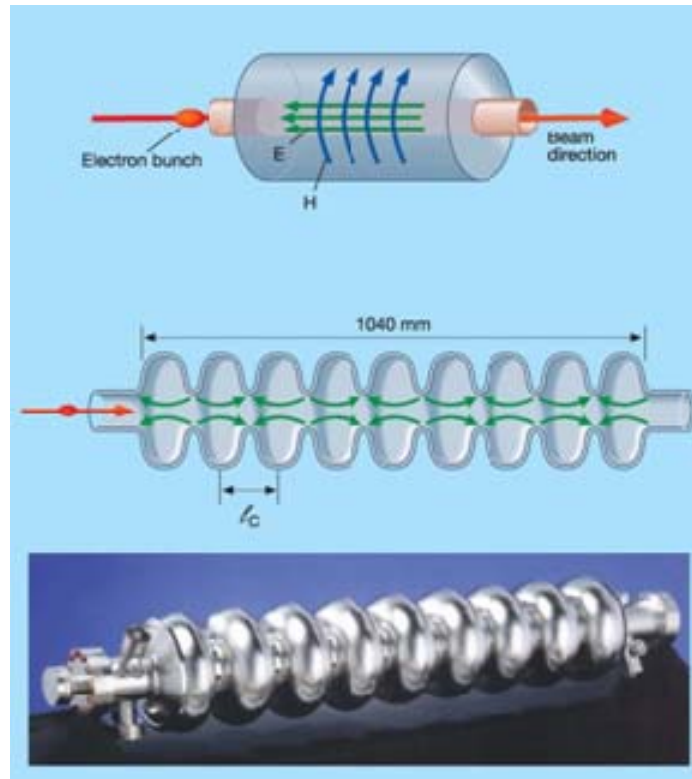
Figure 4.   A Cylindrical RF Cavity with Longitudinal Electric Field for Particle Acceleration. From [5]

3.   Cooling Systems

While a superconducting material exhibits zero loss for direct current (DC) applications, alternating current (AC) applications in the RF range produce a loss that scales in a roughly exponential manner with temperature [8]. Therefore, in order to reduce the resistive losses in the cavity walls, superconducting RF accelerator cavities must be cooled from room temperature (~300 K) to nearly 2 K. With such a large temperature gradient, these systems commonly utilize multiple insulation layers and shields at progressively lower temperatures to obtain the desired cavity temperature. Using liquid helium as a refrigerant, the cooling systems move heat away from the exterior walls of the accelerating cavities using a standard refrigeration cycle, but the

ultimate size and total input power of the cooling system is driven by the size of the accelerator cavities and their required cooling rate.

At the center of the cooling system, a volume of liquid helium surrounds the accelerator cavities. As shown in Figure 5, there are two liquid phases of helium—He I, which exhibits the properties of a conventional fluid, and He II, which is a "superfluid." Below about 2 K, liquid helium exhibits unusual dynamic properties (thus the description as a superfluid) and an extremely large heat capacity. This large heat capacity is what makes He II an ideal refrigerant for high power and high frequency applications.
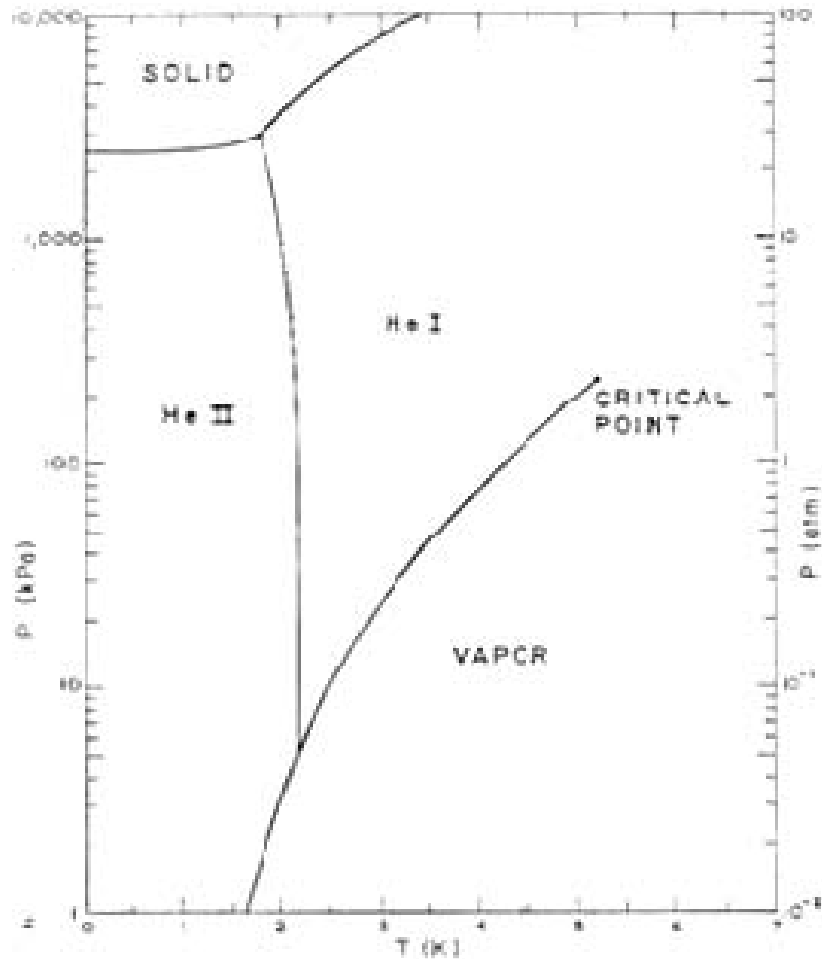
Figure 5.   Helium Phase Diagram. From [9]

At atmospheric pressure, the boiling point of liquid helium is 4.2K, and for lower frequency applications, the cavity power density and losses are low enough to use "normal" He I for a refrigerant.   Working at the natural boiling point allows for a simplified cryogenics system, but at frequencies above 800 MHz, the losses and power densities generally require more cooling than a He I system can provide. In the case of RF applications, the accelerating cavities are immersed in a bath of superfluid He II contained by a secondary shield.   The secondary shield is generally maintained at temperatures in the 30–50 K range by encasing them in a bath of He I. By reducing the drastic thermal gradient from the hot accelerator cavities to the room temperature housing, the cooling systems gain efficiency and reduce the total input power requirements [10].

4.   Beam Control Systems

From the moment the electrons are ejected from the cathode until their eventual collision with the beam dump, the electron beam radius and angular spread must be closely maintained. Inside the undulator, the overlap of each electron bunch with an associated optical pulse is essential to the production of light and to the operation of the FEL. Capitalizing on the magnetic component of the Lorentz force, beam steering and focusing is often achieved with the addition of large quadrupole electromagnets. Other bending and focusing systems can use electric or magnetic dipoles to alter the beam's trajectory.

As shown in Figure 6, quadrupole magnets consist of four magnets laid out in a "cross" pattern. Therefore, in the multipole expansion of the magnetic field, the dipole terms cancel and the lowest significant terms in the field equations are quadrupole terms. This effect produces a magnetic field that grows rapidly with radial distance from the beam axis, thereby providing an innate mechanism for beam focusing. It is impossible to simultaneously focus in both the horizontal and vertical planes in a quadrupole, so that a set of quadrupole magnets will focus in one plane while defocusing in the orthogonal plane in sequence along the beam line. By properly arranging alternating sets of these magnets (horizontally focusing then vertically focusing) with appropriate spacing in-between them, it is possible to achieve an overall focusing effect on the electron beam.
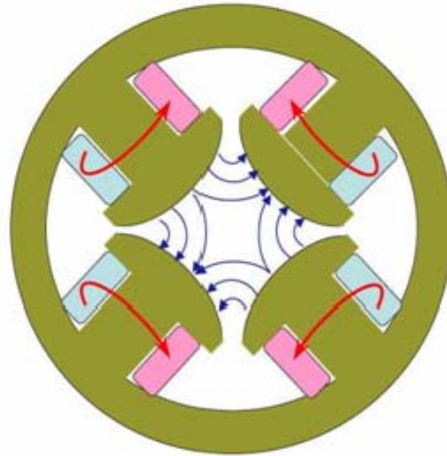
Figure 6.   Quadrupole Electromagnetic with Field Lines. From [11]

5.   Undulator

As shown in Figure 7, the undulator is a collection of strong permanent magnets that establish a periodic magnetic field to elicit oscillations in the electron beam. As electrons travel along the longitudinal axis, these alternating magnetic fields induce oscillations of the electrons in a transverse direction with respect to their original motion. Following the process of stimulated emission, the periodic transverse acceleration of the electrons in the presence of an optical wave produces coherent amplification of the optical wave. In order to ensure that amplification continues, both the amplifier and oscillator FEL designs must carefully coordinate the overlap of optical pulses and electron bunches. Demonstrating one of the primary advantages of the FEL, it is relatively easy to "tune" the output wavelength of an FEL by adjusting the spacing between the undulator magnets, commonly referred to as the undulator period.
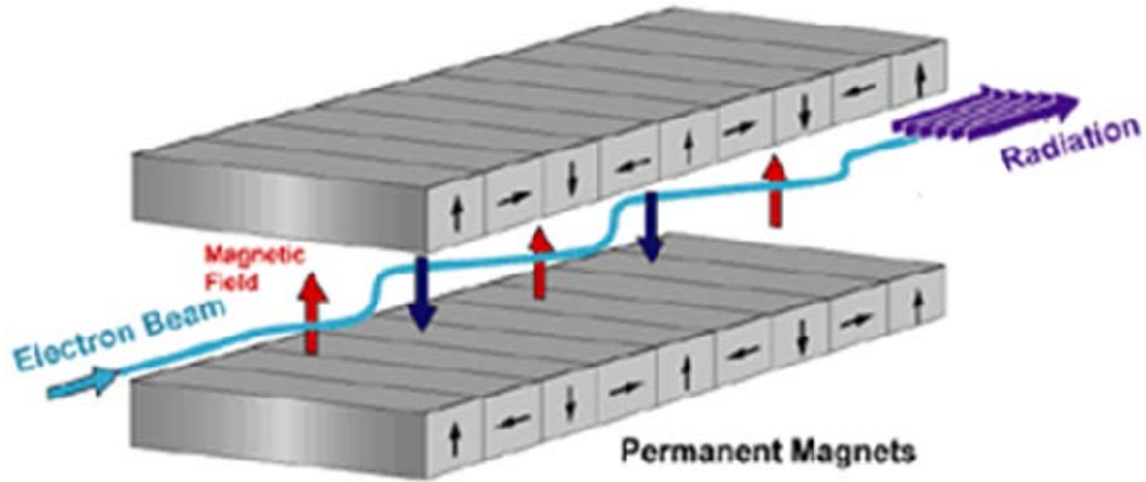
Figure 7.   Periodic Longitudinal Undulator. After [12]

6.   Resonator

Utilized only in the FEL oscillator design, the resonator is an optical cavity created by sandwiching the undulator between two reflective mirrors as shown in Figure 8. The distance between these mirrors is finely adjusted in order to ensure amplification of the optical wave and to prolong the interaction between the optical wave and the electrons. By ensuring the proper synchronization of electrons and optical pulses, the optical cavity allows for the amplification of the original light pulse. By making one of the mirrors partially transmissive, a fraction of the laser light is released on each pass to the output optics and beam director.
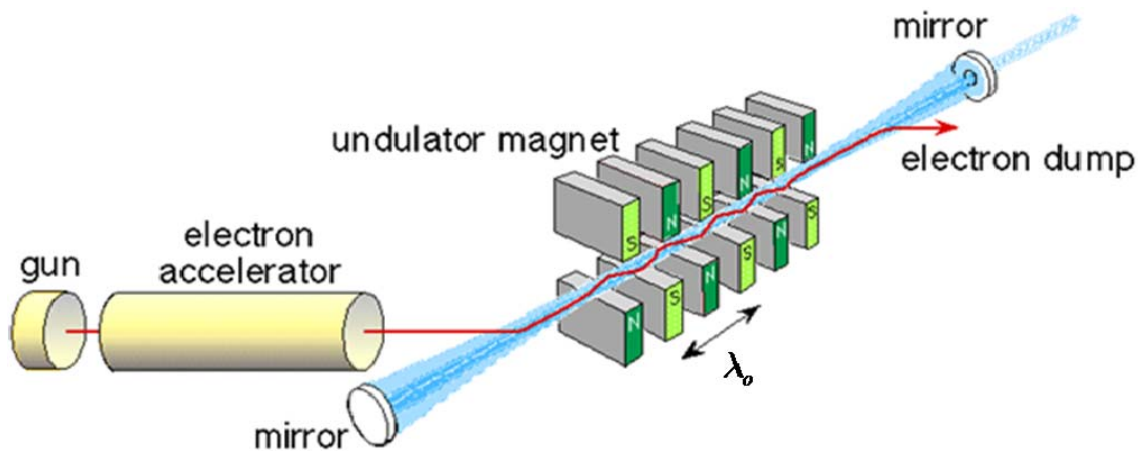
Figure 8.   Generic Oscillator FEL Design. From [13]

7. Electron Beam Recirculation / Energy Recovery

While passing through the undulator, the electron beam only contributes a small portion of its kinetic energy to the optical wave. There are two primary designs to recover this residual kinetic energy and improve the total system efficiency—the Storage Ring and the Energy Recovery LINAC. In an FEL utilizing a storage ring design, steering and focusing magnets bend the electron beam back to the accelerating RF cavities for re-acceleration back to the required operational energy. Thus, in this case, the same electrons will make multiple passes through the undulator. In contrast, an energy recovery LINAC ensures that the returning electron beam is properly out of phase with the RF fields when it arrives at the accelerator, so that the residual electron beam deposits most of its kinetic energy into the accelerator's RF fields. Then, the much lower energy electrons departing the accelerator are directed to the beam dump.

8. Beam Dump

At the end of the electron beam line, the beam dump is designed to safely and efficiently absorb the residual kinetic energy of the electron beam while dissipating the heat and shielding the radiation that is generated by collisions between the electrons and the beam dump material. The complexity of the beam dump is proportional to the remaining power in the electron beam. For a "low energy" beam, the beam dump might just be a copper block or Faraday cup that is air cooled, but for a "high energy" beam, the beam dump becomes a complex and intricate system in its own right.

Since the beam can often have megawatts of power remaining in high energy systems, the heating of the beam dump and breakdown of the dump material can be a significant concern. Some designs feature a long conical hole where the beam strikes to slowly "shave" the edges of the beam and spread the deposited heat over a wider area, and all designs utilize cooling to prevent failure of the beam dump material. While these cooling systems can be quite complex in structure and function, the primary purpose is to safely dissipate the thermal energy deposited by the beam, and most designs utilize a simple water recirculation system [14].

If the electrons in the beam are energetic enough, the impact of the beam can generate serious radiation hazards to equipment and personnel. Obviously, the "high energy" electrons themselves can cause considerable biological damage, but the collisions involved can generate neutrons and even gamma radiation in some cases. Therefore, the beam dump is usually surrounded by massive amounts of shielding material (often concrete blocks) to contain the radiation generated during operation. In many cases, the beam dump is the one component that is physically isolated from other portions of the system, e.g., in its own room, to allow for easy personnel access to the systems without exposing them to the residual radiation in the dump. In shipboard applications, the beam will enter the dump at energies low enough so that neutrons are not produced.

B.   FEL RESONANCE CONDITION

For optimum energy exchange between the electrons and the optical wave, the electrons' velocities must be such that over the distance of one undulator period an electron will fall behind a photon traveling at the speed of light by approximately one optical wavelength. As an electron passes through one undulator period, approximately one wavelength of light passes over it.

This "electron-photon" race is conceptually illustrated in Figure 9 with a red electron, blue photon (of wavelength λ), and green undulator period (λ_o). Due to its slightly lower speed, the "red" electron only travels a distance of λ_o, while the blue photon travels a total distance of $\lambda_o + \lambda$. In order to determine the wavelength of light emitted, the velocity difference between photon and electron ($c(1 - \beta_z)$) must be multiplied by the time it takes the electron to cover one undulator period ($\lambda_o / \beta_z c$). Assuming relativistic electrons, these substitutions and some simplifications produce the following relations between the optical wavelength (λ), the undulator period (λ_o), the dimensionless undulator parameter (K), and the Lorentz factor ($\gamma \gg 1$)

$$\lambda = \frac{\lambda_o \left(1 + K^2\right)}{2\gamma^2} \text{ where} \qquad \textbf{(II.1)}$$

$$K = \frac{e B_{RMS} \lambda_0}{2\pi m_e c^2}, \qquad \textbf{(II.2)}$$

where e is the electron charge, m_e is the electron mass, c is the speed of light, and B_{RMS} is the root mean squared value of the undulator magnetic field. Equation (II.1) demonstrates how an FEL can be "designed" or tuned for different wavelengths, by changing λ_o, K, or γ.
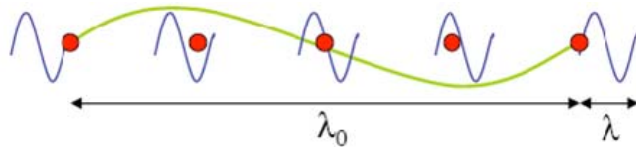
Figure 9.   The "Electron-Photon Race." From [15]

20

C.   FEL PENDULUM EQUATION

The electron dynamics within a free electron laser can be properly described by the solutions of the Lorentz force equations that account for the magnetic field of the undulator and the electric and magnetic fields of the optical pulse. The dynamics are controlled by relativistic but non-quantum mechanical effects—only classical mechanics and electromagnetism are applied. An "ideal" helical undulator has a magnetic field ($\vec{B}_u$) of

$$\vec{B}_u = B_m \left[\cos(k_o z_u), \sin(k_o z_u), 0\right] , \tag{II.3}$$

where B_m is the undulator magnetic field strength, k_o is the undulator wavenumber ($k_o = 2\pi/\lambda_o$), and z_u is the distance along the undulator axis. The associated optical electric and magnetic fields, in cgs units, are

$$\vec{E}_{op} = E\left[\cos\psi, -\sin\psi, 0\right] , \tag{II.4}$$

$$\vec{B}_{op} = E\left[\sin\psi, \cos\psi, 0\right] , \tag{II.5}$$

where $\psi = kz_u - \omega_{op}t + \phi$, E is the field amplitude in cgs units, ϕ is the phase, k is the wavenumber ($k = 2\pi/\lambda$), λ is the wavelength, and ω_{op} is the optical wave frequency. For a given electron velocity (v_e), the relativistic Lorentz force equations are

$$\frac{d(\gamma\vec{\beta})}{dt} = \frac{-e}{m_e c}\left(\vec{E}_{op} + \vec{\beta}\times\vec{B}_{op}\right) , \tag{II.6}$$

$$\dot{\gamma} = \frac{d\gamma}{dt} = \frac{-e}{m_e c}\left(\vec{\beta}\cdot\vec{E}_{op}\right) , \text{ and} \tag{II.7}$$

$$\gamma^{-2} = 1 - \vec{\beta}^2 , \tag{II.8}$$

where $\vec{\beta} = v_e / c$.

Assuming that the electrons are traveling at relativistic velocities and that they experience perfect injection into helical orbits, $\beta_z \approx 1$ and the transverse motion of the electrons in the undulator is

$$\vec{\beta}_\perp = \left(-\frac{K}{\gamma}\right)\left[\cos(k_o z_u), \sin(k_o z_u), 0\right] . \qquad \textbf{(II.9)}$$

After combining equation (II.4) with equation (II.7), it can be shown that

$$\dot{\gamma} = \frac{eKE}{\gamma m_e c}\cos(\zeta + \phi) , \qquad \textbf{(II.10)}$$

where $\zeta = (k + k_o)z_u - \omega_{op}t$ is the "electron phase". Since $k >> k_o$, the electron phase dsecribes the electron's microscopic position within an optical wavelength as it passes through the undulator. By defining the "electron phase velocity" as $\upsilon(\tau) = d\zeta/d\tau = L[(k + k_o)\beta_z - k]$, we can derive the FEL "pendulum equation"

$$\overset{\circ}{\nu} = \overset{\circ\circ}{\zeta} = |a|\cos(\zeta + \phi) , \qquad \textbf{(II.11)}$$

where $\overset{\circ}{\nu}$ denotes a derivative of the electron phase velocity with respect to the dimensionless time, $\tau = \frac{ct}{L}$ is the dimensionless time, L is the length of the undulator, N is the number of undulator periods, and $|a| = 4\pi NeKLE/\gamma 2 m_e c^2$ is the dimensionless optical field amplitude. The laser has weak optical fields that do not over bunch electrons when $|a| \leq \pi$, but when $|a| >> \pi$, the laser has strong fields and is near saturation, where electron over-bunching takes place. The specific phase-space path of each individual electron can be identified by

$$\nu^2 = \nu_o^2 + 2|a|[\sin(\zeta + \phi) - \sin(\zeta_o + \phi)] , \qquad \textbf{(II.12)}$$

where ν_o and ζ_o define the initial electron coordinates in phase space, and the separatrix is given by $\nu^2 = 2|a|[1 + \sin(\zeta + \phi)]$. The amplitude of the closed orbit in phase space is $2|a|^{1/2}$.

D. FEL WAVE EQUATION

In the presence of an electron beam, the full wave equation is

$$\left(\vec{\nabla}_\perp^2 - \frac{1}{c^2}\frac{\partial^2}{\partial t^2}\right)\vec{A}(\vec{x}_u,t) = -\frac{4\pi}{c}\vec{J}_\perp(\vec{x}_u,t) \ , \tag{II.13}$$

where $\vec{x}_u$ is the distance from the beam axis, $\vec{A}(\vec{x}_u,t) = \left(E/k\right)[\cos\psi, -\sin\psi, 0]$ is the optical vector potential, and $\vec{J}_\perp$ is the current density due to the undulator's oscillating magnetic fields. The laser's electric and magnetic fields are related to the vector potential, $\vec{A}$, by Maxwell's equations

$$\vec{E}_L = -\frac{1}{c}\frac{\partial\vec{A}}{\partial t} \quad \text{and} \tag{II.14}$$

$$\vec{B}_L = \vec{\nabla}\times\vec{A} \ . \tag{II.15}$$

After combining Equations (II.13) through (II.15) above with Equation (II.9) and assuming slow variations in the field's phase and amplitude, we derive that the field evolves according to

$$\frac{\partial}{\partial t}\left(Ee^{i\phi}\right) = -\frac{2\pi Kec\rho_e}{\gamma}\left\langle e^{-i\zeta}\right\rangle \ , \tag{II.16}$$

where ρ_e is the electron density and $\langle...\rangle$ is the average of all electrons. If we then multiply both sides of equation (II.16) by a factor of $4\pi NeKL/\gamma^2 m_e c^2$, it can be written as

$$\left[-\frac{i}{4}\vec{\nabla}_\perp^2 + \frac{\partial}{\partial\tau}\right]a(\vec{x},t) = -\left\langle je^{-i\zeta}\right\rangle \ , \tag{II.17}$$

where the dimensionless current density (j) is defined as

$$j = \frac{8\pi^2 Ne^2K^2L^2\rho_e}{\gamma^3 m_e c^2} \ . \tag{II.18}$$

23

In equation (II.17) above, we can trace the effects of each term on the diffraction, gain, and bunching in an FEL. The $\nabla_\perp^2$ term operating on the dimensionless laser field amplitude, a, describes the diffraction of the laser beam. When diffraction is significant, the left side of equation (II.17) includes a double derivative term to account for the changing amplitude and phase; but when diffraction is small, the wave equation simplifies to equation (II.19) where only the dimensionless time derivative term of a remains

$$\overset{\circ}{a} = -j\left\langle e^{-i\zeta} \right\rangle . \qquad\qquad \textbf{(II.19)}$$

The dimensionless current density, j, describes the coupling between the laser light and the electron beam and therefore the gain of the free electron laser. When the dimensionless current is small ($j \leq \pi$) the FEL coupling and gain is small, but when $j \gg \pi$, the coupling and gain are large. The bunching of the electron beam is described by the final term $\left\langle e^{-i\zeta} \right\rangle$. When the electrons are randomly distributed in ζ, the overall average and coupling is small, so that the wave does not evolve, $\overset{\circ}{a} \approx 0$.

As the laser begins operation, a feedback loop develops between the wave equation (II.19) and the pendulum equation (II.11). While traveling along their phase space paths, the electrons begin to bunch, this electron bunching changes the $\left\langle e^{-i\zeta} \right\rangle$ term in equation (II.19), and therefore the dimensionless time derivative of the laser field amplitude also changes. The laser field, amplitude or phase, can increase or decrease depending on the sign of $\left\langle e^{-i\zeta} \right\rangle$. An increasing a can also drive an increase in the electron phase acceleration from equation (II.11). This increase in phase velocity fuels further bunching, creating a feedback loop that will drive gain exponentially higher. This field growth eventually can fall in strong optical fields as the electrons move through their paths in phase space and begin to absorb energy back from the optical beam.

E. FEL PULSE STRUCTURE

The MW-class FEL is often referred to as a high average power laser, while most other lasers that produce the same average power are referred to here as high-peak power lasers. An important difference between the FEL and other lasers of similar power is its pulse structure. High-peak power lasers can produce peak powers in the TW range, but they maintain a low pulse repetition frequency (PRF) in the tens of Hz. High average power lasers, like a MW-class FEL, produce a peak power in the GW range, but their PRF is almost 1 GHz. Figure 10 displays the micro-pulse structure for a MW-class FEL with repeated micro-pulses of over 1 GW at approximately 700 MHz PRF producing an average power of about 1 MW. Later analysis, in Chapter VII, will utilize the ratio of peak-to-average power in a comparison of laser and solar intensities. It is important to realize that the FEL peak power is over 1000 times greater than the average power, and that the PRF is highly precise.
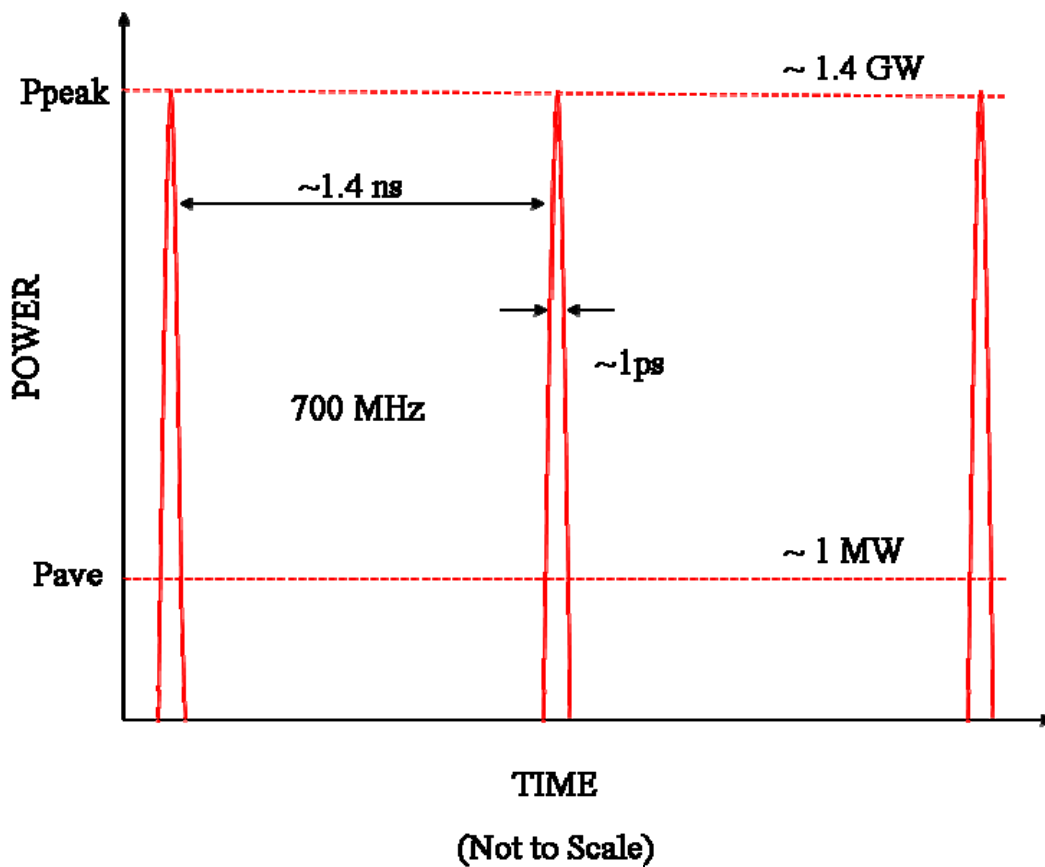
Figure 10.　　MW-Class FEL Macro-Pulse Structure

THIS PAGE INTENTIONALLY LEFT BLANK

III. LASER PROPAGATION

The application of a high-energy, ground-based laser for power beaming, extraterrestrial illumination, or orbital debris clearance requires an understanding of beam propagation. Transmitting a high power beam through a possibly thick and fluid atmosphere over extreme ranges can affect the beam quality and lead to unintended effects at the target. Random thermal and density gradients within the air cause random fluctuations in the refractive index of the atmosphere that degrade the propagation of an optical wave. These effects cause the twinkling of stars that we see at night and limit the resolution ability of earthbound telescopes to a few seconds of arc, but they can also degrade the spatial coherence of a laser beam as it propagates through the atmosphere [16, p. 1]. The loss of spatial coherence will ultimately limit the ability to focus the laser beam, and it can drastically lower the power on target of laser systems. In most cases, these losses can be mitigated through the use of an adaptive optics system for the director. Also, like astronomical observatories, ground-based lasers utilized in space applications could avoid most of the detrimental effects of atmospheric propagation by operating at high altitude, but that would require the construction of an associated electrical generator.

The fundamental propagation effects faced by a ground based laser are: diffraction, scattering, absorption, turbulence, and thermal blooming. With the notable exception of thermal blooming, all of these are linear effects, and the relative importance of each loss mode varies with application. As described by Andrews, some common types of space and laser applications are cited below with a brief description of their primary atmospheric effects after [16, p. 11–13]:

- *Satellite-ground:* Laser communications to the ground from a satellite are disrupted by the atmospheric turbulence near the ground, but for most of the path the beam passes through little turbulence. Because the propagation distances are so long, the beam is very wide by the time it encounters the atmospheric layer. Hence the beam is mostly disturbed by spatial phase fluctuations, thereby limiting heterodyne efficiency in coherent detection. The primary concerns for downlink propagation paths are scintillations and angle-of-arrival fluctuations.

27

- *Ground-satellite:* A transmitted laser beam for communications from the ground to a satellite is disrupted by atmospheric turbulence near the ground and, thus, near the transmitter. Because most of the propagation path lies beyond the atmospheric layer, there is a long propagation path in free space that is dominated by free-space diffraction. The primary concerns for an uplink path are scintillations, beam wander, and beam pointing.

- *Aircraft-satellite and satellite-aircraft:* These two communication paths are similar to the ground-satellite and satellite-ground paths described above. Although the aircraft is usually above much of the natural atmospheric ground-induced turbulence, aircraft boundary layer effects due to platform speed need to be addressed.

- *Imaging:* Problems associated with imaging through the atmosphere are similar to those associated with propagation. For example, the "dancing" of an image in the focal plane of an imaging system is mathematically equivalent to the wander of a beam focused at the object by the same optical system. The resolution of a long-exposure image is equivalent to the long-term beam spread of a focused beam. The short-exposure resolution is equivalent to an optical heterodyne receiver that employs tilt-correction of the signal or of the local oscillator. Among others, adaptive optics systems are widely used today to provide turbulence-compensation techniques to improve image quality.

A. DIFFRACTION

Diffraction effects are a consequence of the wave nature of light that cause beam spreading as the wave propagates away from the beam waist, i.e., that part of the beam where the beam has the smallest diameter. This results in decreased beam intensity and constantly changes the phase front radius of curvature of the propagating wave. Diffraction is the only mechanism that is not linked to the presence of matter and, thus, in the approximate vacuum of near-Earth and interstellar space, it is responsible for the primary loss in intensity of the optical beam. Inside the atmosphere, the loss of beam intensity due to diffraction can be magnified significantly by atmospheric turbulence.

When evaluating diffraction effects, there are two distinctive models available. In Fraunhofer, or far-field, diffraction, the point of observation is far enough from the beam waist so that waves arriving at the point of observation may be considered plane waves. When this is not the case and the curvature of the wavefront must be taken into account,

Fresnel, or near-field, diffraction must be applied. In the far-field approximation, the diffraction pattern (or beam spot size) changes uniformly in size with distance from the beam waist. In the near-field, the diffraction pattern is more complex [17, p. 324].

In Figure 11, the growth in cross sectional area or spot size of a Gaussian beam is graphically depicted showing the radius at the beam waist (w_o), Rayleigh range (z_R), beam divergence angle (θ), range from beam waist to the target (z), and beam radius at the target (w). In the fundamental mode of a Gaussian beam, the intensity of the beam has a normal, i.e., Gaussian, distribution. In this case, the beam spot size is simply the area of the fundamental mode at a specific point along the beam's axis of travel.
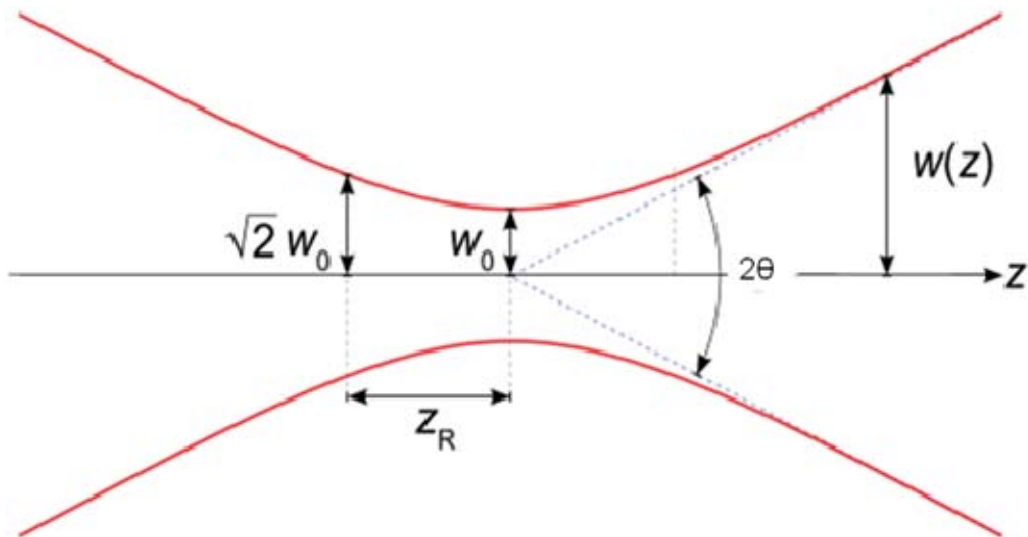
Figure 11.　　Collimation of a Gaussian Beam. After [18]

Assuming a Gaussian beam, the change in beam spot size due to diffraction in the far field can then be approximated based on the wavelength of the optical wave (λ), the range (z), and the beam waist (w_o) by the equation

$$w(z) = w_o \sqrt{\left[1 + \left(\frac{\lambda z}{\pi w_o^2}\right)^2\right]} \; . \qquad \textbf{(III.1)}$$

For large z, the beam waist can be approximated by

29

$$w(z) \approx \frac{z\lambda}{\pi w_o} .$$ (III.2)

When discussing the ability of a laser to retain a focused beam pattern, scientists utilize a parameter called the Rayleigh range (z_R). The Rayleigh range is defined as the distance from the beam waist to the transverse plane where the beam area has doubled. It is the characteristic distance over which a beam area expands due to diffraction. Similarly, the beam divergence angle (θ_B) is used to determine the beam spot size at the target. The formulas for the Rayleigh range and the beam divergence angle are

$$z_R = \frac{\pi w_o^2}{\lambda} \quad \text{and}$$ (III.3)

$$\theta_B \cong \frac{\lambda}{\pi w_o} .$$ (III.4)

The beam's spot size (A_s) at a distance z from the waist is

$$A_s = \frac{\lambda^2 z^2}{\pi w_o^2} = \pi w^2 \quad \text{and}$$ (III.5)

the intensity (I) is given by

$$I = \frac{P}{A_s} ,$$ (III.6)

B.   SCATTERING

When any electromagnetic wave travels through a medium, it can interact with scattering centers in the medium, such as water vapor, suspended aerosols, or other particulates. These scattering centers can redirect or disperse the energy of the

electromagnetic wave, and in the specific case of a laser beam, scattering results in the loss of intensity at the target. Even on a clear day, scattering can reduce transmission in the visible spectrum to 20% for a 16 km path [19, p. 24].

Mie scattering is a complex theory that takes into account the size, shape, refractive index, and absorptivity of the scattering particles. In the discussions below, Mie scattering is a term that is applied to the scattering process when the scatterer is comparable in size to the wavelength of the incident radiation. Rayleigh scattering and non-selective scattering are special cases of Mie scattering. Rayleigh scattering is the scattering of electromagnetic radiation by particles much smaller than the wavelength of the radiation; i.e., individual atoms or molecules. Nonselective, or geometrical, scattering occurs when the scattering center is much larger than the wavelength of the incident light, such as with haze, fog, or rain. Comparing the size of the scattering center and the wavelength of the incident radiation, as shown in Table 1, allows for simplifications of Mie theory into Rayleigh scattering, when the scatterer is small, and non-selective scattering, when the scatterer is large.

Type of Scattering	Size of Scatterer
Rayleigh Scattering	Larger than an electron but smaller than λ
Mie Scattering	Comparable in size to λ
Non-selective Scattering	Much larger than λ

Table 1.   Types of Atmospheric Scattering. From [19, p. 24]

For all types of scattering, the bound electrons experience a displacement due to the harmonic oscillation of the incident electric field. The response of the electron to this driving force is a function of the driving frequency and the natural or resonant frequency of the oscillator [17, p. 303]. The oscillating dipoles re-radiate or scatter their energy in

31

all directions except along the dipole axis itself, but each form of scattering results in a different scattering pattern. As the scattering center grows in size with respect to the wavelength of radiation, the energy reemitted by the dipole begins to emit preferentially in the direction of travel of the incident light. This is graphically illustrated in Figure 12.
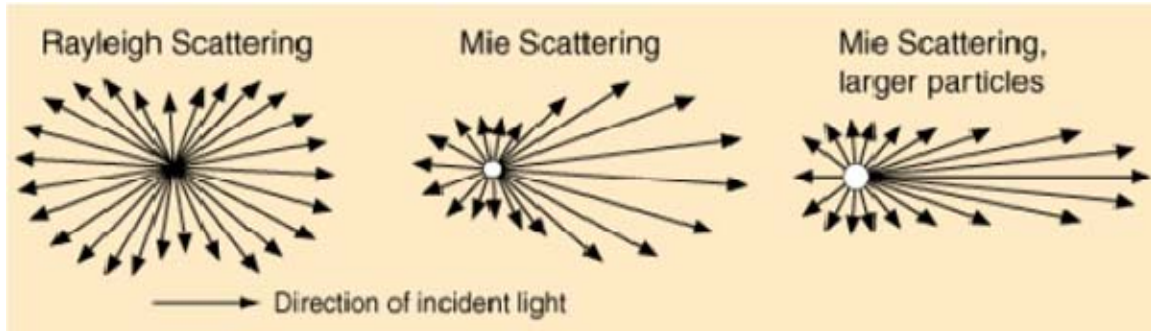
Figure 12. Rayleigh, Mie, and Nonselective Scattering. After [20]

1. Rayleigh Scattering

Rayleigh scattering is the scattering of electromagnetic radiation by particles much smaller than the wavelength of the radiation; i.e., individual atoms or molecules. In Rayleigh scattering, the distance between scattering centers allows them to act incoherently, and therefore, their net irradiance is a sum of their individual irradiances. From [21, p. 448], the radiated power can be shown to be proportional to the fourth power of the frequency or inversely proportional to the fourth power of the wavelength of the incident radiation. This is the Rayleigh Scattering Law

$$P_{dp} = \frac{\mu_o \omega_f^4 p_o^2}{12\pi c} \, ,$$

(III.7)

where P_{dp} is the power radiated by the dipole, μ_o is the permeability of free space, ω_f is the frequency of the incident radiation, and p_o is the maximum value of the atom's dipole moment. Therefore, as shown in Figure 13, oscillating dipoles scatter more energy in the high frequency, short wavelength region of the optical spectrum than in the low frequency, long wavelength region.
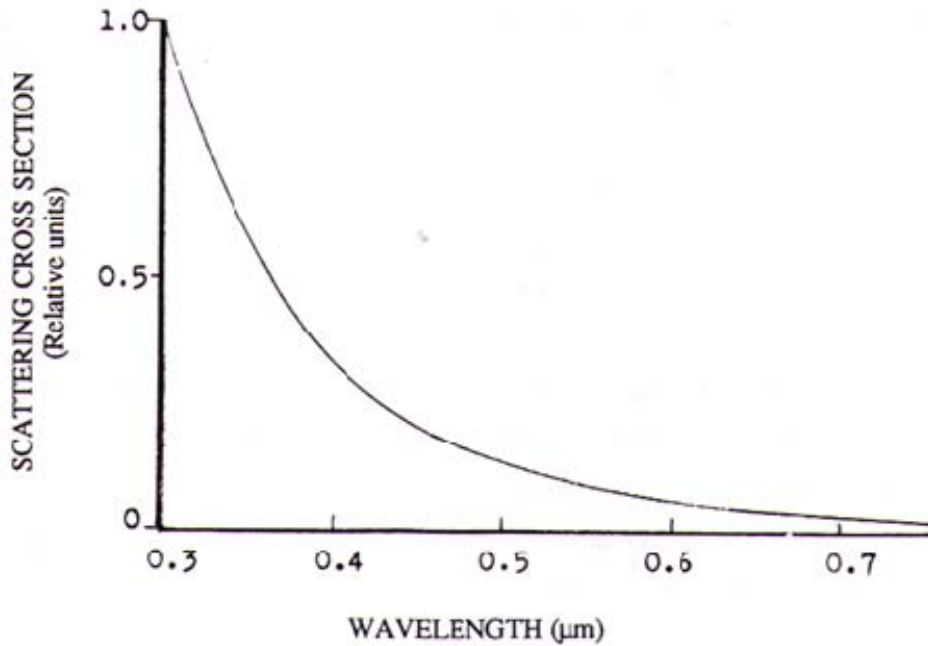
Figure 13.   Rayleigh Scattering. From [19]

The sun emits radiation across most of the electromagnetic spectrum, but its output is not uniform at all wavelengths (covered in more detail in Chapter V). Within the optical spectrum, the peak of the sun's output is in the yellow wavelengths, and when viewed directly, the sunlight appears to be yellowish-white in color. Inside the Earth's atmosphere, sunlight experiences Rayleigh scattering due to the nitrogen and oxygen molecules in the air. If there were no atmosphere, the sky would appear black, but inside the atmosphere, the short wavelength, blue light is scattered randomly and arrives at the observer from all directions, making the sky appear blue. Viewing the sun at its zenith, the sunlight travels through a relatively thin portion of the atmosphere and only a fraction of the light is scattered, making the sky appear blue while the sun appears yellow or white. Viewing the sun low on the horizon, the sunlight travels through a relatively long and dense section of the atmosphere and the sun appears red or orange. The preferential scattering of shorter wavelengths in the daytime sky is a clearly visible demonstration of the $1/\lambda^4$ effect in Rayleigh scattering. In the design of a ground based laser system for

space applications, the implication is clear that, within the optical spectrum, longer wavelengths will experience less loss due to scattering [17].

2. Mie Scattering

Mie scattering occurs when the scattering centers are comparable to the size of the incident wavelengths, such as with aerosols or small water droplets. In Rayleigh scattering, the spatial variation of the electric field over the molecular charge distribution could be ignored due to the relative sizes of the wavelength and molecule. When the radius of the molecule is approximately equal to the wavelength of the incident radiation, the variations of the electric field over the molecule become significant, and they can drastically affect the directionality of the dipole radiation. Despite aerosol particle concentrations that are orders of magnitude lower than molecular concentrations in the atmosphere, Mie scattering in the optical wavelengths far exceeds the attenuation due to both Rayleigh scattering and ozone absorption [19, p. 29]. As shown in Figure 14, the Rayleigh scattering coefficient only becomes comparable to the total aerosol extinction, i.e., aerosol scattering plus absorption, for wavelengths shorter than about 0.3μm, whereas aerosol scattering and absorption dominate at longer wavelengths.
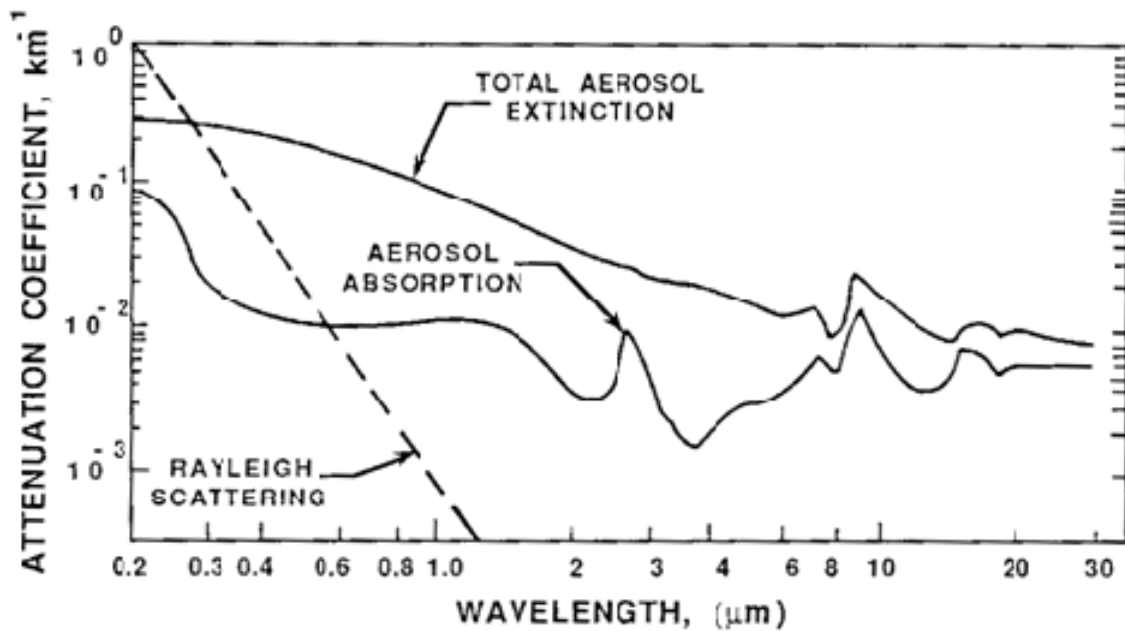
Figure 14.   Rayleigh and Aerosol Attenuation. From [22]

34

3. Nonselective Scattering

Nonselective, or geometrical, scattering occurs when the scattering center is much larger than the wavelength of the incident light, such as with haze, fog, or rain. Haze refers to the small particulates of salt, dust, and combustion products suspended in the air with radii less than about 0.5 μm. In conditions of high humidity, these small particles serve as nucleation sites for the condensation of water molecules, and this condensation can rapidly increase the overall surface area of the particulate. When these particulates increase in size to exceed 0.5 μm, the haze becomes fog if touching the ground, or clouds if suspended above it.

As the particles continue to grow, they become raindrops, which are many times larger than the wavelength of a laser beam. In the presence of these large scattering centers, the wavelength dependence on scattering is eliminated, and the scattering coefficient varies purely as a function of the drop size [19, p. 41]. Thus, all wavelengths scatter equally from clouds, making them appear white. In a heavy rain, laser beam transmission through the atmosphere can be dramatically affected. Rainfall rates for four different rain conditions and the corresponding transmittance, due to scattering only, of a 1.8 km path are shown in Table 2.

Condition	Rainfall (cm/hr)	Transmittance of a 1.8 km path
Light Rain	0.25	0.88
Medium Rain	1.25	0.74
Heavy Rain	2.5	0.65
Cloudburst	10	0.38

Table 2.   Transmittance of a 1.8 km Path Through Rainfall. From [19, p. 43]

In Figure 15, the attenuation coefficients for a typical dense fog and light rainfall is plotted versus wavelength from 0.6 to 15 μm. To allow for comparison, the absorption coefficients of a layer of water containing the same amount of liquid water as the rain are also presented. For all wavelengths shown, the attenuation of rain is relatively constant and much less than that of a dense fog. It is immediately apparent that any ground based laser system intended for space applications should operate at a high altitude and arid ground site to minimize the losses due to scattering regardless of the wavelength in use.
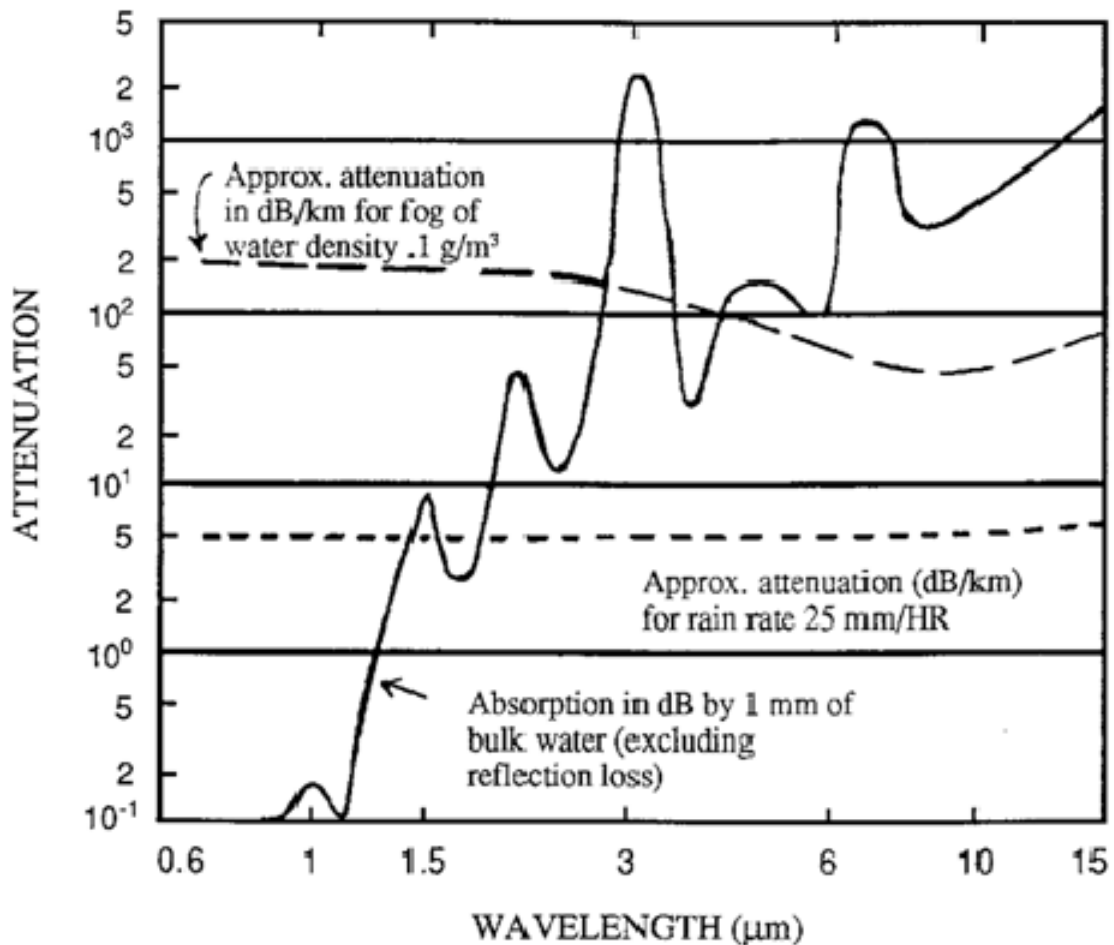
Figure 15.   Attenuation of IR Radiation due to Rain and Fog. From [19, p. 44]

C.   ABSORPTION

Absorption is the process by which the energy in an electromagnetic wave is attenuated in passing through a medium by the conversion of the energy into heat or other

forms of molecular energy. The capacity of a specific medium to absorb radiation is dependent on several factors such as the wavelength of the radiation, the thickness of the medium, the atomic and molecular properties of the medium, and the temperature and density of the medium. A perfectly transparent medium would permit the passage of a laser beam without any loss of intensity, while a perfectly opaque medium would completely block the beam. In reality, there is no material that is perfectly transparent or opaque across the entire electromagnetic spectrum. Thus, it is vitally important to consider the absorption spectrum of the intervening medium when attempting to propagate an electromagnetic wave through the medium. Most importantly, the amount of absorption determines the likelihood of thermal blooming. This process is nonlinear, and it can limit the power transmitted over long distances through the atmosphere. Specifically, any ground based laser must find a "window" of atmospheric transparency at some appropriate wavelength in order to maximize the transmission of beam power through the atmosphere [23].

Earth's atmosphere is composed of 78% nitrogen, 21% oxygen, and 1% of argon and trace elements. Nitrogen (N_2) and oxygen (O_2) have no dipole moment and therefore do not exhibit molecular absorption bands. In the other gases, water (H_2O), carbon dioxide (CO_2), and ozone (O_3) are the most significant contributors to atmospheric absorption. Water vapor varies widely, but averages about 0.5% of the atmosphere. Ozone is found in relatively large concentrations at high altitudes near 30 km, but the concentration of ozone near sea level is negligible [19].

Figure 16 is a chart of the atmospheric transmittance, including scattering and absorption effects, measured over an 1820 m horizontal path at sea level. Table 3 lists the wavelength intervals where transmittance is relatively high. For efficient transmission, the laser wavelength should be selected in the center of these windows as the transmission is decreased at the window boundaries. Figure 16 and Table 3 are useful in examining the general effects of absorption on atmospheric transmission over near-horizontal paths, but any conclusions drawn from them would not necessarily apply for a ground based laser system transmitting vertically through the atmosphere. The FEL

bandwidth is estimated at 0.1 %, or about 10^{-3} μm for an FEL operating at 1 μm, and it would be expected to "fit" into any of these windows [15].
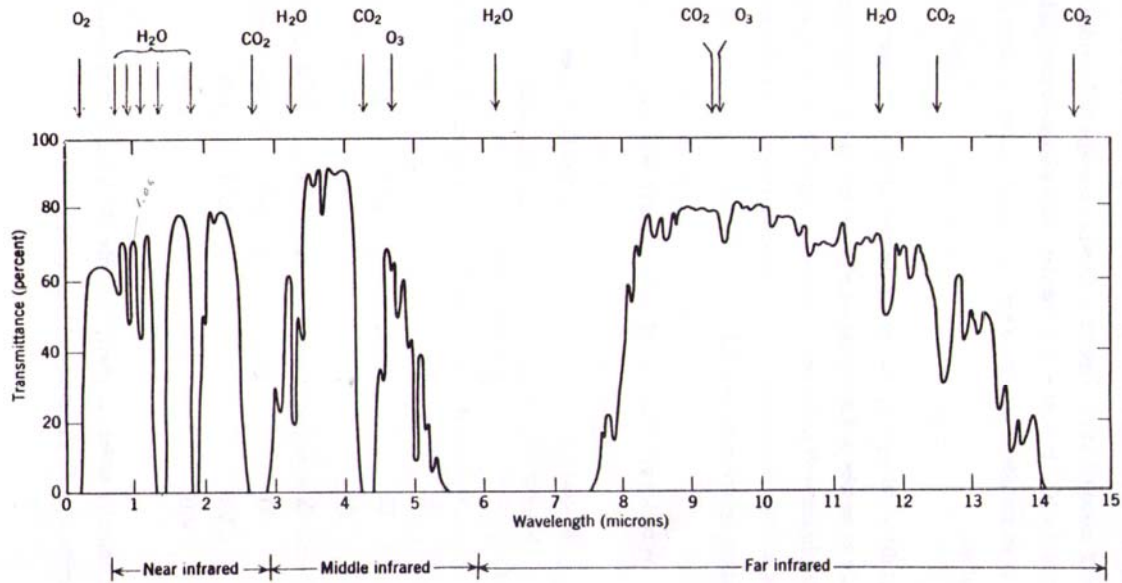
Figure 16.   Atmospheric Transmittance. From [19, p. 15]

Window Number	Window Boundaries (μm)	
	Low	High
I	0.72	0.94
II	0.94	1.13
III	1.13	1.38
IV	1.38	1.90
V	1.90	2.70
VI	2.70	4.30
VII	4.30	6.0
VIII	6.0	15.0

Table 3.   Wavelength Regions of Atmospheric Windows. From [19, p. 16]

D.   TURBULENCE

Treating the atmosphere as a viscous fluid, the motion of the air can be described by fluid mechanics as either laminar or turbulent. In laminar flow, the velocity is uniform, or changes in a regular pattern, and mixing does not occur. In turbulent flow, dynamic mixing of the air leads to the creation of turbulent eddies within the air. Like a layered onion, the Earth's atmosphere is relatively dense within the first 20 km, but extends in varying layers to approximately 700 km. In a region within about 2 km of the Earth's surface, called the atmospheric boundary layer, atmospheric dynamics are dominated by the viscosity of the air and the heat exchange interaction with the Earth's surface, and the atmosphere can be turbulent [16].

Atmospheric turbulence is a linear effect that occurs when air packets at differing temperatures are mixed by wind and convection. Over time, the air will reach a thermal equilibrium as the turbulence cells break down into smaller eddies. In the interim, the turbulent mixing produces random density fluctuations, and therefore, changes in the index of refraction of the air.

This turbulent flow of air, temperature fluctuations, and the associated density fluctuations within the propagation path of a laser beam can cause variations in the index of refraction along the path length. These small and localized variations in the index of refraction can then cause phase fluctuations within the laser beam.   The phase fluctuations act as random lenses, and they result in amplitude fluctuations across the beam wave front. Wave front distortions caused by atmospheric turbulence can lead to the broadening of a laser beam, random changes in the beam direction ("beam wander"), and intensity fluctuations within the beam profile ("scintillation").

The defining parameter to describe the beam disturbances caused by turbulence is the refractive index structure coefficient (C_n). It is a function of the pressure and temperature difference between two points separated by distance *r*, and it is given by

$$C_n = \left[79x10^{-6} \frac{P_P}{T^2} \right] C_T \, , \qquad\qquad \textbf{(III.8)}$$

where the temperature structure parameter (C_T) is

$$C_T = \left[\sqrt{\left\langle \left(T_1 - T_2 \right)^2 \right\rangle} \right] r^{-\frac{1}{3}} , \qquad \textbf{(III.9)}$$

T is the average air temperature in degrees Kelvin, T_1 and T_2 are the temperatures at the points of interest in degrees Kelvin, P_P is the atmospheric pressure in millibars, and r is the distance in cm between points. Measurements of C_n inside the atmospheric boundary layer have demonstrated that it reaches a minimum about one or two hours before sunrise and after sunset [19, p. 49]. Typical values of the refractive index structure are shown in Table 4.

Strength of Turbulence	C_n (m$^{-1/3}$)
Strong	5 x 10^{-7}
Intermediate	4 x 10^{-8}
Weak	8 x 10^{-9}

Table 4.   Typical Values of C_n. From [19]

1.   Beam Wander

Beam wander describes the random motion of the beam's spot at the target due to turbulence effects that are generally larger in size than the beam diameter. In general, beam wander has been demonstrated to be independent of the beam wavelength, and closely follows the value of C_n [19, p. 54]. It becomes a major problem for applications at long range when the laser must stay fixed on a relatively small target. Thus, for a ground based laser beaming power out of the atmosphere, a fast and highly accurate optical tracking system will probably be required to keep sufficient intensity on target.

2.   Scintillation

Scintillation describes the "twinkling" of stars or the "flicker" of a laser beam as it arrives at the target. When the air flow moves small index-of-refraction inhomogeneities through the path of the beam, the disruption of the beam wavefront can lead to intensity variations within the beam profile and result in "hot spots" at the target. Although the time averaged intensity on target remains fairly constant, scintillation can be harmful in laser applications. Local "hot spots" within the beam can lead to thermal blooming and in power beaming applications the higher intensities may exceed the solar cells' power conversion rate.

3.   Turbulence Induced Beam Spreading

In addition to diffraction effects, a laser beam propagating through the turbulent atmosphere experiences a broadening due to the loss of spatial coherence of the wave. Sometimes referred to as "beam breathing," this effect is similar to diffraction, and it can increase the beam spot size at the target. In practice, observed spot sizes can be twice as large as those predicted by diffraction theory alone [19, p. 61].

E.   THERMAL BLOOMING

For high power beams, the molecular absorption of the beam's energy by the atmosphere can lead to temperature, density, and index-of-refraction changes within the air. As the beam continues to travel through air, it can experience a nonlinear, defocusing or "blooming" effect.

Figure 17 shows the evolution of a Gaussian beam and its temperature (T), density (ρ), and index of refraction (n) as the beam suffers the effects of thermal blooming. No turbulence is included in this example. The lower half of Figure 17 shows the initial irradiance, temperature (To), density (ρo), and index of refraction (no) profile of a Gaussian beam. At the center of the Gaussian beam, where the intensity is the highest, the absorption of laser energy and subsequent release of heat results in a radial temperature profile with the hotter, less dense air in the center of the beam and the colder, more dense air at the edges of the beam. These density changes lead to a change in the index of refraction which tends to deflect the power of

41

the beam radially away from the beam center. Thus, a Gaussian beam at transmission arrives at the target in a ring pattern, as shown at the top of Figure 17.
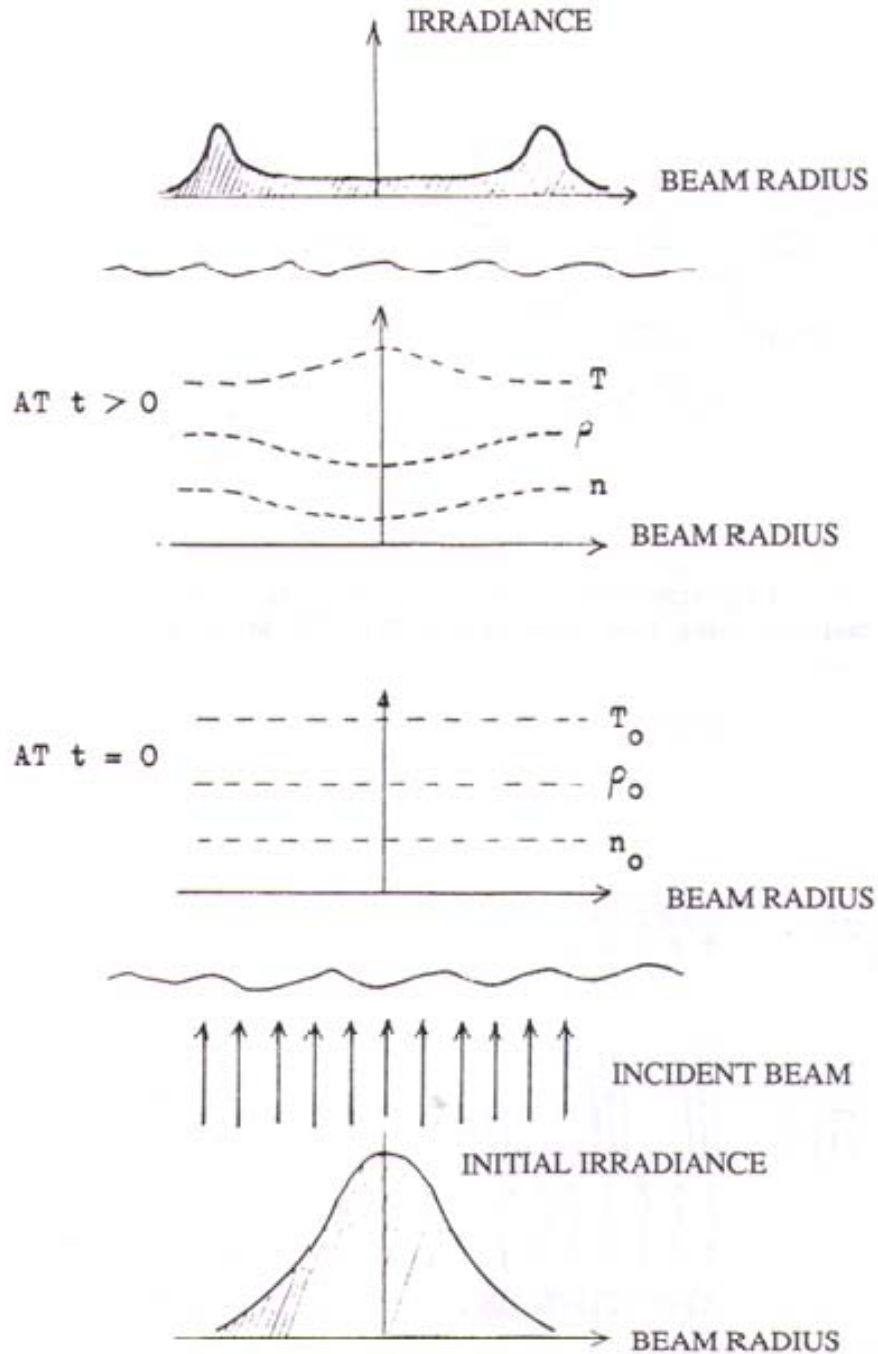
Figure 17.   Thermal Blooming of a Gaussian Wave. From [19, p. 69]

Figure 18 is an illustration of a laser beam suffering from thermal blooming. In this figure, a laser beam of power (P) and cross sectional area (A) propagates through an air column of total length (R). During its propagation, the laser beam passes through a stagnation range (R_s) representing a column of stationary air. It is within this stagnant column of air that thermal blooming occurs and begins to spread the beam. An estimation of the temperature increase per second is given by

$$\frac{\Delta T}{\Delta t} \approx \frac{\alpha R_s P}{\rho c_p A R_s},$$ **(III.10)**

where ΔT is the change in temperature given in K, Δt is the change in time given in seconds, α is the absorptivity of air ($\sim$ 0.0041 km^{-1} at 1μm [25]), R_s is the stagnation range, P is the power of the laser, ρ is the density of air ($\sim$ 1.2 kg/m^3 at sea level), c_p is the specific heat of air ($\sim$1 kJ/kg-K), and A is the cross-sectional area of the beam. [24]
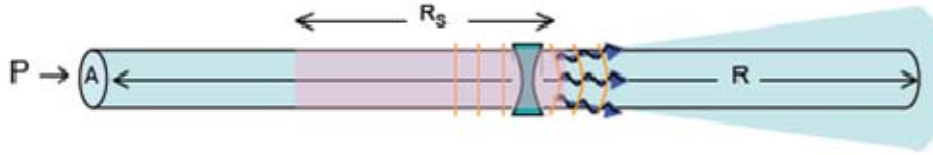
Figure 18.   Thermal Blooming Graphic. From [24]

The increase in temperature leads to a change in the index of refraction of the air according to the formula

$$\Delta n \approx -\left(10^{-6}\middle/\deg ree\_K\right)\Delta T .$$ **(III.11)**

This small change in the index of refraction ($\Delta n = -\Delta v / c$) results in a small velocity difference Δv for light in the middle part of the beam, which is warmer, and the edge of the beam, which is cooler. Thermal blooming is created when this velocity difference allows the wave front to curve by as much as λ over the path length R_s. So, the index change Δn causes thermal blooming when

$$\Delta n \approx -\lambda / R_s,$$ **(III.12)**

where Δn is the dimensionless index of refraction and λ is the laser wavelength in meters. By combining Equations (III.11) and (III.12), we can obtain an equation for the change in temperature that would lead to thermal blooming

$$\Delta T \approx \frac{10^6 \lambda}{R_s} \text{ in degrees K.} \qquad \textbf{(III.13)}$$

Combining Equations (III.10) and (III.13) results in an equation for the time interval until thermal blooming begins

$$\Delta t_B \approx \frac{(2x10^9 \, J/m^3) \lambda A}{\alpha R_s P}, \qquad \textbf{(III.14)}$$

where Δt_B is the time until thermal blooming begins in seconds. [24]

Equation (III.10) approximates the temperature change per second due to the absorption of beam power, and it can be applied to the MW-class FEL. Assuming a power of 1 MW, beam area of about 3.14 m^2, and a stagnation range of 10 km, it predicts a value of 1.08 x 10^{-3} K/sec. This is encouraging, until Equations (III.13) and (III.14) show that thermal blooming might occur for a temperature change as small as 10^{-4} K, and it could begin as quickly as 0.09 seconds after initial illumination. Obviously, this would not allow for sufficient propagation of the beam over long ranges.

Appearing in the numerator and denominator of Equation (III.10), the stagnation range does not affect the rate of temperature change due to absorption. However, it can have a large effect on Equations (III.13) and (III.14). In the case presented above, the initial estimation that the entire atmosphere is stagnant is extremely conservative. There are many variables that affect thermal blooming including the atmospheric density, the velocity of the air, the range of propagation, and the angular rate of the beam as it tracks a target. For the power beaming applications discussed in Chapter V, the laser would sweep across the sky as it tracks a target at an angular rate of approximately 1/2 degree per second. Theoretically, the beam might only experience thermal blooming over very short stagnation ranges close to the director mirror. If this stagnation range was about 100 m, then thermal blooming might not begin until approximately 9 seconds after the first illumination.

Likewise, some of the effects of thermal blooming could be mitigated by locating the ground-based laser in a dry climate at high altitude to reduce the atmospheric absorption, propagation range, and stagnation range of the laser beam. However, for all of the topics within this thesis, thermal blooming effects are mostly ignored to obtain a first approximation of the feasibility of these applications. While the complex issues involved in the atmospheric propagation of the laser are not trivial, over thirty years of research within the military indicates that a high-powered laser can be successfully propagated through the atmosphere. The military has been interested in FELs since 1978, when "the Defense Advanced Research Projects Agency (DARPA) concluded that no other high-power laser could achieve the optical beam quality necessary to focus the beam on a distant (thousands of km) target [26, p. 2–1]." These topics obviously require further study, but for the purposes of this thesis they will be generally excluded from consideration.

THIS PAGE INTENTIONALLY LEFT BLANK

IV.   ORBITAL MOTION

The application of a ground based laser to targets outside of Earth's atmosphere requires a detailed understanding of the variables involved. Both the beam's propagation through the atmosphere and the motion of the target are critical to the design of an integrated system. In most of the applications discussed here, the target will be a satellite or satellite debris in Earth orbit; therefore, an understanding of orbital mechanics and the space environment will be required. This chapter will describe the basic laws of orbital motion and describe the forces that act on an orbiting object. A general comprehension of the relative magnitudes of the perturbing accelerations is conceptually important. Chapter VI will attempt to utilize some of the perturbations generated or altered by a ground-based laser to modify the orbits of space debris. Specifically, the laser may be able to increase the aerodynamic drag forces on orbital debris by altering the orbit of the debris through vaporization of a small amount of surface material, break-up of the debris into smaller particles, and radiation pressure. While most of the other perturbation effects will not be specifically calculated in later work, many of them are utilized within the code of the Satellite Tool Kit (STK) program.

A.   BASIC THEORY

Despite their limited tools, ancient astronomers accomplished many insightful discoveries regarding the motion of celestial bodies, but prior to the 1600s, most of these discoveries amounted to cataloging and describing specific interactions, such as predicting the changes in lunar phases, solar eclipse cycles, and the phases of Venus and other nearby planets. Building on the Copernican, heliocentric model of the solar system and Tycho Brahe's very precise observational data, Johann Kepler produced a work, *Astronomica Nova (New Astronomy)*, that would finally capture the kinematics of planetary motion and lay the foundation for the field of orbital mechanics. Any review of two-body, Keplerian, mechanics requires a familiarity with these laws.

Kepler's Laws:

1) Law of Ellipses: An orbit is an ellipse, or conic section, with a central body at one focus.

2) Areal Law: An orbiting body's radius vector from a central body sweeps out equal areas in equal times.

3) Harmonic Law: The square of an orbiting body's revolutionary period is proportional to the cube of the satellite's mean distance from the central body.

In the early 1700s, Galileo Galilei provided an approximate value for the acceleration due to gravity, stating that two bodies dropped simultaneously would fall at the same velocity independent of their masses. While Kepler described kinematic motion that details the motion of objects without consideration of the causes leading to the motion, Galileo took the first steps into orbital dynamics and attempted to describe the causes of orbital motion. Synthesizing Kepler's laws and Galileo's terrestrial mechanics, Sir Isaac Newton discovered the universal law of attraction and proposed the three fundamental laws of classical mechanics. When combined with Kepler's laws, Newton's second law and his universal law of gravitation are the starting points for any modern study of orbital motion [27, p. 29–31].

Newton's Laws:

1) The Law of Inertia: Every body continues in its state of rest, or of uniform motion in a straight line, unless it is compelled to change that state by forces impressed upon it.

2) The Fundamental Law of Dynamics: The change of motion is proportional to the motive force impressed and is made in the direction of the right line in which that force is impressed

3) The Law of Action and Reaction: To every action there is always opposed an equal reaction: or, the mutual actions of two bodies upon each other are always equal and directed to contrary parts.

B.   GRAVITATIONAL THEORY

Despite the intricate models that have been developed to compute the motion of satellites to the required accuracies for various applications, the main features of their orbits may still be described by a few simple and reasonable approximations. In the same way that the Sun primarily governs the motion of the planets, Earth's gravitational force exceeds all other forces acting on a satellite by several orders of magnitude. As a first approximation, Kepler's laws of planetary motion, Newton's classical mechanics, and Newton's law of gravity may be applied to a satellite's orbit about the Earth. Ignoring, for the moment, the perturbative forces upon a satellite due to their relative insignificance, the "two-body" solution to orbital motion can be developed. In this case, the satellite's mass is negligible when compared to the mass of the Earth, and the Earth and satellite are assumed to be spherically symmetric and of uniform density. In its simplest form, the acceleration ($\ddot{\vec{r}}$) of the satellite is given by Newton's law of gravity

$$\ddot{\vec{r}} = -\frac{\mu}{r^2}\hat{r} \; ,$$
(IV.1)

where μ is Earth's gravitational parameter ($\sim$398,600 km^3/s^2), r is the distance from the center of the Earth to the center of gravity of the satellite in km, and $\hat{r}$ is a unit vector along that path. [28, p. 15]

In this case, the satellite is confined to orbit in a fixed plane, since the gravitational force exerted on the satellite always points towards the center of the Earth. Following the derivations outlined in [28, p. 15-19], the velocity (v_{sat}) and period (T_{sat}) of a satellite in this simplified orbit is given by

$$v_{sat} = \sqrt{\mu\left(\frac{2}{r} - \frac{1}{a_s}\right)} \text{ and}$$
(IV.2)

$$T_{sat} = 2\pi\sqrt{\frac{a_s^3}{\mu}} \; ,$$
(IV.3)

where a_s is the orbit's semi-major axis, given by

$$a_s = \frac{h^2}{\mu\left(1-e^2\right)} \,, \tag{IV.4}$$

where h is the specific angular momentum and e is the eccentricity of the orbit. For a circular orbit where $r=a$, Equations (IV.2) and (IV.3) simplify to

$$v_{sat} = \sqrt{\frac{\mu}{r}} \quad \text{and} \tag{IV.5}$$

$$T_{sat} = 2\pi\sqrt{\frac{r^3}{\mu}} \,. \tag{IV.6}$$

The equations presented above outline the acceleration and related variables caused by a simplified, central potential. A more accurate solution of the acceleration due to Earth's gravity can be described by treating the Earth as an oblate spheroid and expanding the geopotential to higher degrees of accuracy.

Envisioning a summation of the gravitational attraction between all of the discrete point masses that make up the Earth and the satellite's mass, an expression for the geopotential emerges that has no known closed-form solution. An expansion of the terms can be accomplished using a series of Legendre polynomials and spherical harmonics. Spherical harmonics represent periodic boundary solutions on a unit sphere, and in this case, Zonal, Sectoral, and Tesseral Harmonics attempt to describe the complex distribution of mass within the Earth. As shown in Figure 19, Zonal harmonic terms are axially symmetric about the earth's polar axis of rotation, and they represent the flattening of the Earth due to its rotation and other latitudinal mass distributions. Sectoral harmonics divide the Earth along longitudinal meridians, and they take into account the extra mass distributions in longitudinal regions. Tesseral harmonics "checker" the Earth in an attempt to model specific local regions that depart from the unit sphere [29, p. 509–520].
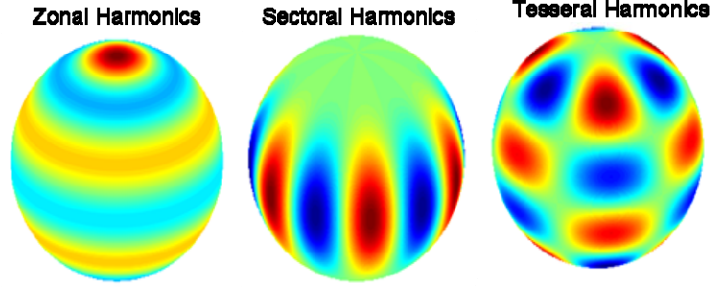
Figure 19.   Spherical Harmonics. After [30]

Ignoring the tidal variations in the terrestrial mass distribution and the variation in the direction of the Earth's axis of rotation, the central potential can be written as

$$U(r,\Lambda,\Phi) = \frac{\mu}{r}\left\{ \begin{array}{l} 1 - \sum_{l=1}^{\infty}\left(\frac{R}{r}\right)^{l} J_{l} P_{l}\left(\sin\Phi\right) \\ + \sum_{l=1}^{\infty}\sum_{m=1}^{l}\left(\frac{R}{r}\right)^{l}\left[C_{lm}\cos\left(m\Lambda\right) + S_{lm}\sin\left(m\Lambda\right)\right]P_{lm}\left(\sin\Phi\right) \end{array} \right\} , \textbf{(IV.7)}$$

where r, Λ, and Φ are spherical coordinates related to the x, y, and z Cartesian coordinates by

$$x = r\sin\Lambda\cos\Phi , \qquad\qquad \textbf{(IV.8)}$$

$$y = r\sin\Lambda\sin\Phi , \qquad\qquad \textbf{(IV.9)}$$

$$z = r\cos\Lambda , \qquad\qquad \textbf{(IV.10)}$$

R is the equatorial radius of the Earth, l and m are counting variables, the $P(\sin\Phi)$ terms are Legendre polynomials, and J, C, and S are harmonic coefficients. In Equation (IV.7), the first term represented by the number one, describes only the dominant central potential causing Keplerian motion. The second term, with J_l and P_l, displays the contribution of the zonal harmonics. The third term, with C_{lm}, S_{lm}, and P_{lm}, provides the contribution of the sectorial and tesseral harmonics. This expansion is discussed here to familiarize the reader with the even terms of J that can be some of the larger perturbation forces affecting an object at low altitude. The additional terms not discussed above, such as the C_{11}, S_{11}, and J_3 terms, are negligible when modeling the actual mass distribution of the Earth, but the interested reader can find a full derivation and discussion in [27, p.67].

Neglecting the expansion of the geopotential and the perturbing forces described in Section D, the fundamental equations of Keplerian motion, supported by Newton's second law, can generally describe the motion of any orbiting object over a limited number of orbits. As discussed in Section E, the acceleration created by this basic Newtonian acceleration is about three orders of magnitude greater than the J_2 term in the expansion of the geopotential or the highest feasible perturbation due to atmospheric drag. As orbital passes build, the detailed geopotential expansion and perturbation effects must be used to account for variations in the orbital motion from that predicted by Kepler and Newton.

D.   ORBIT TYPES

The orbital profile of any satellite has profound implications for its mission performance, service lifetime, electrical power, overall weight, thermal gradients, launch costs, and a variety of other critical factors. In addition to the complexities of systems engineering, there is a nearly infinite number of possible orbits for a satellite designer to consider during the design process. Among the thousands of satellites in orbit, however, there emerges a general catalog of useful orbits. There are four basic orbit types described below.

The radiation environment near the Earth can be highly damaging to a satellite's solar cells. It consists of electrons and protons trapped in the geomagnetic field, radiation generated by solar flares, and cosmic radiation. Within Earth's magnetosphere, trapped electrons and protons within the Van Allen belts cause most of the damage to solar cells. Outside of the magnetosphere, the solar flare protons are the predominant cause of solar cell degradation. Figure 20 shows a cross section of the Earth's magnetosphere, illustrating the trapped electron and proton flux. Due to its highly damaging effects on solar cells, the center of the proton belt, between 6,000 and 12,000 km, is generally avoided by all solar powered spacecraft, creating an artificial gap between useful Low Earth Orbits (LEO) and Medium Earth Orbits (MEO) [31, p.327].
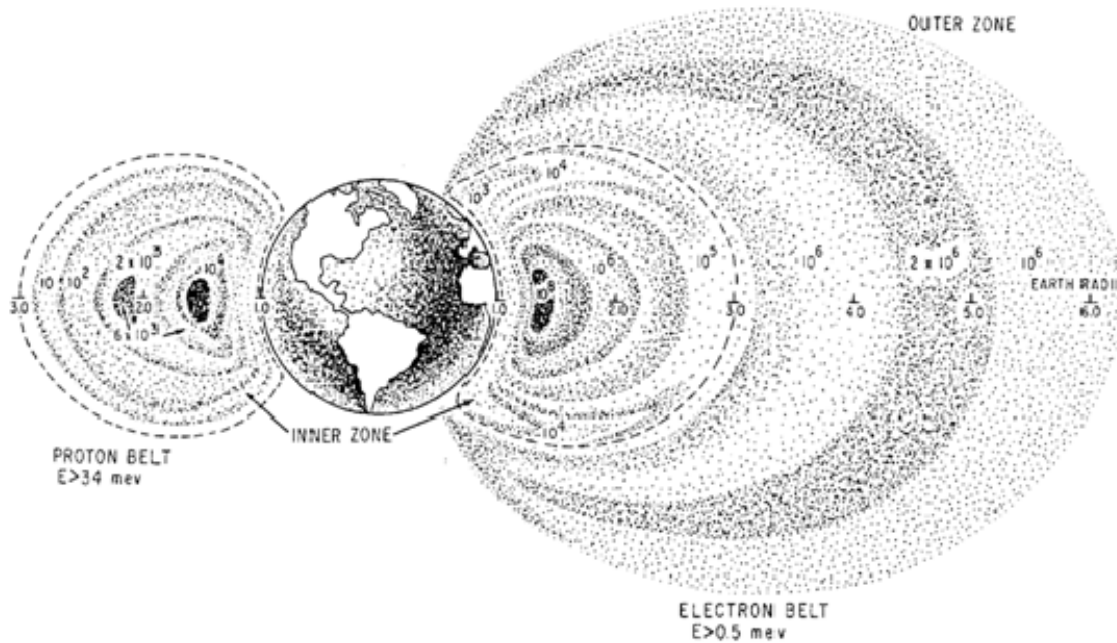
Figure 20.   Earth's Van Allen Belts. From [32]

1.   Low Earth Orbit (LEO)

Any orbit with an altitude less than 1000 km is categorized as a Low Earth Orbit (LEO).   Due to their low altitude, satellites in LEO are subjected to significant atmospheric effects such as orbit degradation due to atmospheric drag and material degradation due to erosion or chemical interactions with the upper atmosphere, but they can often avoid the high electron and proton flux of Earth's Van Allen Belts [33].   A typical LEO satellite has an orbital period of about an hour and a half to a few hours, but it can only be seen from a particular terrestrial location for a few minutes as it passes overhead.   For this reason, it is common to operate "constellations" of multiple LEO satellites spaced in appropriate orbits to provide frequent or continuous coverage of critical locations [34].

LEO offers many advantages over other orbits, but all LEO satellites benefit from the relatively low launch costs when compared to higher altitude orbits. With less fuel required to reach LEO altitudes, high orbital inclinations and even retrograde orbits are much more accessible for LEO spacecraft. While maintaining a higher viewpoint and

wider field of view than reconnaissance aircraft, remote sensing satellites in LEO are able to quickly cover large portions of the Earth's surface and still maintain better resolution than satellites at higher altitudes. Communications satellites, such as Iridium or Global Star, benefit from the lower altitudes with increased signal strength and shorter transmission delays.

2. Medium Earth Orbit (MEO)

Any orbit with an eccentricity less than 0.5 and an orbital altitude between 1000 km and about 35,786 km is generally categorized as a Medium Earth Orbit (MEO). MEO satellites can have orbital periods between 2 and 24 hours. MEO is highly utilized by space-based, navigation satellites such as the Global Positioning System (GPS), Glonass, or Galileo systems, but some communications satellites that cover the North and South Pole are also in MEO [34].

At higher altitudes than LEO, MEO satellites can cover more of the Earth's surface with fewer satellites while avoiding the atmospheric drag and deterioration of materials. Similarly, MEO satellites experience shorter average eclipse times than LEO satellites, thereby simplifying the electrical power requirements of the spacecraft. Generally, launch costs to MEO are slightly more affordable than GEO and allow for larger spacecraft for the same launch vehicle. Depending on the specific orbit and altitude, MEO satellites can experience very high proton and electron flux within Earth's Van Allen Belts [33].

3. Highly Elliptical Orbit (HEO)

A Highly Elliptical Orbit (HEO) is an orbit with an eccentricity larger than 0.5 [34, p. 6]. HEO is commonly used as an intermediate transfer orbit for satellites on their way to geosynchronous orbits via Hohmann transfer, but there are some specialized scientific and communications applications. During its twelve hour orbit, a HEO satellite will dwell for approximately nine hours near apogee before sweeping through perigee in the remaining three hours of the orbit. HEO satellites typically degrade faster than MEO or GEO satellites due to the atmospheric drag during their transit near perigee, so some

fuel is usually reserved to extend the operational lifetime through regular orbit maintenance maneuvers. Like MEO satellites, HEO satellites can experience very high proton and electron flux within Earth's Van Allen Belts depending on their specific orbital profile [33].

For scientific applications, HEO orbits allow for measuring detailed cross sections of interesting phenomena. By transiting across a large range of geocentric distances out to twenty Earth radii, these satellites produce volumes of data on the structure and composition of Earth's magnetosphere and the solar-terrestrial interaction. As shown in Figure 21, specially designed 12-hour, "Molniya" orbits are commonly used to provide long dwell times over high northern latitudes where the coverage by GEO satellites is limited. The same principle could be used over any latitude of specific interest. By carefully matching the inclination (± 63.4 degrees) and eccentricity of these orbits, engineers establish an orbit that keeps the argument of perigee constant, i.e., the latitude at which apogee occurs does not vary. Satellites in Molniya orbits dwell over the northern hemisphere during the orbit, allowing for excellent coverage of the northern latitudes with fewer satellites in a constellation. As its name suggests, this is a standard orbit for Russian communications satellites [35].
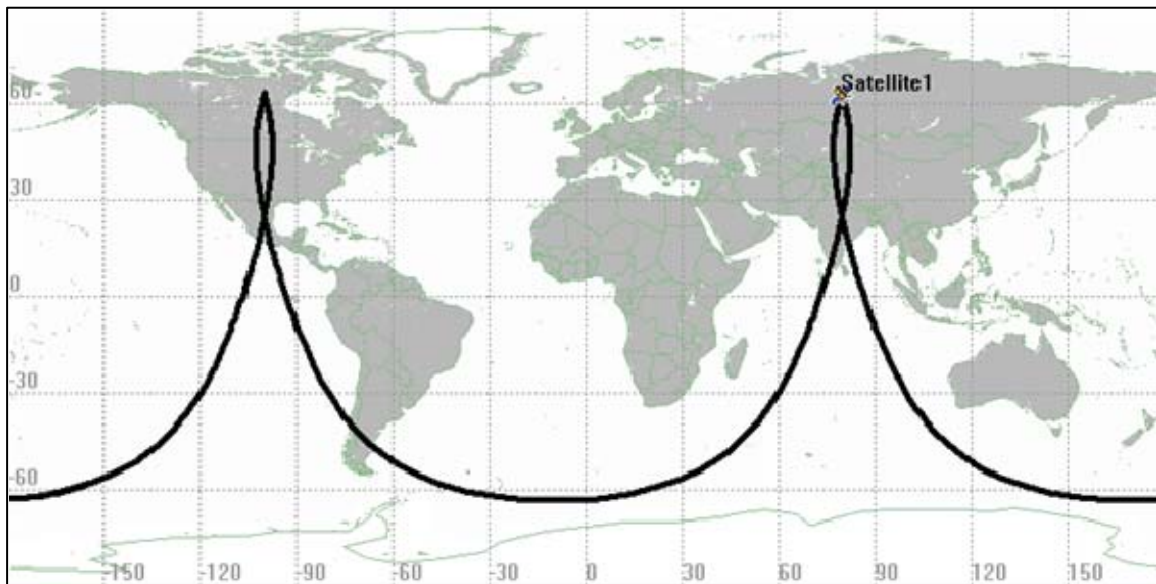
Figure 21.   Molniya Ground Track

4. Geosynchronous Orbit (GEO)

GEO satellites circle the Earth at a fixed altitude of 35,786 km and have a period of 23.9345 hours, or a sidereal day, matching the time it takes for the Earth to rotate a full 360 degrees. The satellite's velocity at this altitude matches the Earth's rotational rate, thereby keeping the satellite over a specific location on the Earth's equator and creating a satellite ground track in a "figure-eight" pattern on that location. A geosynchronous orbit with zero inclination is generally referred to as a geostationary orbit as it will orbit directly above a point on the Earth's equator with no North/South displacement. Many satellite communications systems utilize geostationary satellites, which appear stationary to a ground observer, to eliminate the need for tracking systems in the ground receivers [34].

The concept of geosynchronous spacecraft was first proposed by Arthur C. Clark in 1945, more than a decade before Sputnik 1, the first satellite, was launched. Clark correctly deduced that a system of three satellites in geosynchronous orbit would have simultaneous coverage over nearly the Earth's entire surface. This makes the GEO belt an optimum orbit for any application seeking to minimize the number of satellites for global coverage; however, there can be significant transmission delays due to the large transmission distances involved.

GEO is highly populated by many communications, weather, and remote sensing satellites. Satellites at GEO experience much shorter average eclipse times than satellites at lower altitudes and generally avoid the high proton flux existing within Earth's Outer Van Allen Radiation Belts [33]. As discussed in Chapter V, GEO satellites spend most of the year in full sunlight and only experience eclipses near the spring and autumn equinoxes with each eclipse lasting about 70 minutes, or 5% of the orbital period. GEO satellites tend to be very large due to the much greater transmission losses experienced by their communications systems at this distance, and their cascading effect on the required antenna, electrical, and attitude control system sizes.

Examples of the orbits discussed above and "typical" satellites within those orbits are outlined in Table 5.

Orbit	Low Earth Orbit (LEO)	Medium Earth Orbit (MEO)	Highly Elliptical Orbit (HEO)	Geosynchronous Earth Orbit (GEO)
Typical Satellite	Landsat 7	GPS 2-27	Russian Communications Satellites	TDRS-7
Apogee altitude	703 km	20,314 km	39,850 km	35,809 km
Perigee altitude	701 km	20,047 km	500 km	35,766 km
Period	98.8 min	12 hr	~12 hr	24 hr
Inclination	98.21 deg	54.2 deg	63.4 deg	2.97 deg
Eccentricity	0.00010760	0.00505460	0.741	0.000765

Table 5.   Typical Orbit Parameters. After [35, p. 115]

E.   PERTURBATIVE FORCES

While the original laws discovered by Kepler and Newton accounted for the primary acceleration within a satellite's orbit, there are many other conservative and non-conservative perturbative forces that affect the motion of an orbiting body. Equations (IV.1) through (IV.6) assumed that the Earth and satellite were spherically symmetric and of uniform density and completely ignored the usually minor effects of the other perturbative forces. These simplifications are generally valid for most applications where a limited number of orbits are involved or only a rough idea of the satellite track is required, but for high accuracy applications, such as power beaming, orbital debris clearance, or illuminating extraterrestrial bodies, perturbations on orbital motion must be taken into account.

Similarly, it can be an egregious error to assume that perturbative forces are always small. Atmospheric drag during reentry and the second body gravitation in the restricted three-body problem are prime examples of a perturbative forcing growing to match the primary attractive force. Whenever they are this large, they are no longer termed "perturbations," because the fundamental nature of the problem has changed. In

this paper, the perturbative accelerations are discussed because the removal of orbital debris, covered in Chapter VI, depends upon increasing the atmospheric drag of the debris particles.

All of the significant accelerations that will affect an orbiting object are discussed in the following sections and displayed in Figure 22 on a log-log scale. At the top of the plot, the gravitational acceleration due to a uniformly spherical Earth (labeled GM) is three orders of magnitude larger than the other accelerations. The J_2, J_4, and J_6 lines display the harmonic expansions of the geopotential. The odd zonal harmonics have no temporal effect on the Keplerian motion of a satellite, and they are not included here [27, p. 92]. J_2 represents the Earth's equatorial bulge due to its angular momentum. While atmospheric drag and lift are virtually non-existent above 1000 kilometers, it can even exceed the gravitational potential at altitudes below a few hundred kilometers, allowing for winged flight within the atmosphere. As an important note, the gravitational attraction due to the Sun, Moon, and other planets produces the only accelerations with positive slope, i.e., their forces increase as the distance from the Earth increases. The Solar radiation pressure generally drops with distance from the Sun, but on the scales shown here, it remains virtually unchanged. Overall, the Tidal, Relativistic, and Albedo perturbations remain fairly low and trend together.
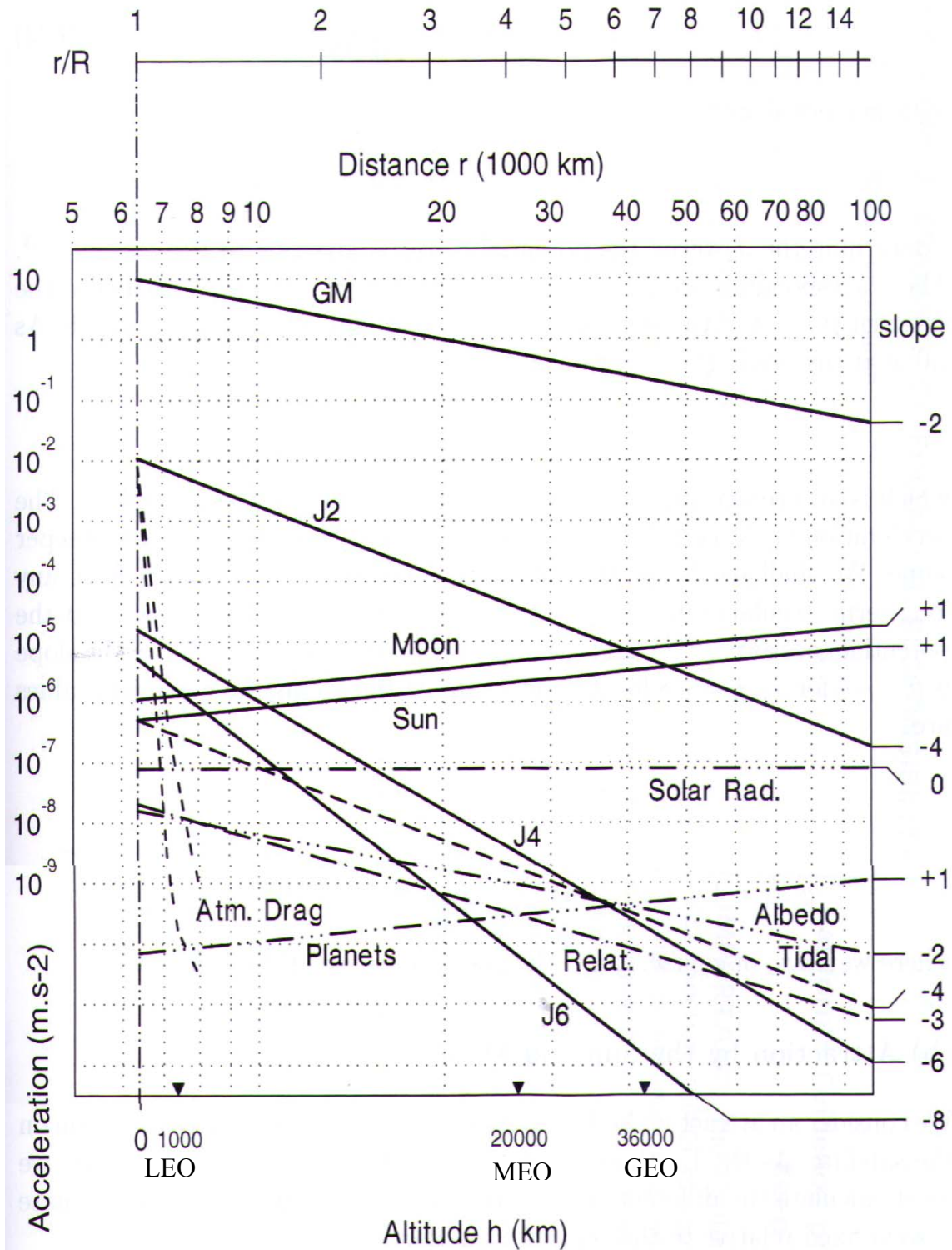
Figure 22.   Central and Perturbative Accelerations. From [27, p. 69]

1. Conservative Perturbations

a) Attraction by the Earth

As described by the geopotential expansion shown above in Equation (IV.7), the acceleration due to Earth's gravity is an extremely complex variable to determine. Each expansion term adds a level of precision by accounting for increasingly subtle differences in the mass distribution of the Earth. The Newtonian central acceleration (GM) is inversely proportional to the radius squared, and therefore it is represented in the log-log plot by a straight line of slope $s=-2$. The J_2 acceleration term, representing the Earth's oblateness, is inversely proportional to r^4, and it is represented in the plot as a straight line with slope $s=-4$. The other high order harmonic terms (J_n) are inversely proportional to $r^{(n+2)}$, and they have a slope $s=-(n+2)$.

b) Attraction by the Sun and Moon

While a satellite obviously experiences acceleration due to the gravitational attraction of the Sun and the Moon, the Earth is also affected by their gravity, and therefore, it is the differential attraction felt by the satellite that must be accounted for here. Due to its proximity, the Moon exerts the largest, non-terrestrial acceleration on the satellite- followed closely by the gravitational acceleration due to the Sun's extremely large mass. In general, the Lunar and Solar differential accelerations increase with orbital altitude because the average gravitational attraction to them increases.

c) Attraction by Other Planets

Planetary perturbations of Earth-orbiting satellites are small and vary with the orientation of the planets, with Venus usually providing the largest contribution, and they can cause no significant uncertainty in the Keplerian orbit [27, p.71]. At much greater ranges than the Moon and lower relative mass than the Sun, the other planets exert a differential, gravitational attraction similar to that described above, but it is at least 1000 times less than the Solar or Lunar accelerations.

d) Tidal Elements

The gravitational attraction of the Moon, Sun, and other planets also affect the Earth's oceans and crust, causing tidal variations in the liquid and solid mass distribution of the Earth. The Earth's crust can raise and fall with an amplitude of as much as one decimeter, affecting the gravitational potential almost ten times more than the ocean's tides [27, p. 71]. The tidal acceleration is significantly greater at lower altitudes as the range is lower and the angular differential due to the displaced mass is larger.

e) Relativistic Effects

While satellites orbit at speeds well below relativistic velocities, Einstein's relativity provides a small correction to the Newtonian equations of motion resulting in equally small changes in the Keplerian motion of the spacecraft. Since they are about six orders of magnitude less than the J_2 acceleration, these changes are generally negligible over a few orbits, but they result in a secular effect on the argument of perigee. Over multiple orbits the perigee of an orbit will change more rapidly than classical calculations alone would predict.

2. Non-Conservative Perturbations

a) Atmospheric Drag

For satellites in LEO, friction with the molecules of residual atmospheric gases can provide significant decelerations. These perturbations are extremely difficult to model since they require a detailed model of the upper atmosphere, which varies according to solar and geomagnetic activity. They also depend heavily on the spacecraft's size, configuration, surface materials, and orientation with respect to the direction of travel. The acceleration due to atmospheric drag can be computed using

$$\vec{a}_d = -\frac{\rho v_{rel}^2}{2}\left(\frac{C_D A_{sc}}{m_{sc}}\right)\hat{i}_v \ , \qquad \textbf{(IV.8)}$$

where ρ is the atmospheric density, v_{rel} is the velocity of the spacecraft relative to the atmosphere, C_D is the dimensionless atmospheric drag coefficient (a function of the satellite's shape), A_{sc} is the spacecraft's effective projected area, m_{sc} is the spacecraft mass, and $\hat{i}_v$ is a unit vector of the spacecraft velocity relative to the atmosphere.

b)   *Radiation Pressure*

The actual radiation pressure experienced by a satellite depends heavily upon its size, configuration, and surface materials. A satellite in Earth orbit experiences three significant radiation pressures- Solar, Albedo, and Earth's Infrared. Naturally, there is no Solar or Albedo acceleration when the satellite is in eclipse. Solar radiation pressure, due to the Sun's direct illumination of the satellite, is inversely proportional to the squared distance to the sun, and it is therefore largely independent of satellite altitude. The Albedo radiation pressure, due to the direct reflection of the Sun's rays off of the Earth's surface, is inversely proportional to the squared orbital radius, but it can vary greatly due to the extreme variations in Earth's surface emissivity. Earth's Infrared (IR) radiation pressure, due to the emission of Earth's heat in the IR spectrum, varies like the Albedo, but it can affect a satellite even in eclipse [27].

3.   Other Perturbations

The list above does not constitute an exhaustive listing of the perturbations that affect an Earth orbiting satellite, but it represents the largest contributors to variations in the predicted Keplerian motion. There are many other physical and theoretical perturbations, such as: the thermal re-emission of radiation absorbed by the satellite, which usually occurs in an anisotropic way due to the variations in emissivity and surface temperature; micrometeorite drag, due to the impact of micrometeorites; the Poynting-Robertson effect, due to the fact that even if incident radiation emits isotropically, it only does so in the satellite's reference frame; additional general relativistic perturbations; and the theoretical emission of gravitational waves, which is many orders of magnitude less significant than the other examples provided [36].

62

V.   POWER BEAMING TO SATELLITES

While Chapter IV described the orbital motion of a satellite, Chapter V investigates the use of a ground-based, high-energy FEL, propagating through the atmosphere, to power orbiting satellites. In the design of a satellite, the electrical power system typically receives the highest priorities for redundancy, testing, and safety margins [31, p. 326]. Of all the systems onboard, it is the first to be placed in operation, and it remains in service for the entire life of the mission. It serves as the literal heart of a spacecraft, pumping power to every other system and allowing for their operation, and when it inevitably fails, the spacecraft fails with it.

The frequent eclipses suffered by every satellite in LEO place a very high strain on the electrical power system, and they can drastically affect the battery and spacecraft lifetime. During the design phase, the projected number and length of eclipses over a satellite's design life begin a process driving the size, weight, complexity, and final cost of the satellite into an ever increasing spiral. The concept of beaming power from the Earth to a satellite via a high-energy laser has been suggested as an optimal solution to minimize the depth of discharge on every orbit, and thereby reduce the battery and solar array size, the spacecraft mass, and the overall complexity of the satellite. Unfortunately, this concept requires a considerable, and ultimately impractical, ground infrastructure. The ground tracks of most satellites vary considerably from pass to pass, and it requires a large number of ground stations to ensure reliable power for every nighttime pass.

Although it may seem desirable, power beaming will not be able to provide the constant and economical coverage that is required to meet most of a satellite's power requirements in the foreseeable future. Another futuristic, but more realistic, potential for the power beaming concept resides in the ability to improve a satellite's design lifetime in certain specific orbits, such as a sun synchronous orbit. For a sun-synchronous orbit, the orbital profile is highly regular, and, therefore, it would probably be the least complex application of power beaming. For this specialized orbit, it might be possible to utilize fewer ground stations, thereby reducing the overall investment in ground infrastructure.

By reducing the battery's depth of discharge in every orbit, this sun-synchronous, power-beaming system could allow for a smaller and lighter electrical power system. The cost savings for extending the lifetime of an individual spacecraft can be significant, but additional cost benefits could be realized by designing smaller and lighter spacecraft and using a less capable and cheaper launch vehicle. Current launch costs to LEO are approximately \$8,400/kg [44, pg. 178]. If consistent power beaming allowed for a satellite design with 10% less mass, then a 450 kg satellite might save about \$833,000 in launch costs. Despite these considerable savings for an individual spacecraft, the large ground infrastructure required for effective power beaming can only become economical when applied to satellites on a grand scale. Even for a typical LEO satellite constellation of ten-to-twenty spacecraft, the cost of infrastructure required to support a worldwide capability for power beaming is prohibitive. So, it may only be cost effective to support a full ground based infrastructure as a national or corporate enterprise (by servicing more than one constellation of satellites).

Currently, the U.S. Navy has funded the development of a 100 kW class FEL with intentions to pursue the creation and deployment of a MW class laser for shipboard use [37]. Presumably, the lasers onboard these ships would remain deployed and operational, and for the majority of the time, their lasers would not be occupied by combat operations. Although a ship in a maritime environment would operate under less than ideal conditions for long-range, atmospheric propagation, a deployed fleet of naval vessels with MW-class FELs might be the preferred terrestrial infrastructure for powering critical government, military, or communications satellites in specialized orbits or during emergent situations. For military or national security applications, payloads must typically restrict their operations during eclipse due to their limited battery power. The ability to power critical missions during eclipse might have a considerable effect on battle-space awareness or control. In special cases, the additional power during eclipse could allow for critical communications during wartime or additional imaging by remote sensing satellites. In emergency cases, power beaming may even assist in the recovery of satellites that have lost attitude control, failed to fully deploy their solar panels, or are otherwise unable to maintain their solar panels in a sun-soaking orientation. Earth-based

lasers could provide additional irradiance to the spacecraft, helping to provide useful power and heat while engineers attempt to recover the craft.

A.   ECLIPSE DISCUSSION

The fraction of time that a satellite spends in sunlight and eclipse is important to the design of the electrical power and thermal systems. Depending on the time of year, orbit, and spacecraft age, there can be significant differences in a satellite's eclipse profile and power budget, so a spacecraft is typically designed for maximum eclipse and minimum sunlight at the end-of-life (EOL). Thus, every satellite is over designed for all other conditions within its mission lifetime. Similarly, the orbital and eclipse periods determine the total number of battery cycles and depth of discharge per orbit, which are directly related to the battery lifetime.

The typical eclipse profile of a low earth orbiting satellite in a circular orbit at 400 km altitude and zero degrees inclination is shown in Figure 23. This plot displays the angle from the orbital plane to the sun (β_s), or "beta angle," overlaid with the angular radius of the Earth from the altitude of the satellite's orbit. For an orbit at zero degrees inclination, the beta angle will merely vary with the seasonal variation of the Sun's declination ($\pm$ 23.5 degrees), and at 400 km, the Earth's angular radius is approximately 70 degrees. When the beta angle is inside the Earth's angular radius (plotted in red), the satellite will pass through the Earth's shadow during each orbit, and the absolute difference between the values is proportional to the length of each eclipse. When the beta angle is outside of the Earth's angular radius, the satellite will not enter Earth's shadow, remaining in full sunlight for every orbit. As shown in Figure 23, this LEO satellite will pass through eclipse on every orbit throughout the year although at some points of the year the time in eclipse will be less than others.
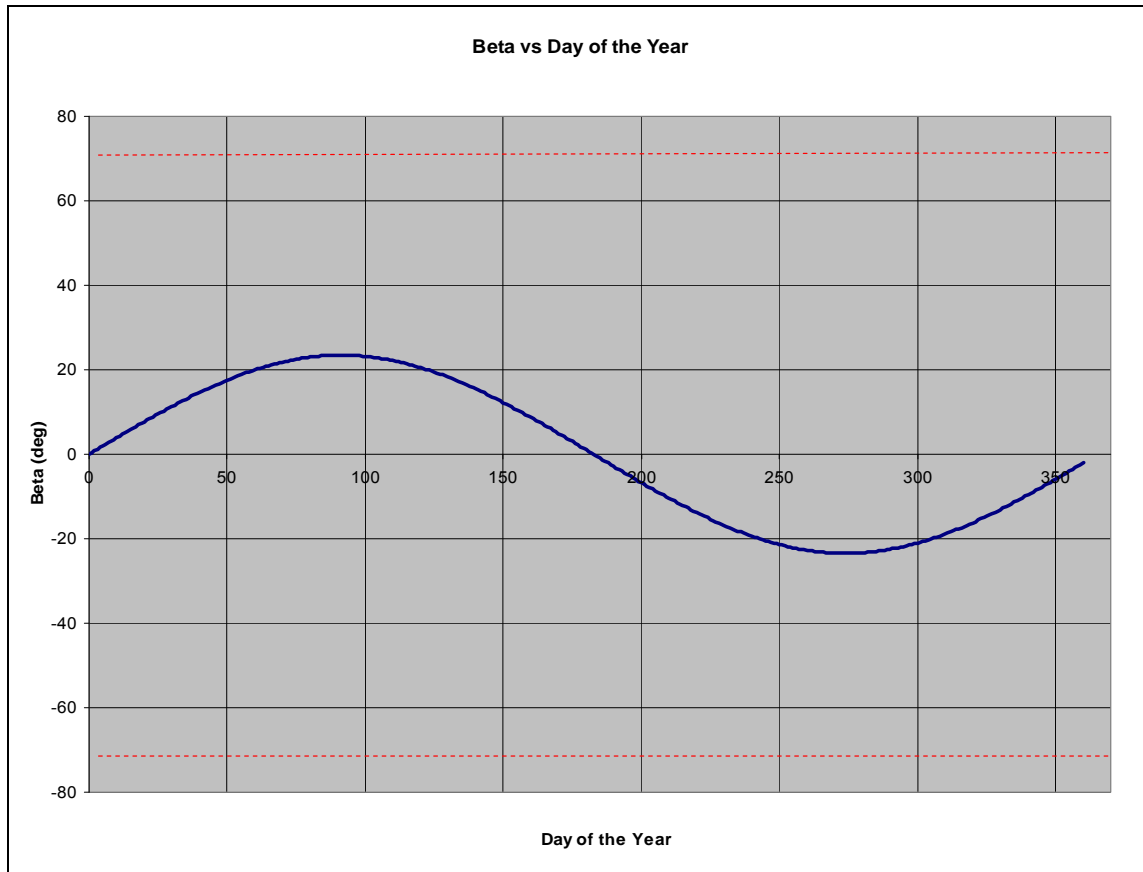
Figure 23.   LEO Eclipse Profile Zero Degree Inclination. After [38]

In Figure 24, the typical eclipse profile of a LEO satellite in a circular orbit at 400 km altitude and 65 degrees inclination is plotted. In this plot, the precession of perigee for the orbit combines with the seasonal variation in the Sun's declination to produce about 30 days without eclipse for the satellite, and for some of the year, the satellite experiences much shorter eclipses than those faced by the LEO satellite with zero inclination.

In contrast to the eclipses experienced by LEO spacecraft, the graph of a typical geosynchronous spacecraft shown in Figure 25 shows that it will only suffer eclipses during about three months of the year, and these eclipses are very short compared to the overall orbital period. Since most GEO satellites orbit near zero inclination, the beta angle varies with the seasonal variation in the Sun's declination, but at GEO altitudes, the angular radius of the Earth is only about 8 degrees.

66
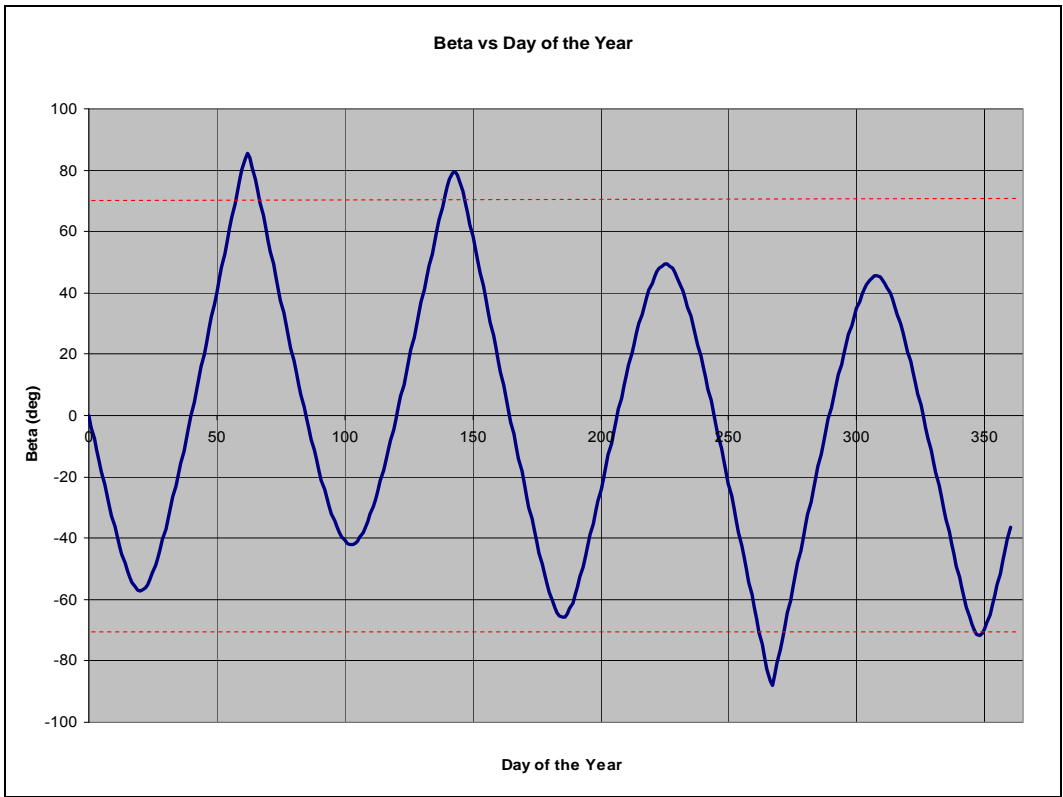
Figure 24.   LEO Eclipse Profile 65 Degree Inclination. After [38]
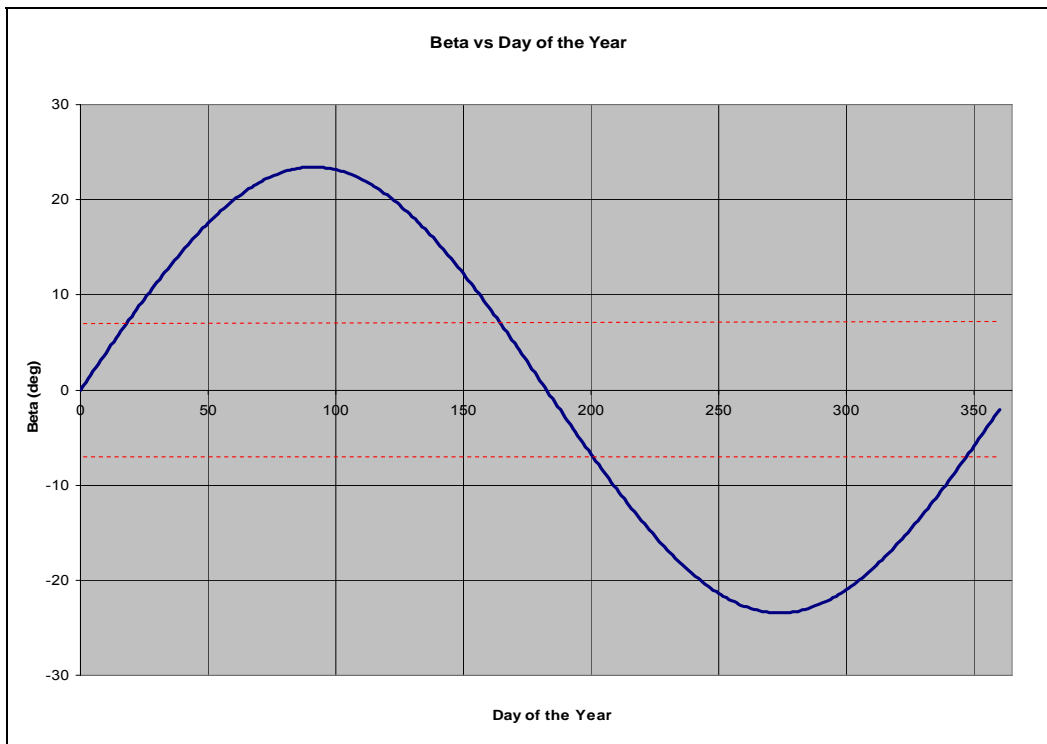
Figure 25.   GEO Eclipse Profile. After [38]

67

Figure 26 shows the proportional time in eclipse for each orbit discussed above. In a LEO spacecraft, eclipse can be as much as 36 minutes out of a 90-minute orbit (eclipse for 39% of each orbit), and, depending on the mission, power budget, and battery type, the spacecraft may not recover a complete charge prior to the next eclipse. For a GEO spacecraft, the eclipse can last as long as 70 minutes out of a 1436-minute orbit (eclipse for ~5% of each orbit), and the satellite can easily recover a complete battery charge prior to the next eclipse. In both cases, power beaming could limit the cyclical stress on the electrical power system, but each orbit type has individual advantages. With eclipse times almost twice as long as a LEO satellite, a GEO satellite with a similar mission and loads would need a much larger battery.
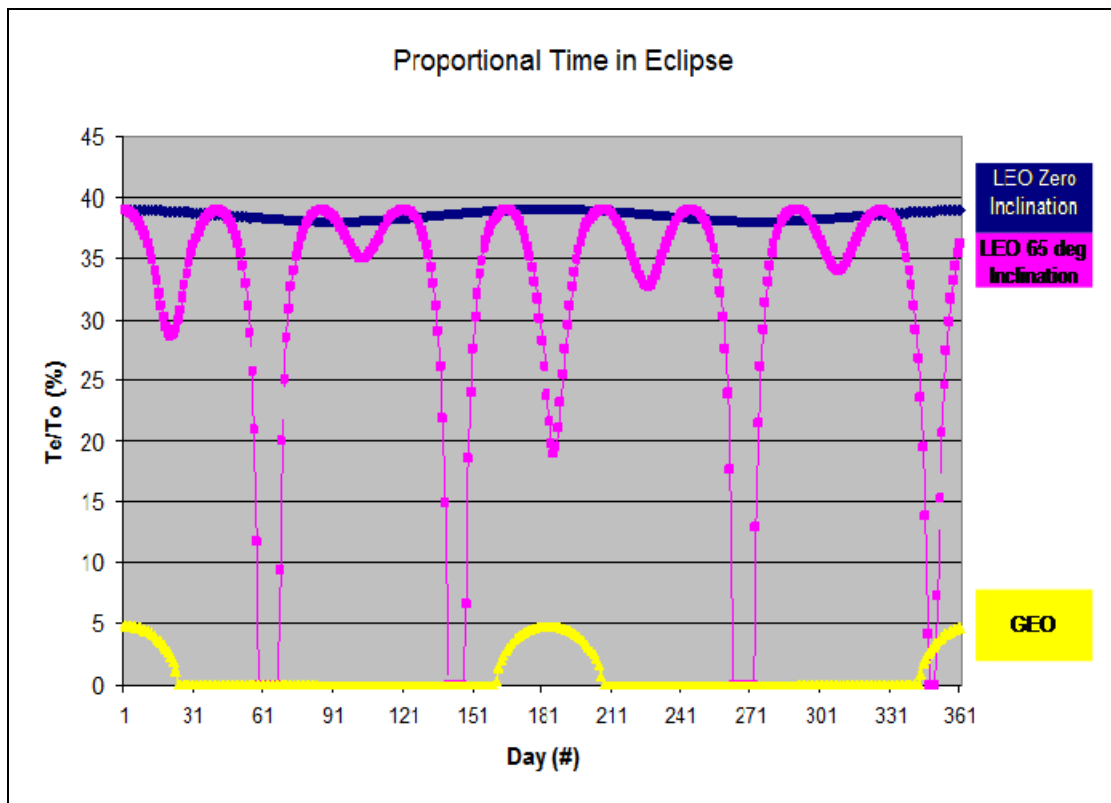
Figure 26.   Proportional Time in Eclipse for LEO and GEO Satellites

B.   POWER BUDGET

When designing a spacecraft and planning for on-orbit operations, all of the systems and components must be designed to the most limiting case and still be able to meet mission requirements. Since every spacecraft is adversely affected by radiation, eclipses, and other factors while in orbit, this means that the typical spacecraft is launched with enough excess capacity at beginning-of-life (BOL) to ensure that it can meet all mission requirements at end-of-life (EOL), when the solar cell and battery efficiencies have degraded.

Shown in Figure 27 is an approximate power budget, or skyline chart, for an imaging satellite, displaying the expected systems in operation and power required for each system over one orbit. The peaks in Figure 27 can be directly related to battery capacity and solar cell sizing as these components must supply the power to meet all of the requirements placed upon them during eclipse or sunlight. The average spacecraft spends its time in the sun operating the payload, communicating with ground stations, and power soaking the solar arrays to charge the battery in preparation for the anticipated battery discharge during eclipse. During this power soaking, or sun soaking, of the solar arrays, the satellite maintains an orientation that maximizes the solar illumination of the solar arrays. While changing orientation for communications, imaging, or sun soaking, the satellite's attitude control system utilizes power to point the spacecraft. During eclipse, the satellite's thermal control system operates extra heaters to stabilize the temperature of the satellite.

Obviously, the design of the electrical power system and the availability of solar power can considerably limit the operation of a satellite. Remote sensing satellites typically have a restricted window for operating the payload during the daytime, and nighttime operations are tightly controlled due to the limited battery capacity. By continuing the battery charge after a satellite enters eclipse, a laser could potentially improve current satellite operations. The primary difference between the imaging satellite depicted in this figure and a communications satellite is that a communications satellite often has a nearly constant power profile due to the requirement for continuous communications ability, i.e., constant operation of the payload and attitude control systems.
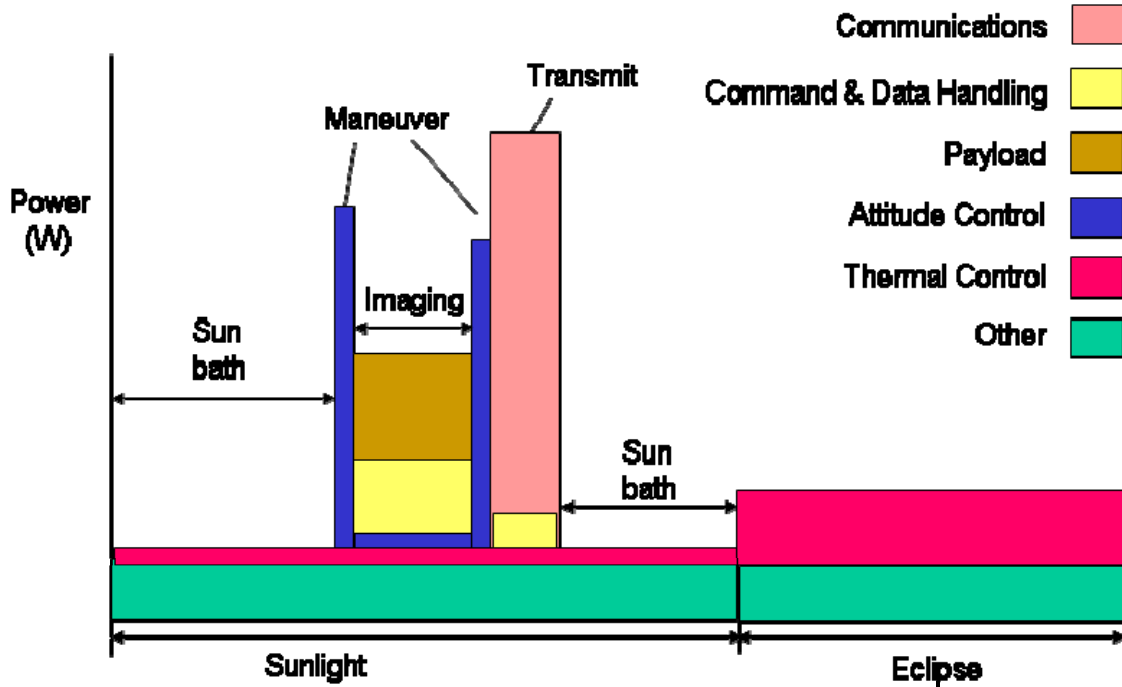
Figure 27.   Generic Power Profile of an Imaging Satellite. After [38]

As mentioned above, the total battery capacity becomes a dominant parameter early in the design phase of a spacecraft, as it must accommodate the power requirements for every component for the entire spacecraft lifetime. In Figure 28, the battery capacity for a typical spacecraft is plotted versus time to display the frequent charge and discharge periods that a satellite battery will undergo. A satellite is not always able to fully recharge its battery to maximum capacity during each orbit. Mission requirements sometimes dictate more frequent payload operation and less time for sun soaking, resulting in an incomplete charge while in sunlight. Likewise, in a process called "battery conditioning," engineers will increase the depth of discharge over a few orbits to preserve the overall battery capacity. Historical failure data suggests that the depth of discharge per orbit and the total number of battery cycles are quite important to the overall lifetime of a spacecraft as they are directly linked to the stresses on the electrical power system.
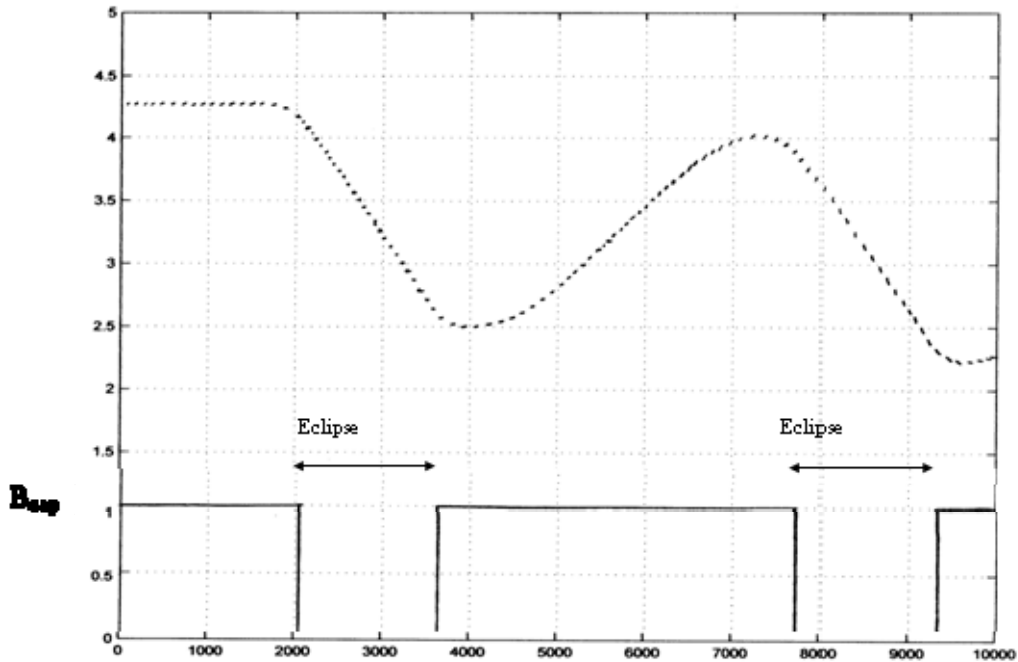
Figure 28.　　　Typical Battery Capacity Graph. From [38]

C.　PHOTOVOLTAIC CELLS

By far the most common method of providing power to a satellite is through the use of solar panels, which utilize large arrays of specialized photovoltaic cells to gather some of the energy provided by the sun's illumination. Photovoltaic cells utilize the photoelectric effect to transform incident electromagnetic radiation into electrical current. Solar cells are photovoltaic cells specially designed to utilize incident solar energy for power, and increasingly, multi-junction solar cells are becoming common in satellite applications. Multi-junction cells attempt to capture more of the energy within the broad solar spectrum by mixing materials with differing band gaps. Regardless of their design, most of the radiation that falls upon a solar cell will always be wasted due to the breadth of the solar spectrum and the limited band gaps of the semiconductor materials. Since their introduction early in the space age, solar cell efficiencies have remained below 20% for most applications with typical values around 15% [39, p. 277].

When designing a photovoltaic cell for laser power beaming, it would be possible to better match the band gap of the cell with the wavelength of the incident laser beam,

thereby reducing excess energy delivered as heat and increasing the overall efficiency of the cell. Photovoltaic cells operating at 800 nm can be subjected to more than five times the natural solar radiation intensity (~1366 W/m^2) without requiring active cooling, and more than 60% efficiency has been demonstrated using Gallium Arsenide (GaAs) cells at this wavelength [39, p. 277]. Generally, the conversion efficiency of a specially designed photovoltaic cell under monochromatic illumination can be two-to-three times greater than a typical solar cell under solar radiation, but even conventional solar cells can benefit from monochromatic illumination. Figure 29 shows a graphic of observed solar cell efficiencies when subjected to monochromatic illumination.
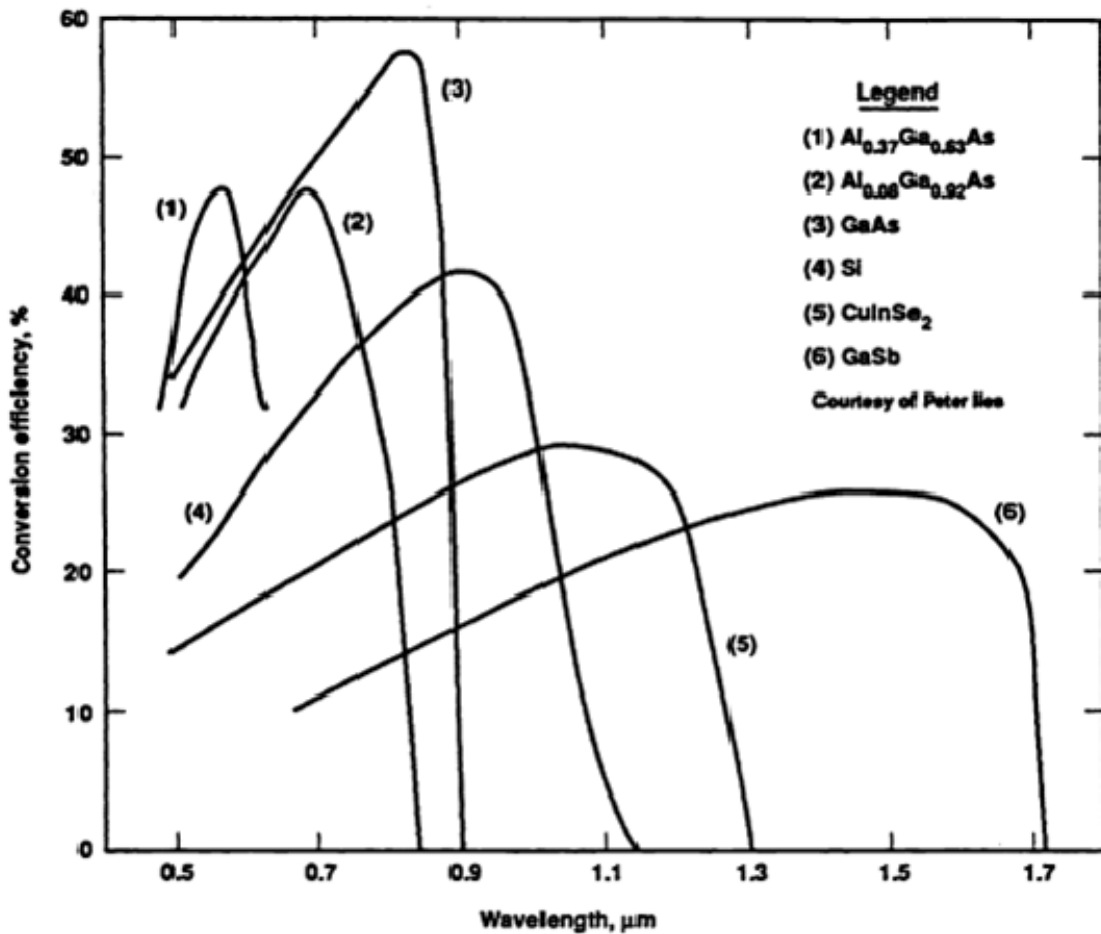
Figure 29.   Solar Cell Efficiencies Under Monochromatic Illumination. From [40, p. 235]

Power beaming has the potential to greatly enhance the power generated by a satellite without increasing the size of the solar arrays. Using the Hubble Space telescope as a typical imaging satellite, a rough comparison of the power generated by solar and laser illumination can be performed. The average solar radiation intensity in Earth orbit is approximately 1366 W/m^2, and the Hubble solar panels occupy a total area of about 38m^2 [41]. Thus, the total power falling on these panels is 52 kW, but even with a generous efficiency of 20%, the solar panels would only provide 10.4 kW of electricity.

By applying the high intensities allowed through monochromatic illumination, a laser could conservatively project more than three times the solar intensity to the solar panels, about 4200 W/m^2, without requiring additional radiators. On the same area, this illumination results in roughly 160 kW falling upon the solar panels, and with an estimated monochromatic efficiency of 50%, the solar panels would generate about 80 kW of electricity. Under monochromatic illumination, the combination of higher cell efficiencies and higher sustainable radiative intensities allows the satellite to generate almost 8 times more power than it could under solar radiation. This additional power could be crucial for specialized applications such as providing a power "boost" to counter jamming of GPS or communications satellites or rapid charging of a satellite's battery during eclipse.

Solar cells experience considerable damage due to the electron and proton flux in Earth orbit and the thermal stresses of frequent heating and cooling. This damage can seriously degrade the EOL efficiency and power output of the solar panels, necessitating larger design margins and solar panels at launch. Some scientists have suggested illuminating solar panels with a high power laser to anneal the cells and repair some of this damage remotely. In this instance, the targeting accuracy of the laser mount and the thermal effects on the rest of the spacecraft body are much more prominent concerns than for power beaming. Otherwise, this application is similar to power beaming with much less frequent access to the spacecraft, i.e., it would be performed infrequently. Thus, only one or two ground sites would need a laser capable of the higher power and better accuracy that is required to support the "repair" illumination.

D.   SOLAR RADIATION SPECTRUM

Although the sun outputs a great amount of energy, it does so across the entire electromagnetic spectrum.   In contrast, the FEL can transmit its energy within a bandwidth of about 0.1% of the wavelength, or about 10^{-3} µm for an FEL operating at 1 µm [15].   The radiation output of the sun can be easily approximated using the Stefan-Boltzman law by assuming that the sun radiates as a black-body radiator at a temperature of about 5800 K.   This temperature approximates the temperatures of the outer visible layers of the sun's corona, those that directly interact with the solar system through radiative means.   The Stefan-Bolztman law is

$$R_{Sun} = \sigma \varepsilon T^4 ,$$ (V.1)

where R_{Sun} is the power radiated in W/m^2, σ is the Stefan-Boltzman constant (5.67 x 10^{-8} W/m^{2}K^4), ε is the emissivity (approximately one for a blackbody), and T is the temperature in K.   Using Equation (V.1) and the assumptions above, the total output power of the sun is approximately 64.2 MW/m^2 at the solar surface.   For the applications discussed here, it may be more useful to know the radiative flux as a function of wavelength since the laser only has to compete in limited bandwidths. [33]

Planck derived an analytical expression for the radiative flux as a function of wavelength for a blackbody,

$$R_{Sun\lambda} = \frac{C_1 \lambda^{-5}}{e^{\left(C_2 / \lambda T \right)} - 1} ,$$ (V.2)

where $R_{Sun\lambda}$ is the blackbody thermal radiation in W/m^2, λ is the wavelength in m, C_1 is 3.74 x 10^{-19} kW-m^2, C_2 is 1.439 x 10^{-2} m-K, and T is the temperature in K [42].   This relation can be used to generate the radiation curve of a blackbody, shown in Figure 30, but it can also be used to determine the sun's power over a limited bandwidth.   In most applications, the laser only has to compete with the sun within its bandwidth or near the band-gap energy of a photovoltaic cell.
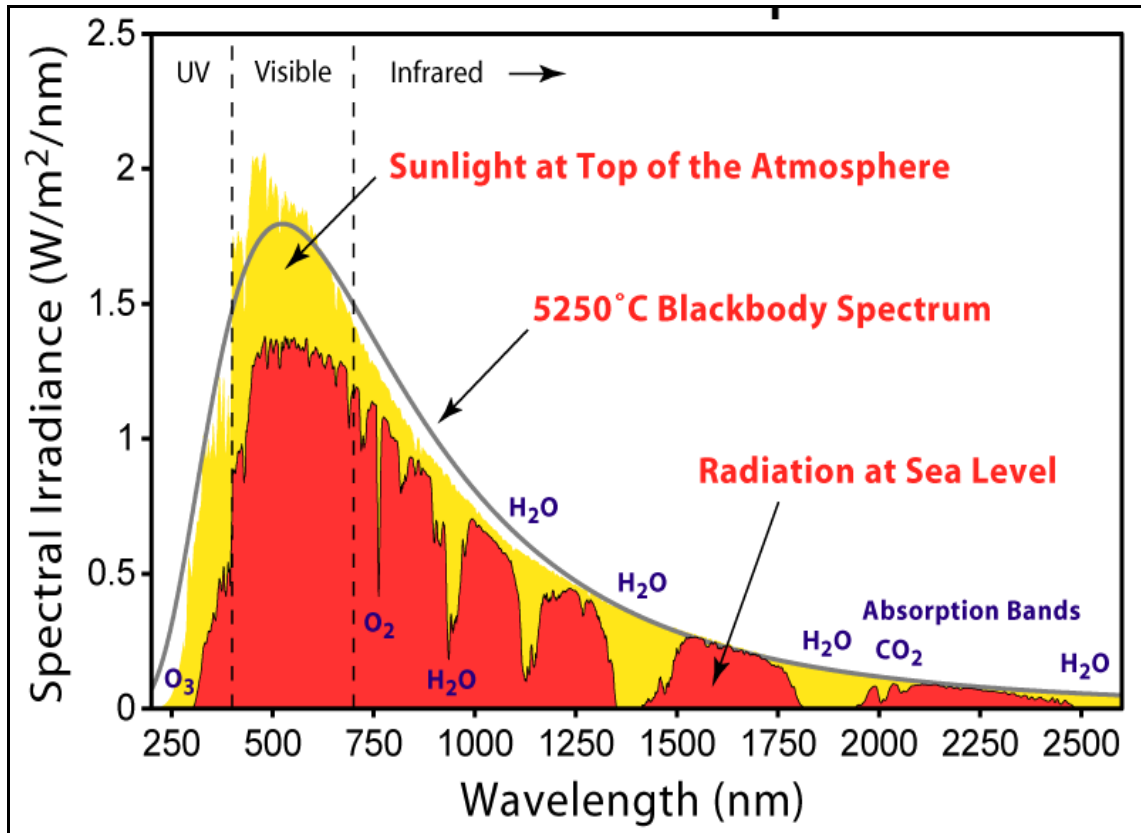
Figure 30.   Solar Irradiance Spectrum. From [43]

Figure 30 above compares the actual irradiance of the sun in Earth orbit, referred to as Air Mass Zero (AM0), over a range of wavelengths to the power profile of the theoretical blackbody radiator.   It also shows the ground level irradiance in red, highlighting the absorption caused by Earth's atmosphere on the AM0 radiation.   As shown above, the actual irradiance is very similar to the blackbody approximation at the wavelengths of interest for high energy applications and atmospheric propagation. Calculations in Chapter VII will utilize the blackbody approximation to determine the sun's output within the laser bandwidth.   While satellites in low earth orbit do operate inside the upper vestiges of the atmosphere, atmospheric effects on incident radiation are generally negligible, and the AM0 solar spectrum can be assumed for most spacecraft.

E.   ATMOSPHERIC PROPAGATION

When attempting the beaming of power from a terrestrial site to an orbiting spacecraft, the absorptive and scattering properties of atmospheric water molecules begin to critically affect laser propagation. As shown above in Figure 16 and Figure 30, the total transmittance of Earth's atmosphere near 1 μm ranges from 50 to 70% of the total transmitted power. Thus for the simulations and calculations in Chapters V, VI, and VII, we must assume that whatever the final output of the laser at the director mirror, only a conservative 50% will pass through the atmosphere. Still, when we compare the anticipated 1 MW output power of a ship-borne FEL to the typical tens of kilowatts required for even the largest spacecraft, this loss will not prevent successful power beaming.

For GEO applications, the laser beam will remain relatively motionless in the atmosphere and could experience thermal blooming. In the LEO case, the angular rate of the laser beam should avoid thermal blooming high in the atmosphere, but thermal blooming could develop in the dense and relatively stagnant sir near the director. Some method of inducing convection near the beam may allow for a reduction in thermal blooming, such as the use of large turbofans to move air through the laser column. This artificially induced "wind" would tend to bend the laser beam which could possibly be corrected by realigning the beam director.

F.   BEAM SPOT SIZE AND INTENSITY

Satellites specially designed for power beaming applications might utilize a single circular photovoltaic panel to assist in laser targeting and reduce illumination of the satellite body, but most currently orbiting satellites utilize dual, sun-pointing solar arrays extending symmetrically from opposite sides of the satellite. Therefore, any power beaming to a generic satellite will have to individually target each solar panel or generate a spot size large enough to illuminate the entire spacecraft body and its solar panels. For a generic, imaging satellite like the Hubble Space Telescope, the total diameter of the beam required to encompass both solar panels is about 13 m [41].

Using Equations (III.1-6), the on-orbit beam radius and intensity of a generic, MW class, ship-borne laser can be estimated without turbulence. The beam radius (w) is given by

$$w(z) = w_o \sqrt{\left(1 + \left(\frac{z}{z_R}\right)^2\right)} \text{ , and} \qquad \textbf{(V.3)}$$

the intensity (I) is given by

$$I = \frac{P}{\pi w^2} . \qquad \textbf{(V.4)}$$

The orbital altitude of a satellite gives the minimum propagation range for a laser engagement, which is assumed to be 400 km for the simulations in this chapter. Figure 67 in Appendix B shows the maximum range of engagement as 1844 km. The beam director, which determines the beam waist radius (w_o), is assumed to be approximately 1 m. This results in a Rayleigh range (z_R) of 3.14 x 10^6 m. For the maximum LEO range of 1844 km, the calculated beam radius at the target is 1.16 m, and for the minimum LEO range of 400 km, the calculated beam radius at the target is 1.01 m. Atmospheric transmission is assumed to be a conservative 50 % of the transmitted power, and the 1 MW of transmitted energy results in about 500 kW of power delivered to the satellite. By diffraction alone, the respective beam intensities for the maximum and minimum range engagements are about 118 kW/m^2 and 156 kW/m^2. A conservative estimation of atmospheric turbulence and thermal blooming might halve these intensities, but this still results in about 100 kW/m^2 incident on the satellite body and solar panels that are designed to receive solar irradiances of ~1.4 kW/m^2 [15].

These intensity values exceed the power requirements of most orbiting satellites by a few orders of magnitude, and they could result in damage to the satellite. Therefore, for power beaming applications, the laser power may need to be lowered or the beam director may need to be redesigned to decrease the beam intensity at the satellite. Fortunately, the FEL is scaleable over a wide power range, and they could be designed to "dial-in" powers between 1 kW and 1 MW [15]. Likewise, the beam director is already

expected to be curved and utilize an adaptive optics system to improve atmospheric propagation effects. On days when turbulence significantly reduces intensity, the MW level FEL can still be effective.

For satellites in GEO, the propagation range is about 35,678 km. By diffraction alone, the calculated beam radius at the target satellite would be about 11.4 m, and the beam intensity is about 1.22 kW/m^2. This is slightly less than the solar intensity, but it may be enough to power vital systems throughout eclipse for most satellites. However, in this case, thermal blooming effects occur much closer to the laser source than to the target, and over these long propagation ranges, they can have a much greater effect on the beam intensity at the target. The combined effects of thermal blooming and turbulence might make power beaming to GEO impractical for beam directors of this size. If the beam director mirror's radius is doubled, then the beam radius at the satellite is halved, and the beam intensity is about 4 times larger than the solar intensity.

In the Hubble example discussed above, a deliberate spreading of the beam to an on-target diameter of 13 m would reduce the overall intensity to about 3.77 kW/m^2, and further atmospheric effects may lead to on-orbit intensities of about 2 kW/m^2. This is only slightly more than the current incident solar irradiation and should be well within the satellite's design tolerances. However, this approach utilizes basic assumptions about atmospheric transmission and a simplistic illumination pattern of the target satellite. Any specific application of power beaming to an orbiting satellite would have to accurately measure and anticipate the atmospheric propagation and model the beam intensity fluctuations across the satellite body to prevent unintentional damage. A dedicated site using a MW-class FEL might use a larger mirror to accommodate smaller spot sizes, and therefore, larger intensities at distant satellites.

G.   SATELLITE THERMAL EFFECTS

Currently, the thermal control system of every satellite is designed to withstand full solar illumination through much of their orbits and possibly even long periods of sun-soaking in a fixed orientation. Thus, the coatings and materials of every satellite surface are carefully analyzed and controlled. Assuming this full solar illumination, the major constraints on the

solar panels are that they have a large enough area to support the satellite loads, battery charging, and some method of aligning themselves to the solar radiation. For a satellite designed for power beaming, a single circular solar panel would be the optimal target for the laser illumination, while still remaining available for the collection of solar illumination. There will be changes to the thermal control system, coatings, and materials of future satellites designed for monochromatic, laser illumination.

The radiative heat sources contributing to a satellite's final temperature are graphically depicted in Figure 31 and included in Equation (V.5). The total heat input to a typical satellite is comprised of terms representing the direct solar radiation, albedo (a reflection of solar energy directly off the Earth), Earth's infrared (IR) radiation, equipment heat dissipation, and solar cell efficiency (since the solar cells turn some incident energy into electricity not heat). The heat input equation is

$$\overset{Input}{Q_{in}} = \overset{SolarRad}{\alpha I_s A_p} + \overset{Albedo}{\rho_a \alpha I_s A F_a} + \overset{EarthIR}{\varepsilon I_{IR} A F_e} + \overset{Equip}{Q_{eq}} - \overset{SolarCell}{\eta I_s A_p f_p}, \quad \textbf{(V.5)}$$

where Q_{in} is the total heat input to the satellite, α is the absorptivity, I_s is the solar irradiance, A_p is the projected area, ρ_a is the albedo factor, A is the surface area, F_a is the Albedo view factor, ε is the emissivity of the surface, I_{IR} is the Earth IR irradiance, F_e is the Earth view factor, Q_{eq} is the heat input due to operating equipment, η is the solar cell efficiency, and f_p is the cell packing factor. In this case, albedo refers to the direct reflection of solar energy off of the Earth's surface, which is differentiated from the general thermal IR radiation of the Earth's IR term [38].
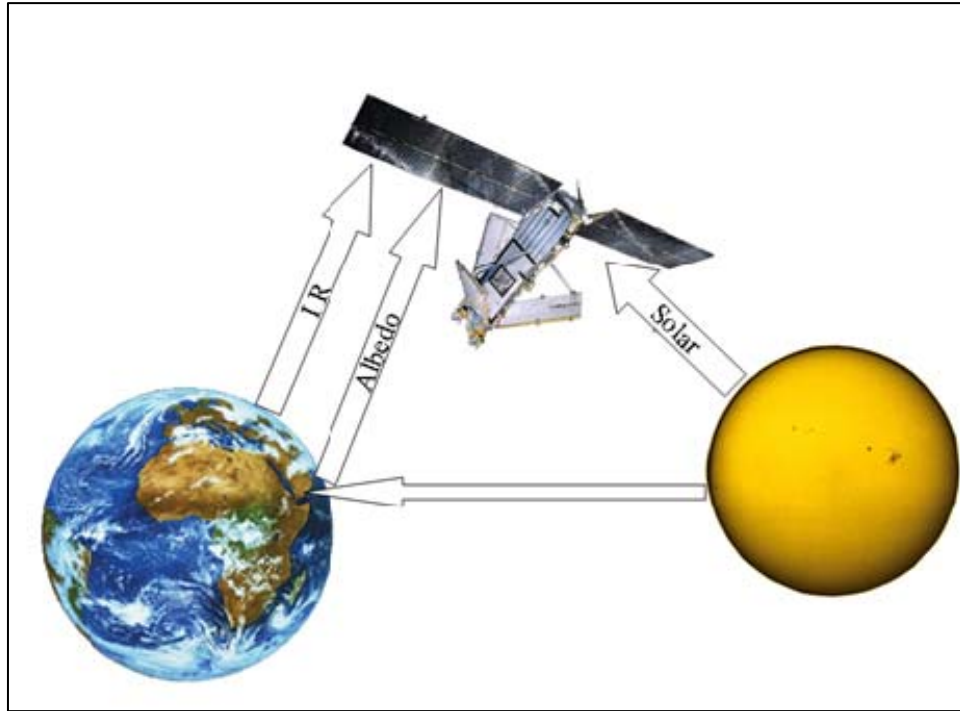
Figure 31.   Satellite Thermal Interactions with the Space Environment

Power beaming during daylight could be useful in propulsion and other specialized applications. If power beaming is conducted while the satellite is in sunlight, then the solar cells would be pointed towards the Earth and operate with a different efficiency under monochromatic illumination. In this case, there is an additional term representing the heat deposited by the laser on the spacecraft and the final term is replaced by the laser energy transformed into electricity by the photovoltaic cells. The heat input equation for daylight power beaming is then

$$Q_{in} = \left\{ \begin{array}{c} \overset{SolarRad}{\alpha I_s A_p} + \overset{LaserRad}{\alpha I_L A_p} + \overset{Albedo}{\rho_a \alpha I_s A F_a} \\ + \overset{EarthIR}{\varepsilon I_{IR} A F_e} + \overset{Equip}{Q_{eq}} - \overset{PVCell}{\eta_{pv} I_L A_p f_p} \end{array} \right\}, \qquad \textbf{(V. 6)}$$

where I_L is the laser irradiance at the target and η_{pv} is the photovoltaic cell efficiency. Power beaming while the satellite is in the sun is a much more complex thermal problem as the satellite will be subjected to illumination due to the sun, laser, albedo, and earth's IR from various angles. As shown in the equations above, thermal control of the

spacecraft depends on the particular absorptivities and thermal conductive properties of the satellite materials, but generally, power beaming to a satellite in sunlight will add significantly to the heat load on the satellite. Therefore, power beaming during sunlight may only be worthwhile for applications that require more power than solar illumination alone can provide, such as for propulsion. Likewise, it is probably feasible only for specially designed satellites with appropriate photovoltaic panels, surface coatings, and possibly extra radiators to dissipate the additional heat deposited by the laser.

The thermal profile of a satellite receiving laser illumination during eclipse would have terms similar to those in Equation (V.5). This equation replaces the solar radiation term with a lasing radiation term, removes the albedo term, and adds a heater term to account for the heat required to maintain safe operating temperatures for equipment. The heat input equation for power beaming during eclipse is

$$\overset{Input}{Q_{in}} = \overset{LaserRad}{\alpha I_L A_p} + \overset{EarthIR}{\varepsilon I_{IR} A F_e} + \overset{Equip}{Q_{eq}} - \overset{PVCell}{\eta_{pv} I_L A_p f_p} + \overset{Heater}{Q_{htr}}, \qquad \textbf{(V. 7)}$$

where Q_{htr} is the heat input by the spacecraft heaters. In this case, the high efficiency photovoltaic cells transform most of the incident radiation that falls on them into electricity, but some of the remaining energy is deposited as heat in the solar panels. Likewise, the beam spot size on-orbit may encompass much of the satellite body, and some of this energy will also be deposited as heat. Certainly, satellite surfaces could be specially designed for higher or lower absorption near the laser wavelengths, but this would require a detailed analysis of the satellite's thermal profile. Reflecting a specific known wavelength from the laser can remove much of the heat absorbed on parts of the satellite other than the photovoltaic panels.

H.   PROPULSION

The current average estimate of launching a satellite to LEO is about $8,400/kg, and the cost for the transfer to GEO using a typical, Hohmann transfer is over $21,000/kg [44, p. 178]. A Hohmann transfer is a method for changing orbital altitude that utilizes two burns on opposing sides of the orbit. Astoundingly, the fuel for a traditional orbital transfer can represent over 50% of the total launch mass of the satellite, which is a

significant use of money and launch assets. In an attempt to lower the traditional cost and risks of launching spacecraft into orbit, NASA has recently funded a space elevator contest to reward the engineering development and practical demonstration of the technologies required to create a robotic climbing vehicle that would ascend an extremely long cable into space while powered by a high energy laser. Some NASA scientists think that it may also be possible to conduct a satellite's transfer from LEO to GEO using a high energy laser to beam power to a "space tug" with an ion thruster engine [45]. This space tug would remain in orbit, reduce launch costs, reduce launch weight, and deliver vehicles to GEO with much more payload mass or station-keeping fuel.

Figure 32 displays the cross sections of the LEO to GEO orbital transfer maneuver using a traditional, (a) Hohmann transfer or (b) the laser-powered, spiral transfer. Unlike the Hohmann transfer, which is traditionally conducted using a liquid fueled engine for two large burns, the Spiral orbital transfer maneuver using an ion thruster provides exceptionally high efficiencies because the specific impulse (I_{sp}) is large. The I_{sp} is proportional to the change in momentum per unit amount of propellant used. The primary advantage of using laser versus solar energy for powering the orbital transfer is in the much larger irradiances and efficiencies that it can provide in lower orbits and the nearly constant power available near GEO. This would allow for a more rapid trip from LEO to GEO, thereby limiting the overall exposure time of the satellite to the high proton and electron flux within Earth's Van Allen Belts and putting the asset into service more rapidly. Laser powered orbital transfers to GEO could last less than a month, which is a much better option than the several month voyage and high radiation levels of an equivalent solar powered system [46, p. 24].
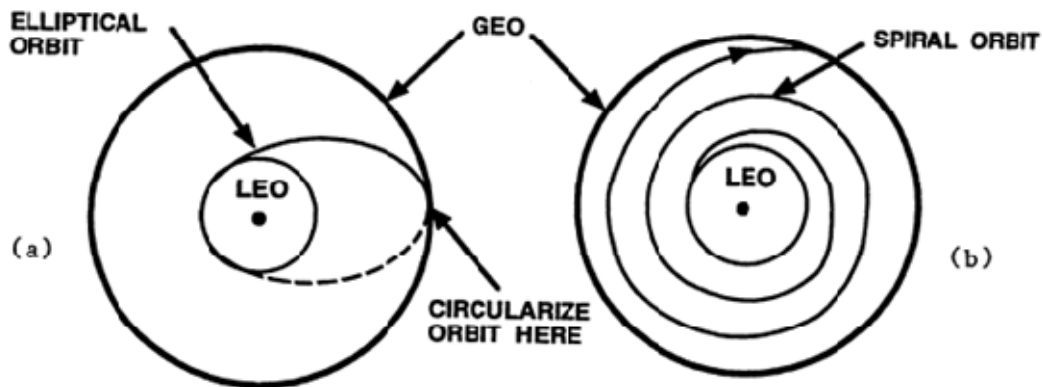
Figure 32.   Hohmann and Spiral Orbital Transfers. From [46, p. 26]

Unlike conventional missions which operate from existing launch pads and benefit from an established ground infrastructure, laser powered propulsion would require a significant initial investment in the ground infrastructure. However, as the number of laser powered missions grows, the cost of the infrastructure is spread among more and more launches and the cost per mission decreases considerably. As shown in Figure 33, a laser powered vehicle offers a much higher effective I_{sp} than conventional vehicles as well as significant savings on the per kg cost of transportation to GEO. Like other spacecraft driven by electric propulsion, a laser powered vehicle would have a high effective I_{sp}, but the laser powered vehicle could presumably use a much smaller and less massive power plant than solar-powered, electrically-driven spacecraft. Therefore, the less-massive, laser-powered spacecraft can have a much larger Δv and transit through the Van Allen Belts more rapidly than other spacecraft using electric propulsion.

- FOUR GROUND SITES
- PAYLOADS: 20 / YR (@ 2500 kg)
- EARTH-LEO LAUNCH COST = $11 K/kg
- LASER POWER VEHICLE, Isp = 2500
- CONVENTIONAL VEHICLE, Isp = 480
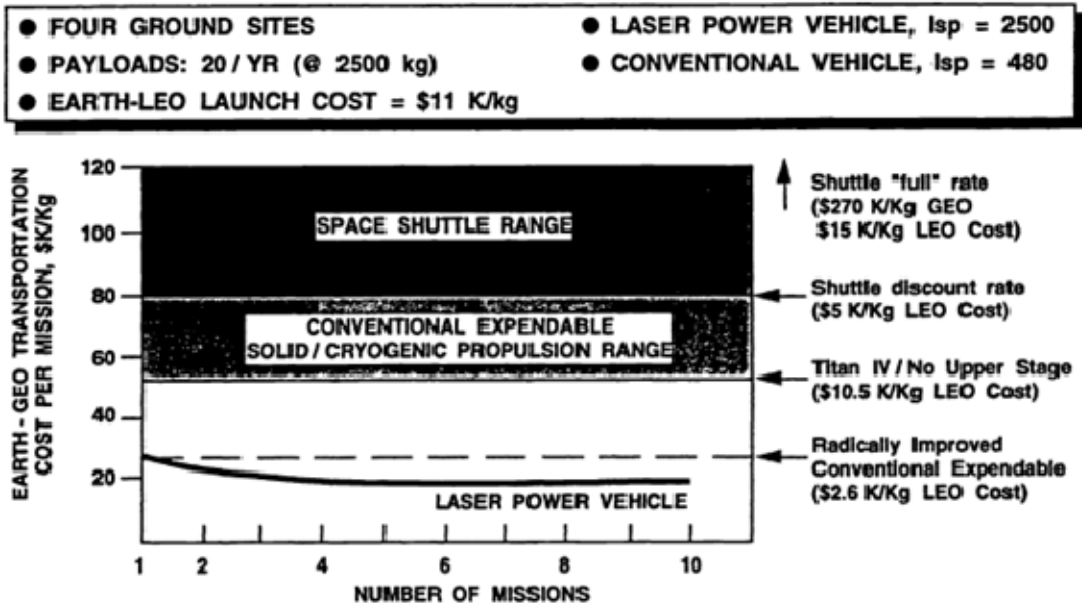
Figure 33.   GEO Transportation Costs. From [46, p. 24]

In one major advantage over conventional launches, the space tug remains useful even after its satellite is delivered to GEO. After undocking, the space tug could be used to de-orbit other satellites at EOL or to collect and de-orbit large pieces of orbital debris. This process could be repeated until the electric drive runs out of propellant. As discussed in Chapter VI, debris in high Earth orbits can remain in orbit for millennia, and it presents a hazard to all future space missions in crossing orbits. At the present time, there are no active methods available for the removal of space debris, only recent procedural changes to minimize their future creation, so this use alone may justify the expense of designing and building a large, terrestrial, power-beaming infrastructure.

I.   CONCEPT OF OPERATIONS

There are many claims within the scientific and engineering communities about the potential applications of power beaming technology. Most of these applications, such as eliminating satellite batteries and powering them through every eclipse, require systems of perfect reliability and immense complexity, and they will remain beyond our capabilities for many years to come. However, there are some applications that would be

well within our technological capabilities assuming the deployment of a MW class laser, and many that could even function with modern lasers in the hundreds of kW range. The primary challenges facing the implementation of these technologies will be the cost, complexity, and safety considerations of building and operating the ground infrastructure for power beaming. In addition to the difficulties of finding a ground site that offers clear viewing conditions, good atmospheric transmission, and a nearby power source capable of supporting a CW, high-power laser, there are significant safety considerations in clearing the local area and airspace prior to firing a high energy laser.

Power beaming, if successfully implemented, offers the potential to improve the entire power budget of the spacecraft during the orbital passes when it receives power during eclipse. Due to the restrictions on the satellite power budget, daytime operations are sometimes limited to allow for enough time to "sun soak" the solar panels and achieve enough battery charge to last through eclipse. By providing illumination during eclipse, the additional power not only aids the nighttime power budget, but it can also allow for a more aggressive usage of the payload during the daylight pass just prior to the over flight of the ship-borne laser.

The United States Navy has recently funded the development of an Innovative Navy Prototype for the MW class FEL, and these systems may be deployed to naval surface combatants within the next twenty or thirty years. While these lasers would operate at sea level in a maritime environment that is not optimal for beam propagation, they would presumably offer the benefits of reliable power, rapid and accurate beam directors, a proven sensor capable of tracking objects in orbit, and mobility. Assuming the successful design, testing, and deployment of these lasers, this thesis models a fleet of up to four ship-borne FELs for power beaming simulations in the Satellite Tool Kit (STK) program. The laser will be assumed to operate at 1 μm with the ability to access any satellite that is at least 10 degrees above the horizon. The lasers will be located at sites that will maximize satellite access in an attempt to "bound the problem" and deduce which applications are most useful or achievable.

J.   SIMULATIONS

Three simulations are illustrated here to determine the useful boundaries and technological capabilities of near-term power beaming applications. For all simulations, the "ground stations" are assumed to be naval vessels equipped with a high energy laser, integrated sensors, and accurate tracking systems, and their locations are chosen for general isolation from inhabited areas and reliable access to the satellite within eclipse. The simulations examine the number and length of nighttime accesses to the satellite to determine whether significant power levels can be delivered to a satellite for specialized operations during eclipse. Laser illumination on the satellite while it is in the daylight may require satellites with special coatings or additional radiators to safely distribute the additional heat load, so daytime illumination is not considered here. These simulations are intended to be applicable to any currently deployed satellite upon the development and deployment of the appropriate lasers to support power beaming.

Other than by locating the lasers in the open ocean, these simulations do not account for the obvious complications of safely firing a high power laser above the horizon. Direct illumination by a laser beam, or even the reflection or scattering of such light, could be highly dangerous for satellites, aircraft, ships, and personnel, and some method of safely "clearing the range" must be established prior to the implementation of these technologies.

1.   Simulation One: The Sun Synchronous Satellite

Simulation One represents the simplest useful case for power beaming, a satellite in a sun synchronous orbit that repeats its ground track daily at the same local times. For this orbit, power beaming could be attempted with a single ground station placed in an advantageous geographic location beneath the ground track where the satellite is in eclipse. This ground station should have reliable and repeating daily access to the satellite while it is in eclipse, but would not have access to the satellite on every eclipse. At most, by selecting a ground station located between two adjacent ground tracks, the laser may be able to power the satellite on two successive passes through eclipse in a critical mission area, i.e., just prior to passing over Asia from the Western Pacific Ocean.

Figure 34 displays the two-dimensional satellite ground track for Simulation One in orange and the access between the ship and the satellite in white. For this simulation, a sun synchronous satellite at 400km altitude, labeled Imager1, with a repeating ground track was created using the STK Orbit Wizard function. The ship, labeled DDL, began the simulation beneath the satellite ground track in the South China Sea, and during the simulation, the ship transits a repetitive track beneath the satellite's nightly over-flight. Specific orbital parameters, ship route, simulation settings, and detailed simulation results are provided in Appendix B.
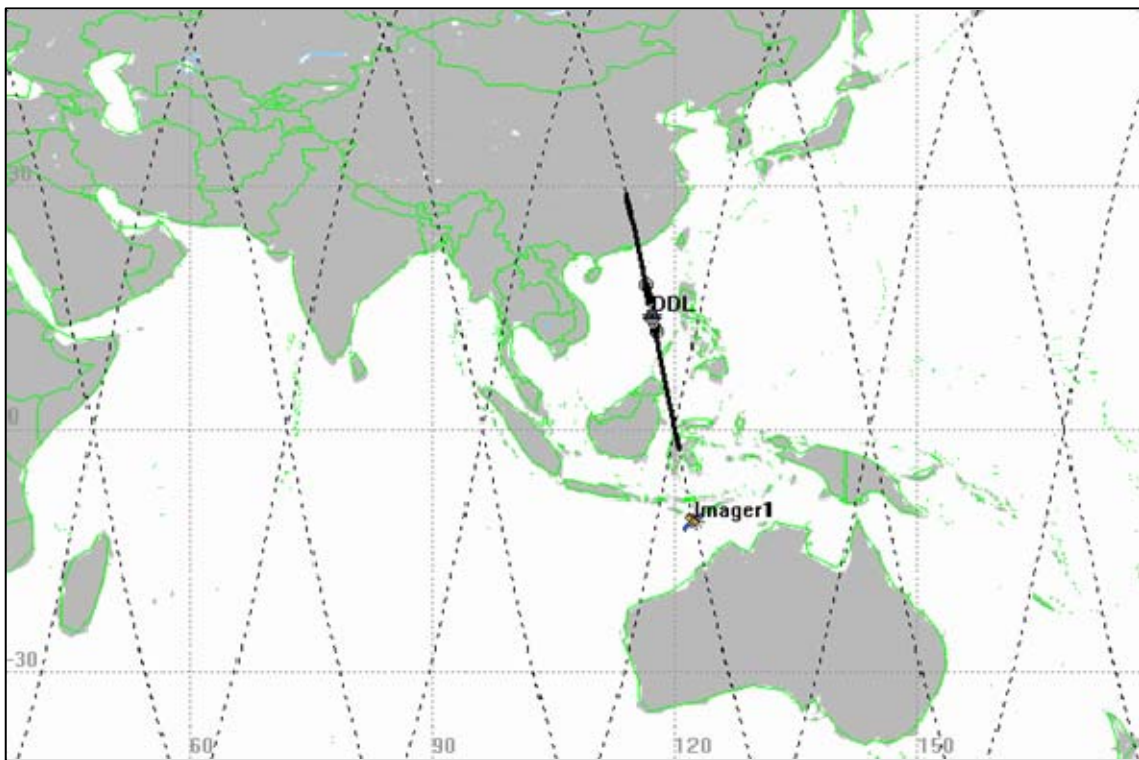
Figure 34.   Two-Dimensional Ship Position, Satellite Ground Track, and Access for Simulation One

Conceptually, the ship is assumed to have access to accurate satellite ephemeris data from an external source in order to acquire and track the satellite in the limited time that the satellite is above the horizon. Thus, the access between ship and satellite was required to be at least ten degrees above the horizon in order to allow for the ship's sensors to gain track and for range safety to avoid possible laser scattering effects.

Similarly, the plotted accesses in this simulation pass over densely populated portions of Indonesia and mainland China. The operation of this laser might be prohibited except in times of war or broad international cooperation due to the hazards it may present to foreign property or populace.

Figure 35 displays the computed satellite access times between the ship and satellite over a one week timeline. As expected for a sun synchronous satellite and a relatively stationary "ground" station, the accesses occur at virtually the same local time every day, while the satellite is in eclipse, and they last for just over 8 minutes each. Thus, for a satellite that experiences just about 36 minutes of eclipse each orbit, the ship can power the satellite for more about 22% of the eclipse period during one orbital pass per day, out of the nearly 16 orbital passes per day. As discussed above in Section C, the satellite may be able to generate power levels as much as 8 times greater than its daytime levels, allowing for continued imaging, communications, or other specialized power boosted modes of operation.

```
Ship-DDL-To-Satellite-Imager1:   Access Summary Report


DDL-To-Imager1
---------------
               Access      Start Time (UTCG)          Stop Time (UTCG)        Duration (sec)
               ------    --------------------      --------------------      --------------
                  1    1 Jul 2007 15:59:44.458    1 Jul 2007 16:07:45.866       481.408
                  2    2 Jul 2007 15:59:40.412    2 Jul 2007 16:07:41.796       481.384
                  3    3 Jul 2007 15:59:36.365    3 Jul 2007 16:07:37.723       481.358
                  4    4 Jul 2007 15:59:32.323    4 Jul 2007 16:07:33.652       481.328
                  5    5 Jul 2007 15:59:28.279    5 Jul 2007 16:07:29.580       481.301
                  6    6 Jul 2007 15:59:24.234    6 Jul 2007 16:07:25.508       481.275
                  7    7 Jul 2007 15:59:20.189    7 Jul 2007 16:07:21.437       481.248

Global Statistics
-----------------
Min Duration      7    7 Jul 2007 15:59:20.189    7 Jul 2007 16:07:21.437       481.248
Max Duration      1    1 Jul 2007 15:59:44.458    1 Jul 2007 16:07:45.866       481.408
Mean Duration                                                                  481.329
Total Duration                                                                3369.303
```

Figure 35.   STK Ship to Satellite Access Report for Simulation One

2.   Simulation Two: Double Access to a Sun Synchronous Satellite

Simulation Two re-creates the same sun synchronous satellite used in Simulation One, but the laser-equipped ship follows a course parallel to the satellite ground tracks to obtain access on two successive nighttime orbits. While Simulation One determined an approximate maximum access for a satellite under ideal conditions, Simulation Two balances the access times on successive orbits to increase the number of nighttime accesses. In this case, the individual access times are slightly less, but this maximizes the ability to fully utilize a satellite during eclipse in one specific geographic region, such as successive orbits over the Korean peninsula and the Chinese mainland.

Figure 36 displays the two-dimensional ground track of the sun synchronous satellite, Imager2, labeled in blue, and the track of the laser equipped ship, DDL2 in yellow. Much like in the first simulation, the actual path of the laser on each access would pass over the inhabited islands of Indonesia and might violate foreign airspace. This presents a significant challenge to the design and implementation of power beaming technology since applications on this scale will certainly require worldwide or at least regional cooperation among our allies. In this case, the same results might be obtained with a ground station in Australia where the central portion of the country is largely uninhabited and airspace control might be achievable.

Figure 36.   Two-dimensional Ship Position, Satellite Ground Track, and Accesses for
Simulation Two

Figure 37 displays the ship to satellite access times over a one week period. As expected, the ship gains access to the satellite twice per day on successive passes with each access lasting just over five minutes. Thus, the satellite only receives about 62.5% of the illumination time provided in each pass by the ideal case in Simulation One, but it still remains illuminated for about 14% of its time in eclipse. Depending on the specific mission, this additional five minutes at the higher powers provided by a monochromatic laser could allow for extra payload operation during eclipse or make up for some extra usage during its time in the sunlight.

```
Ship-DDL2-To-Satellite-Imager2:   Access Summary Report

DDL2-To-Imager2
----------------
              Access      Start Time (UTCG)          Stop Time (UTCG)        Duration (sec)
              ------    ------------------------  ------------------------   ---------------
                 1      1 Jul 2007 14:24:01.810   1 Jul 2007 14:29:17.903       316.093
                 2      1 Jul 2007 15:58:54.750   1 Jul 2007 16:03:55.725       300.975
                 3      2 Jul 2007 14:24:14.246   2 Jul 2007 14:29:30.369       316.123
                 4      2 Jul 2007 15:59:06.362   2 Jul 2007 16:04:09.196       302.834
                 5      3 Jul 2007 14:24:26.643   3 Jul 2007 14:29:42.865       316.223
                 6      3 Jul 2007 15:59:17.934   3 Jul 2007 16:04:22.712       304.778
                 7      4 Jul 2007 14:24:38.996   4 Jul 2007 14:29:55.394       316.399
                 8      4 Jul 2007 15:59:29.470   4 Jul 2007 16:04:36.264       306.795
                 9      5 Jul 2007 14:24:51.313   5 Jul 2007 14:30:07.955       316.642
                10      5 Jul 2007 15:59:40.969   5 Jul 2007 16:04:49.856       308.887
                11      6 Jul 2007 14:25:03.589   6 Jul 2007 14:30:20.547       316.958
                12      6 Jul 2007 15:59:52.428   6 Jul 2007 16:05:03.482       311.053
                13      7 Jul 2007 14:25:15.822   7 Jul 2007 14:30:33.169       317.347
                14      7 Jul 2007 16:00:03.851   7 Jul 2007 16:05:17.145       313.295

Global Statistics
-----------------
Min Duration      2      1 Jul 2007 15:58:54.750   1 Jul 2007 16:03:55.725       300.975
Max Duration     13      7 Jul 2007 14:25:15.822   7 Jul 2007 14:30:33.169       317.347
Mean Duration                                                                    311.743
Total Duration                                                                  4364.400
```

Figure 37.   STK Ship to Satellite Access Report for Simulation Two

3.   Simulation Three: The Mid-Inclination Satellite

Simulation Three simulates a satellite in an orbit with moderate inclination and a variable ground track. This scenario requires more laser "ground" stations and offers less reliable access to the satellite, but these orbits are useful for satellites that are dedicated to global coverage vice repeated surveillance of a particular geographic location.

Figure 38 displays the two-dimensional ship positions, satellite ground tracks, and accesses for Simulation Three. In this simulation, there are four ships spaced evenly around the globe and transiting slowly to the East over the course of the simulation. The ships are labeled DDL1 through DDL4, and their accesses with the satellite are shown as dark black traces over the satellite's ground track. In this simulation, the ships were located so that most of the accesses occur over the open ocean, but there is still some overlapping of foreign airspace over Brazil and Indonesia.
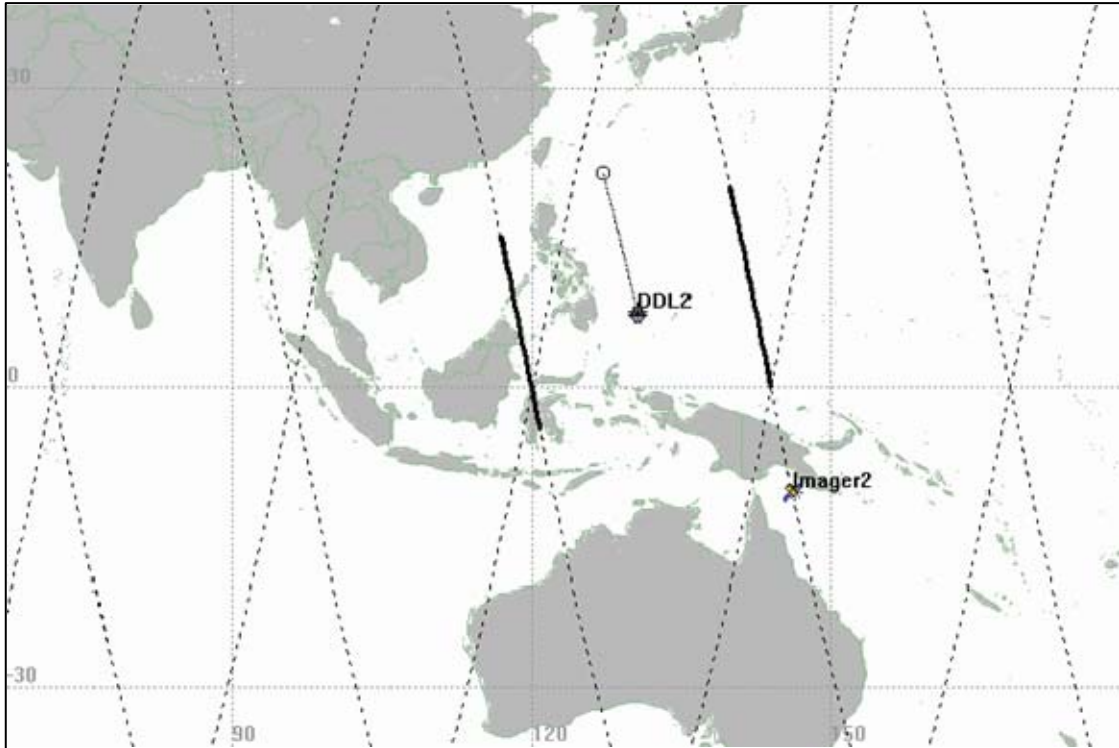
91
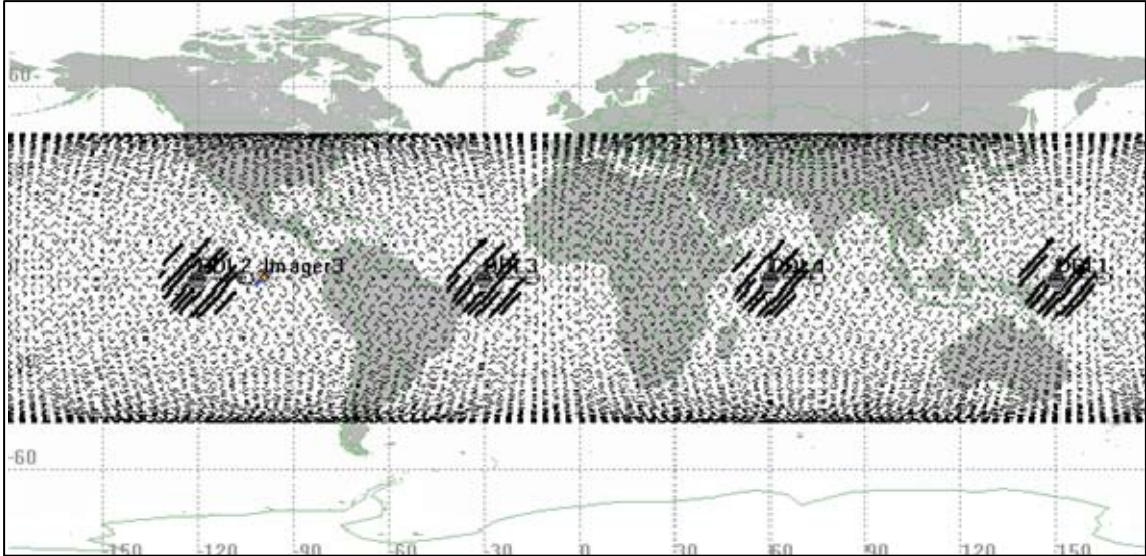
Figure 38.   Two-Dimensional Ship Positions, Satellite Ground Tracks, and Accesses
for Simulation Three

Figure 39 displays the Ship to Satellite accesses for Simulation Three.   As
demonstrated by the comparative size of this table to those of Simulations One and Two,
four ship-borne lasers have the ability to generate a number of accesses to a mid-
inclination satellite over a week of operation.   However, it is important to note that the
first access does not occur until July 2, thus the accesses in this scenario can be irregular
and sometimes infrequent.   With a mean duration of just over 4 minutes, these accesses
would generally deliver power equivalent to the five minute accesses of Simulation Two.
There is considerable variation in the length of each access with a maximum access time
of just over 6 minutes (~389 sec) and a minimum access time of about half a minute (~30
sec).

```
Satellite-Imager3-To-Ship-DDL1, Ship-DDL2, Ship-DDL3, Ship-DDL4:  Access Summary Report

Imager3-To-DDL1    Access       Start Time (UTCG)             Stop Time (UTCG)         Duration (sec)
-----------------  ------    -------------------------   -------------------------    --------------
                     1       2 Jul 2007 18:45:16.396     2 Jul 2007 18:47:52.974          156.579
                     2       3 Jul 2007 17:50:44.542     3 Jul 2007 17:55:54.509          309.967
                     3       4 Jul 2007 16:57:04.960     4 Jul 2007 17:00:34.009          209.049
                     4       4 Jul 2007 18:32:55.365     4 Jul 2007 18:36:25.011          209.646
                     5       5 Jul 2007 17:37:30.311     5 Jul 2007 17:43:54.288          383.977
                     6       6 Jul 2007 16:42:43.643     6 Jul 2007 16:49:00.932          377.289
                     7       7 Jul 2007 15:48:36.730     7 Jul 2007 15:53:26.298          289.567
                     8       7 Jul 2007 17:25:38.845     7 Jul 2007 17:29:50.457          251.612
Global Statistics
-------------------
Min Duration         1       2 Jul 2007 18:45:16.396     2 Jul 2007 18:47:52.974          156.579
Max Duration         5       5 Jul 2007 17:37:30.311     5 Jul 2007 17:43:54.288          383.977
Mean Duration                                                                             273.461
Total Duration                                                                           2187.686

Imager3-To-DDL2    Access       Start Time (UTCG)             Stop Time (UTCG)         Duration (sec)
-----------------  ------    -------------------------   -------------------------    --------------
                     1       2 Jul 2007 12:34:55.166     2 Jul 2007 12:37:44.198          169.032
                     2       3 Jul 2007 11:40:49.218     3 Jul 2007 11:45:35.860          286.642
                     3       3 Jul 2007 13:17:47.977     3 Jul 2007 13:18:18.403           30.426
                     4       4 Jul 2007 12:22:01.078     4 Jul 2007 12:26:17.736          256.657
                     5       5 Jul 2007 11:27:00.407     5 Jul 2007 11:33:28.652          388.245
                     6       6 Jul 2007 10:32:35.802     6 Jul 2007 10:38:12.607          336.805
                     7       6 Jul 2007 12:10:56.429     6 Jul 2007 12:13:19.398          142.970
                     8       7 Jul 2007 09:39:17.486     7 Jul 2007 09:41:47.174          149.688
                     9       7 Jul 2007 11:14:28.388     7 Jul 2007 11:20:03.582          335.194
                    10       8 Jul 2007 10:19:11.655     8 Jul 2007 10:25:39.656          388.001
Global Statistics
-------------------
Min Duration         3       3 Jul 2007 13:17:47.977     3 Jul 2007 13:18:18.403           30.426
Max Duration         5       5 Jul 2007 11:27:00.407     5 Jul 2007 11:33:28.652          388.245
Mean Duration                                                                             248.366
Total Duration                                                                           2483.661

Imager3-To-DDL3    Access       Start Time (UTCG)             Stop Time (UTCG)         Duration (sec)
-----------------  ------    -------------------------   -------------------------    --------------
                     1       2 Jul 2007 06:24:47.830     2 Jul 2007 06:27:35.303          167.473
                     2       3 Jul 2007 05:31:32.442     3 Jul 2007 05:33:54.181          141.739
                     3       3 Jul 2007 07:06:38.518     3 Jul 2007 07:08:10.096           91.577
                     4       4 Jul 2007 06:11:22.597     4 Jul 2007 06:16:10.218          287.621
                     5       5 Jul 2007 05:16:43.221     5 Jul 2007 05:22:50.099          366.878
                     6       6 Jul 2007 04:22:48.129     6 Jul 2007 04:27:02.973          254.844
                     7       6 Jul 2007 05:59:15.154     6 Jul 2007 06:04:02.258          287.104
                     8       7 Jul 2007 05:03:39.609     7 Jul 2007 05:09:56.180          376.571
                     9       8 Jul 2007 04:08:45.672     8 Jul 2007 04:15:10.102          384.430
Global Statistics
-------------------
Min Duration         3       3 Jul 2007 07:06:38.518     3 Jul 2007 07:08:10.096           91.577
Max Duration         9       8 Jul 2007 04:08:45.672     8 Jul 2007 04:15:10.102          384.430
Mean Duration                                                                             262.026
Total Duration                                                                           2358.237

Imager3-To-DDL4    Access       Start Time (UTCG)             Stop Time (UTCG)         Duration (sec)
-----------------  ------    -------------------------   -------------------------    --------------
                     1       2 Jul 2007 00:15:01.067     2 Jul 2007 00:17:26.309          145.242
                     2       3 Jul 2007 00:55:50.285     3 Jul 2007 00:58:01.613          131.328
                     3       4 Jul 2007 00:00:57.016     4 Jul 2007 00:06:02.472          305.456
                     4       4 Jul 2007 23:06:41.111     4 Jul 2007 23:11:55.703          314.592
                     5       5 Jul 2007 00:44:16.835     5 Jul 2007 00:46:32.036          135.201
                     6       5 Jul 2007 23:48:13.699     5 Jul 2007 23:54:06.833          353.134
                     7       6 Jul 2007 22:53:05.286     6 Jul 2007 22:59:34.890          389.604
                     8       7 Jul 2007 21:58:32.745     7 Jul 2007 22:04:27.130          354.384
Global Statistics
-------------------
Min Duration         2       3 Jul 2007 00:55:50.285     3 Jul 2007 00:58:01.613          131.328
Max Duration         7       6 Jul 2007 22:53:05.286     6 Jul 2007 22:59:34.890          389.604
Mean Duration                                                                             266.118
Total Duration                                                                           2128.941
```

Figure 39.   STK Ship to Satellite Access Report for Simulation Three

93

J. DISCUSSION

As demonstrated by the simulations above, the complexities of orbital motion and terrestrial political boundaries present significant challenges to successfully deploying an operational power beaming system. While it is challenging to develop and deploy an integrated power beaming system with dedicated ground stations and specially designed satellites to take advantage of the benefits of monochromatic illumination, an opportunity exists to develop this technology and associated applications incrementally. Assuming the near term deployment of high energy FELs on naval surface combatants, experiments could be conducted at low power over isolated ocean regions to demonstrate the acquisition and tracking abilities of these vessels and the thermal effects and potential power benefits for an orbiting satellite.

The results from Simulation One demonstrate the best case access between a satellite at 400 km and a single ground station. In this case, the ground station is able to deliver useful power levels to a sun synchronous satellite during one orbital pass every day. This additional power could allow operation of the payload during eclipse or decrease the length of required sun soaking in the preceding or following daylight pass, generally increasing the operational use of the payload over one orbital pass. The results from Simulation Two spread the access coverage to two successive orbital passes while only partially decreasing the illumination time. This would allow for more coverage of a general geographic area, i.e., a war zone or disaster site requiring extra communications or imaging. The results from Simulation Three demonstrate that multiple ground stations generate sporadic but generally useful accesses for a satellite at a moderate inclination. As discussed later in Chapter VI, the same accesses could be evaluated for targeting specific orbits to clear orbital debris through laser ablation or vaporization of the debris material. For that application, the length of each access is less important than the number of accesses, and therefore, multiple ground sites spaced around the globe could be a very useful configuration for clearing orbital debris across a wide swath of Earth orbit. Likewise, the clearance of space debris is in the interest of nearly every nation, and therefore, it is the application most likely to generate the international consensus required for the development of a global power beaming capability.

VI.   ORBITAL DEBRIS REMOVAL

While Chapter V investigated the use of a ground-based FEL to extend the life of a satellite through power beaming, Chapter VI will discuss and evaluate the potential application of a high-powered FEL to accelerate the reentry of orbital debris or decrease the risk that they pose to operating spacecraft. There are four primary methods by which a laser could affect orbital debris. First, a laser could be utilized to aid in the detection of non-metallic debris, which is difficult to track with radar, through illumination and optical tracking. Second, a high-peak power laser could ablate a small portion of the surface material, creating a vectored velocity change to lower the perigee of the orbit. Third, a laser could break up the material into less massive pieces with more surface area. This method, however, generates a larger debris cloud and might only be used in lower orbits to ensure the break-up of objects during reentry or to alter the reentry trajectory to an uninhabited area, if possible. Fourth, the laser could be used to heat the debris sufficiently to melt and then boil some of the material. As the debris material boils away, it should be ejected almost isotropically away from the primary body, creating a larger cloud of smaller debris particles, the size of molecules, which pose no risk to spacecraft and de-orbit more rapidly. All of these methods would result in an increase in the atmospheric drag experienced by the debris, and, therefore, accelerate the orbital decay.

A.   BACKGROUND

There are two types of debris in Earth orbit: meteoroids and man-made space debris. Meteoroids are a naturally occurring part of the interplanetary environment that can transit near the Earth at high velocities. Observational estimates indicate that these meteoroids are primarily made up of particles about 0.01 cm in diameter and that they move through Earth's orbital space at an average speed of 20 km/sec [47, p. 3]. Natural debris is usually a "one-time" problem, i.e., the steep trajectories either enter Earth's atmosphere or pass through Earth orbit and return to interplanetary space. In stark contrast to natural meteoroids, virtually all man-made debris, referred to here as orbital debris, remains trapped in Earth orbit until its final reentry into Earth's atmosphere.

Orbital debris is defined by NASA as any man-made object in Earth orbit that no longer serves a useful purpose, including "derelict spacecraft and upper stages of launch vehicles, carriers for multiple payloads, debris intentionally released during spacecraft separation from its launch vehicle or during mission operations, debris created as a result of spacecraft or upper stage explosions or collisions, solid rocket motor effluents, and tiny flecks of paint released by thermal stress or small particle impacts [48]." Most of this orbital debris resides in high inclination orbits with velocities of 7 to 8 km/sec, and it can generate collisions between objects with average relative velocities of 10 km/sec [48]. Consequently, collisions with even small pieces of orbital debris involve considerable energy transfers. For comparison, in 1995, the estimated total mass of all the meteoroids within 2000 km of the Earth's surface was 200 kg, and the estimated mass of orbital debris within the same altitudes was 2,000,000 kg [47, p. 3].

All orbital debris represents risk to current and future space missions, but there are three general categories of space debris, each with its own risk mitigation method. Approximately 19,000 objects larger than 10 cm are known to exist in Earth orbit. About 9,000 of these objects are tracked in LEO and GEO orbits by the United States Space Surveillance Network using radar and optical observations. The orbits of these objects are generally well known, and some spacecraft can maneuver to reduce the chance of collision with them. Particles between 1 and 10 cm in diameter have an estimated population of about 500,000, and most of them are not tracked due to the difficulty of observing them with ground based radars or telescopes. This population estimate is generated by the intermittent radar detection of objects as small as 3mm, but ground based radars cannot reliably track objects of this size [48]. Without reliable track information, operational spacecraft cannot maneuver to avoid these mid-sized particles, and they are too large to be effectively shielded against. Over 10 million particles smaller than 1 cm in diameter are estimated to exist in Earth orbit, based on observational data from the external surfaces of recovered spacecraft. These objects cannot be detected or tracked by modern means, so spacecraft typically require shielding on some external surfaces to mitigate the risk of damage from collisions with them [48].

Figure 40, Figure 41, and Figure 42 display an instantaneous "snap-shot" of all of the tracked objects in near-Earth orbits. While a small number of these objects are operational satellites, over 95 % of them are orbital debris. In all three images, the white "dots" represent the approximate instantaneous location of each tracked item, but they are not scaled to represent their actual size in comparison to each other or the Earth. The particular range and perspective of each picture was selected to adequately capture the orbit in question.
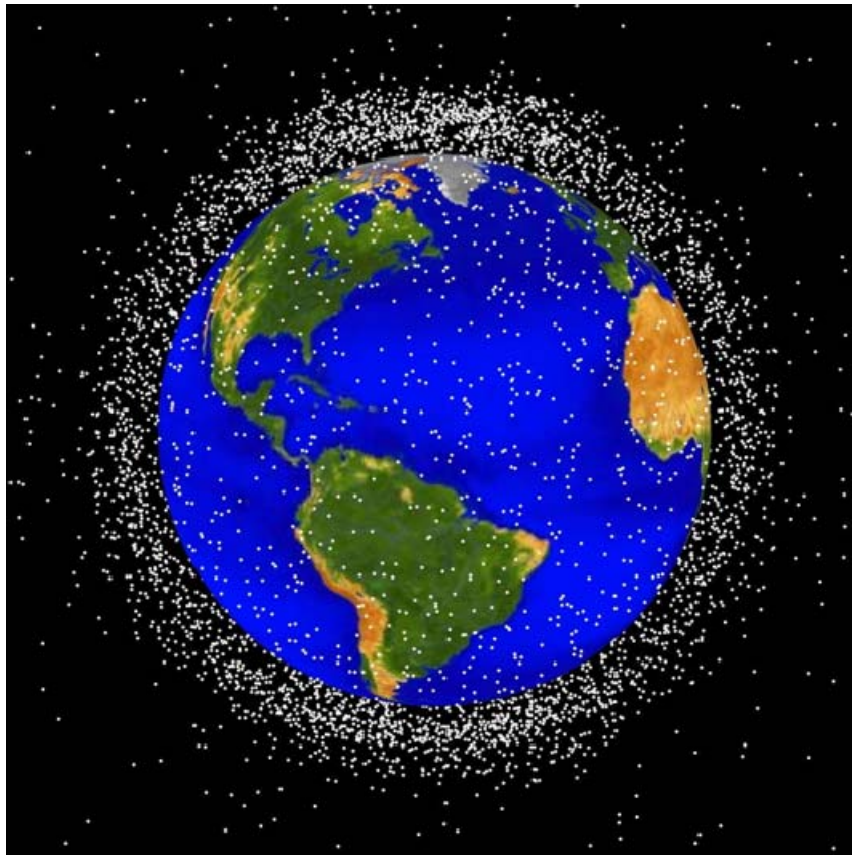
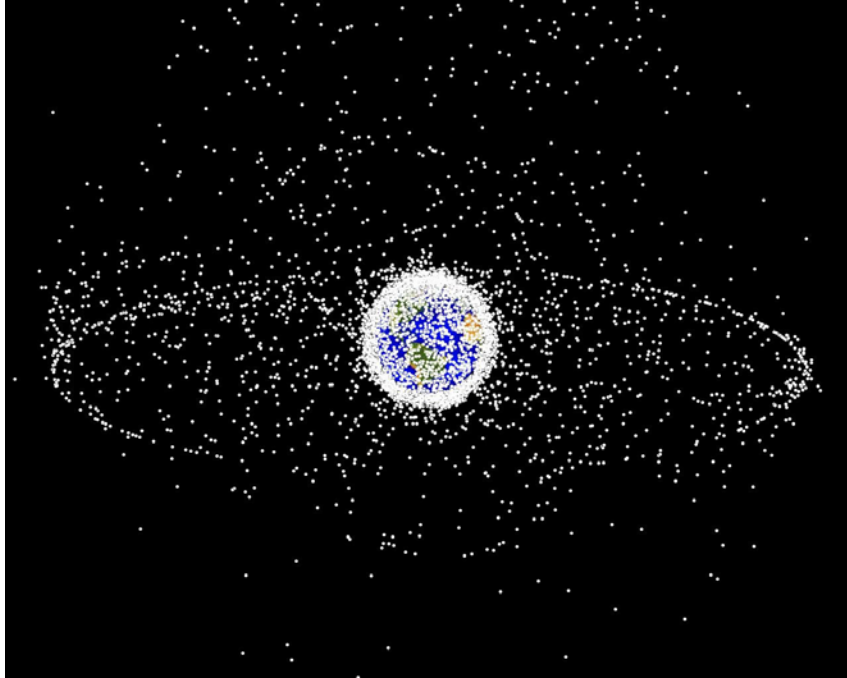Figure 40.   Objects in LEO. From [48]
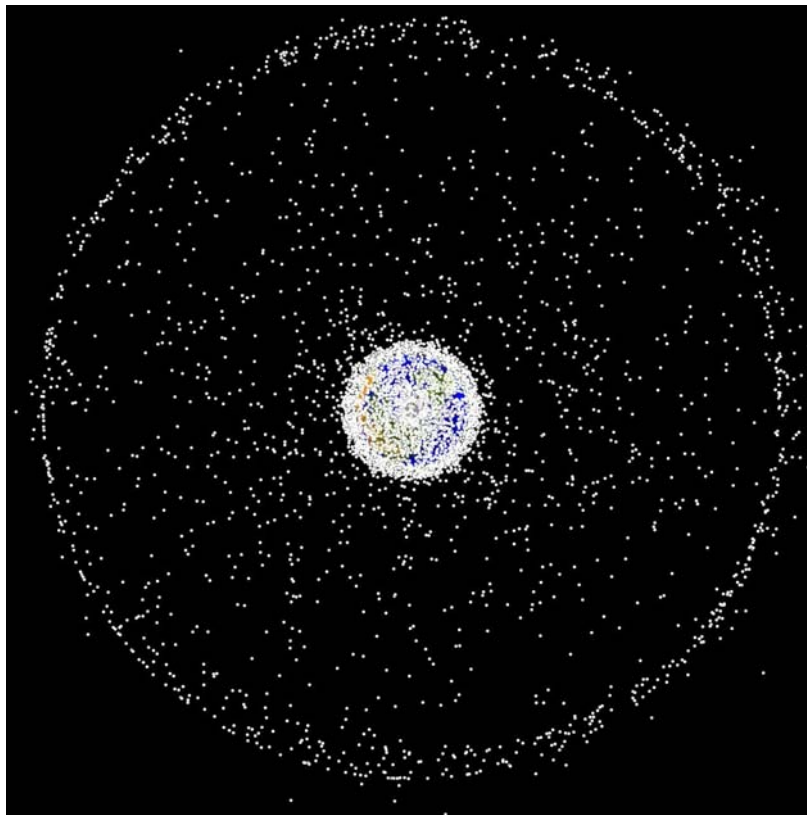
Figure 41.   Objects in GEO and LEO. From [48]

Figure 42.   Polar View of GEO and LEO Objects. From [48]

B. PROBLEM SCOPE

There are four primary types of orbital debris—Non-Functional Spacecraft, Rocket Bodies, Mission Related Debris, and Fragmentation Debris. Only one-fifth of the spacecraft in orbit are functional spacecraft [49, p. 21]. When a GEO spacecraft reaches its EOL, it is usually moved to a higher or lower disposal orbit, but LEO satellites have traditionally been left in their orbits until they naturally decay. In both cases, these satellites are classified as non-functional spacecraft. Rocket bodies represent the one or more stages of a launch vehicle that are jettisoned as they deliver a satellite to its functional orbit. Usually only one rocket body is left in orbit for LEO missions, but GEO missions may release up to three separate rocket bodies in different staging orbits along the way. The presence of rocket bodies in orbit is of particular importance due to their typically large dimensions and the explosive potential of their residual propellants. These bodies generate much of the fragmentation debris in LEO. Figure 43 is a picture of a Delta 2 second-stage, main-propellant tank that landed in Georgetown, Texas, in 1997. This tank has a mass of over 250 kg and survived reentry relatively intact [49].

Figure 43.   Delta 2 Second-Stage Main Propellant Tank After Reentry. From [48]

Mission-related debris is usually released in the course of a satellite's deployment, activation, and operation, such as explosive bolts, spring release mechanisms, spin-up devices, or solid rocket slag. The amount of debris released by a typical spacecraft can be quite large, with one study observing the generation of 76 separate objects from a single Russian launch mission [49, p. 24]. In Figure 44, a pellet of aluminum oxide (Al_2O_3) solid rocket motor slag, some of the most common mission-related debris, is displayed. Solid rocket motors are commonly used for orbital transfer operations, but the relative abundance of their effluent slag has only recently been discovered and studied. During the burn process, large numbers of aluminum oxide particles are formed and ejected, but the number of particles ejected and their respective sizes are not well known. NASA's Project ORION report stated that these particles are generally assumed to be less than 10 μm in diameter, but over one thousand can be generated in a single firing [48]. The particle shown in Figure 44 represents a larger and presumably less common particle generated during ground testing, shown for illustrative purposes.
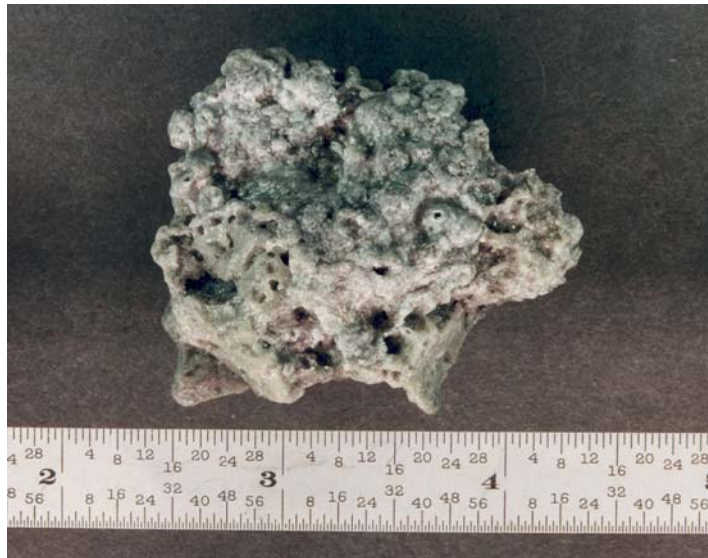

Figure 44.   Aluminum Oxide Solid Rocket Motor Slag. From [48]

Fragmentation debris consists of space objects created during collisions between other objects, explosive events, or space weapons testing. Due to the variation in ejection trajectories and velocities, a cloud of debris emanating from a fragmentation event evolves over time to spread throughout nearby orbits, resulting in a broad band of

material. Figure 45 displays the three phases of evolution for a cloud of orbital debris after a fragmentation event. In phase one, an ellipsoidal cloud of debris is formed that follows the general orbit of the parent body. In phase two, the velocity and trajectory variation of the debris accumulates to spread the ellipsoidal cloud into a torus near the original orbit. In phase three, the debris cloud continues to evolve into a wide band.
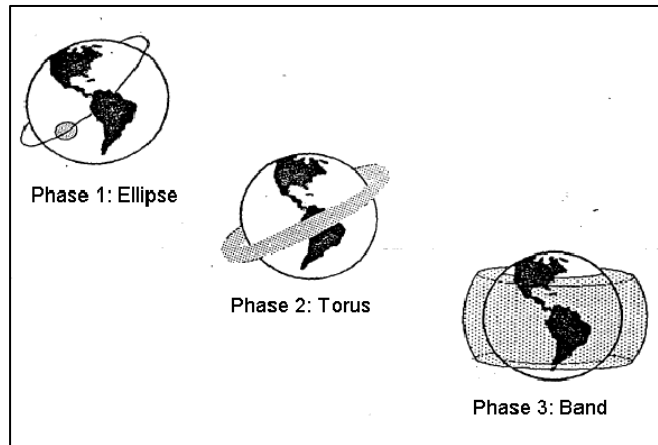

Figure 45.   Debris Cloud Evolution. From [50]

Another serious source of fragmentation debris is the flaking of spacecraft paint under solar radiation and particle impacts. This problem was first seriously considered in 1983, when STS-7 Space Shuttle returned to Earth with a millimeter sized crater in an orbiter window. Figure 46 is a picture of this impact damage. This picture is an example of the risks posed by orbital debris to both manned and unmade space missions.
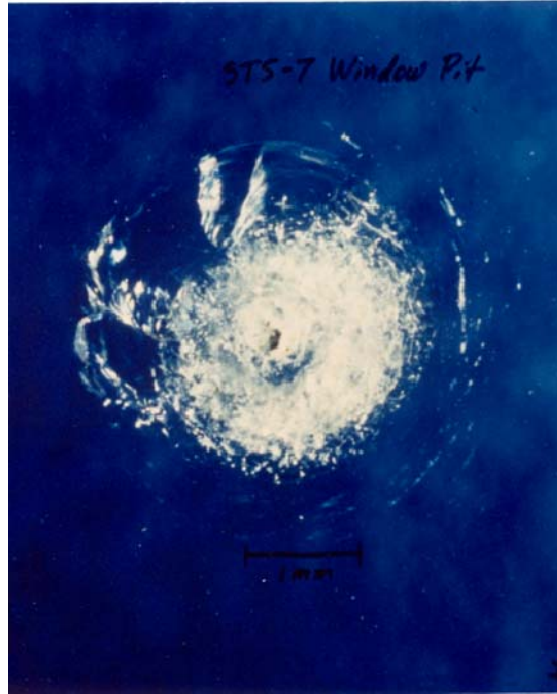
Figure 46.   STS-7 Orbital Window Impact Crater due to a Paint Fleck.
From [48]

Ever since the launch of Sputnik in October 1957, the near-Earth environment has continued to accumulate orbital debris. The largest contributor to the daily growth of debris is the frequent fragmentation of larger objects through collision or explosive events. Figure 47 displays the monthly breakdown of objects in Earth orbit by object type. With an international average near 75 launches each year, the number of spacecraft, rocket bodies, and mission related debris continues to grow, but the relative abundance of fragmentation debris continues to rise dramatically as collisions and explosions occur on-orbit. The largest fragmentation events in recent history were due to the Chinese Fengyun-1C (FY-1C) anti-satellite test in January 2007 and the collision between Iridium 33 and the derelict Cosmos 2251 in February 2009. These events created over 5000 fragmentation objects > 10 cm in diameter and nearly doubled the population of cataloged orbital debris [51, p. 7].
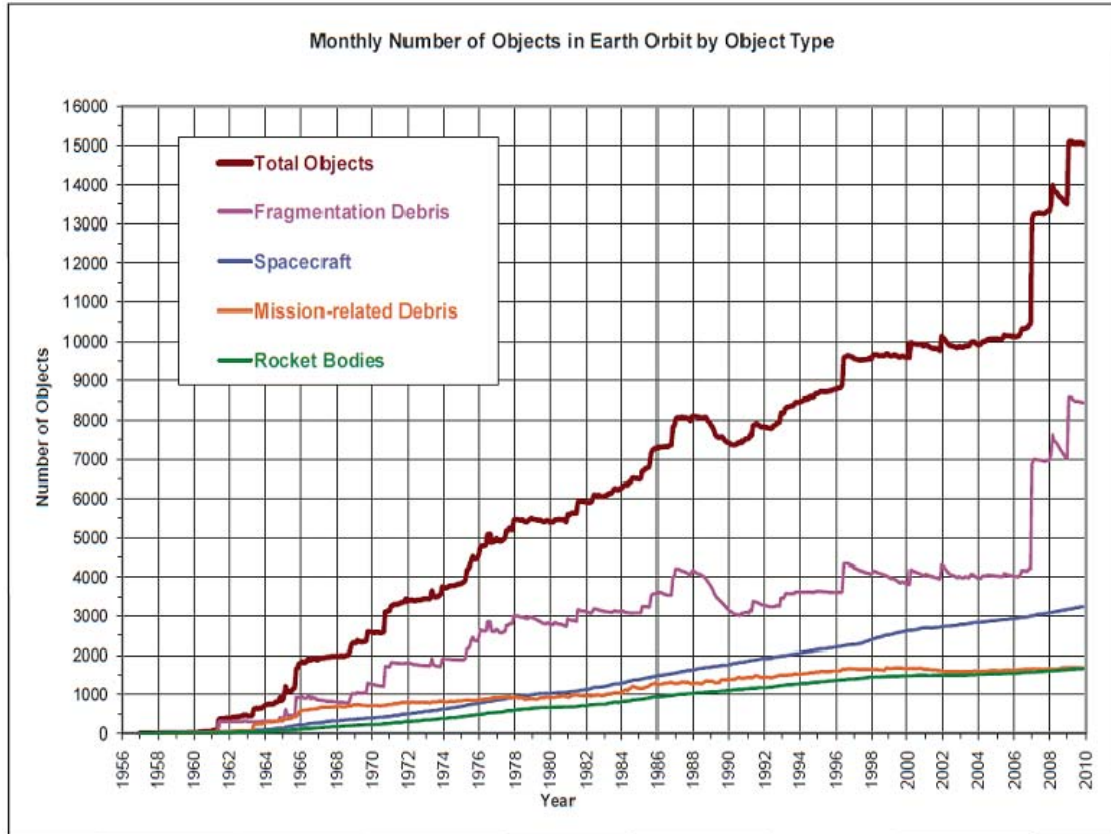
Figure 47.   Orbital Debris Breakdown. From [51, p. 12]

Considering the alarming rate of orbital debris generation, the era of mankind's open and relatively simple access to space may be coming to an end. Any increase of fragmentation events, such as through a future war with anti-satellite engagements or simply from the continued collisions in crowded orbits, has the potential to render those orbits virtually useless for generations to come. If the Chinese ASAT engagement above generated ~3,000 pieces of debris, an anti-satellite war that destroys only 10 satellites could immediately double the current debris population, and this large debris field would spread over time to other orbits "near" the parent satellite.

Currently, there are no programs for the removal of space debris from orbit, and the National Aeronautics and Space Administration (NASA) has only recently enacted guidelines to limit the creation of orbital debris. Likewise, the space debris problem will not "solve itself" in the near future. The anticipated orbital lifetime of debris in the 800-1100 km range is on the order of 10,000 years [52, p. 576]. The space tug concept

discussed in Chapter V may be one method to reduce the amount of large debris, such as rocket bodies and non-functional spacecraft, by hauling these items into lower disposal orbits that experience higher atmospheric drag. Similarly, by reducing the larger parent objects, much of the future fragmentation debris growth could be avoided. For smaller debris, the most-promising, near-term method of debris removal is through the illumination of debris clouds with a high energy laser to lower the perigee of their orbits as proposed by Project Orion.

C.   TARGET PROPERTIES

During the 1990s, NASA investigated the design of an orbital debris removal system using a ground-based laser. This study was referred to as Project Orion, and it primarily considered the laser useful for the removal of orbital debris with diameters between 1 and 10 cm. Objects less than 1 cm are extremely numerous, but they are difficult to detect. Therefore, shielding against them is common practice for all satellites. Objects larger than 10 cm are routinely tracked, but their numbers remain small enough that operational spacecraft can maneuver to avoid them [53].

Project Orion focused on five major types of mid-size debris that are most numerous in the orbits of concern. These debris types are: Na/K spheroids released from a leaking Russian nuclear power plant, carbon phenolic fragments, multilayered insulation (MLI), crumpled aluminum, and steel tank rib supports. Table 6 displays the typical characteristics of these debris particles and their standard orbits. The left-most column lists a description of important orbital and physical characteristics for each type of debris. The inclination, apogee, perigee of each debris type are generalizations based on radar measurements of the orbit or the orbital parameters of the parent object. The approximate sizes and abundance of each debris type are based on radar or optical measurements or, in some cases, theoretical modeling. The bond albedo and optimum *Cn* are numbers that reflect the coupling and interaction between the laser beam and the object. The Δv is a calculated number based on the mass and orbit of the objects. Due to the age of this report, the estimated number of targets is no longer accurate, but the general categories and orbits remain the same. As a general approximation of these

debris categories and the aluminum-oxide, solid-rocket-motor slag that has recently alarmed scientists, the calculations in this chapter will assume that the target is an aluminum sphere with a diameter of 5 cm.

Debris Target Matrix

Target	A	B	C	D	E
Description	Na/K Sphere	Carbon Phenolic Fragment	MLI (Plastic/Al Surfaces)	Crumpled Aluminum	Steel Tank Rib Support
Inclination (deg)	65	87	99	30	82
Apogee (km) Perigee (km)	930 870	1190 610	1020 725	800 520	1500 820
A/m (cm²/gm) Actual size (cm)	1.75 1.0	0.7 1×5	25 0.05×30	0.37 1×5	0.15 1×10
Bond albedo	0.4	0.02	0.05/0.7	0.05/0.7	0.5
Optimum C_m(dyne–s/J)	6±2	7.5±2	5.5±2	4±1.5	4±1.5
Δv required (m/s)	190	110	140	90	160
Estimated number of targets	50 k	20 k	60 k	10 k	10 k

Table 6.   Debris Target Matrix. From [53]

D.   ATMOSPHERIC DRAG

Even without human intervention, solar activity indirectly influences the orbital debris environment by heating the Earth's upper atmosphere, which affects the upper atmospheric density and, therefore, the atmospheric drag experienced by objects in LEO. During the eleven-year solar cycle, fluctuations in solar intensity lead to a slow pulsation of Earth's atmosphere that can accelerate the orbital decay of objects in LEO when the atmospheric density increases at higher altitudes. Likewise, atmospheric drag has a greater effect when the orbit is at perigee, so the eccentricity of orbits tends to circularize over time at the same altitude as its perigee, resulting in an overall lower average altitude for the orbit. At lower altitudes, the object experiences greater atmospheric drag, leading

to further orbital decay. Therefore, any method which increases the atmospheric drag on an orbital debris cloud would help to decrease its orbital lifetime.

NASA's Project Orion sought to utilize a high-peak-power, ground-based laser to ablate small portions of the debris material in order to provide a change in velocity, or Δv, that would lower the altitude of the orbit. As their moniker suggests, high-peak-power lasers have a very high energy per pulse, which is sufficient to cause ablation, but their pulses are less frequent than an FEL's pulses. This single, high-energy pulse is what allows for the ablation of material and subsequent Δv.

If an FEL were utilized for orbital debris removal, it would not have enough peak-power to ablate the surface material of the debris. In contrast to other types of laser, an FEL achieves its high average power by generating frequent pulses with comparatively small amounts of energy per pulse. While NASA's proposed laser for Project Orion generates 150 J per pulse, a 1 MW FEL will only produce about 10 mJ per pulse, but at $\sim 10^6$ times the pulse repetition frequency [53].

An FEL may be able to induce a faster than normal orbital decay by removing some of the debris material through vaporization. If enough power can be delivered in one orbital pass to heat some of the object enough to undergo two phase changes, from solid-to-liquid and then from liquid-to-gas, the remaining particle will have a smaller diameter and less mass than the original. As shown by Equation (IV.8), the deceleration due to atmospheric drag is proportional to the object's surface area and inversely proportional to its mass. A less massive particle with a lower surface area may not experience more atmospheric drag. However, particles greater than 1 cm in size are still hazardous to spacecraft. Therefore, the calculations included here will determine the amount of energy required to melt and vaporize enough material such that the remaining particle is less than 1 cm.

E.   CALCULATIONS

1.   Assumptions

As in Chapters V and VII, this chapter will make a general assumption that atmospheric transmission for the FEL operating at 1 μm is ~50%, so only half of the laser power is transmitted outside the atmosphere. These calculations will ignore turbulence and thermal blooming effects. Due to the small target size and pointing accuracies required, these effects require further study. This thesis will assume that accurate tracking and pointing mechanisms exist to maintain the laser beam on the targets in question. Improved tracking due to brighter illumination may be a significant advantage of the MW-class FEL.

The calculations of this chapter approximate the target orbital debris as a homogeneous sphere of aluminum with a radius of 2.5 cm. This is a considerable oversimplification of the actual composition of most orbital debris, but aluminum is a fairly common material in the debris population. It is frequently utilized during spacecraft construction, and the aluminum oxide slag produced by solid rocket motors is a growing contributor to the total debris population. In terms of examining the difficulty of debris removal, the density, thermal conductivity, and relatively high melting and boiling temperatures of a metal present a challenging target for laser removal. A debris particle consisting of insulating material may be deflected by evaporation because they do not conduct heat well and the material would leave the object's surface asymmetrically.

2.   STK Simulations

In order to determine whether a high power FEL could conceivably vaporize orbital debris, this chapter begins with a Satellite Tool Kit (STK) simulation to determine the approximate access times between a hypothetical, high-altitude, ground-based laser and two of the prominent debris categories shown in Table 6. In this simulation, the altitude of the ground site does not affect the power transmitted through the atmosphere, but it does affect the line-of-sight to the satellite. Due to their aluminum content, relative

abundance, and differing orbital parameters, the materials modeled in STK were the MLI and the crumpled aluminum. Figure 48 displays a two-dimensional STK plot of the laser ground station and satellite ground tracks. The laser ground station is visible on the left, in the Hawaiian Islands. The high inclination orbit of the MLI debris is shown, and the MLI appears to the upper left of the figure. The mid-inclination orbit of the crumpled aluminum debris is shown near the equator, and the debris appears to the center-right of the figure. The accesses between laser and satellite tracks are shown in dark black over the satellites' ground tracks. For this simulation, the lasers' illuminations were restricted to times when the satellite was in sunlight and at least 10 degrees above the horizon.
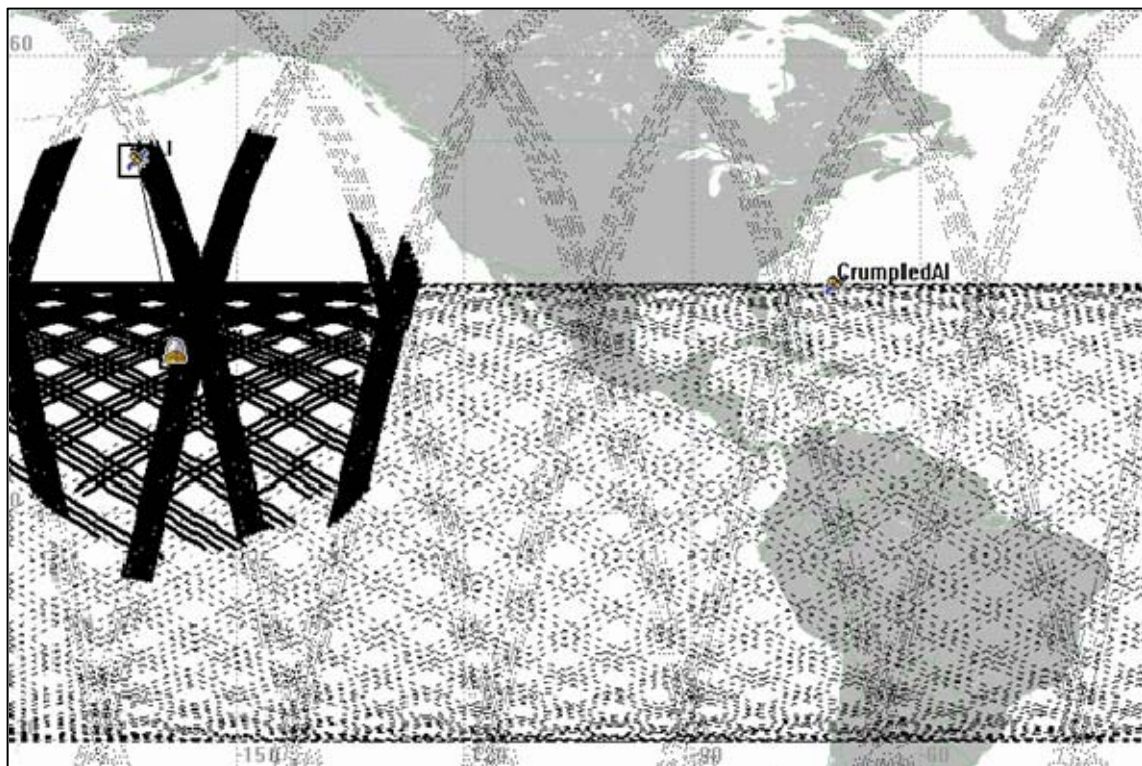

Figure 48.   STK Plot of MLI and Crumpled Aluminum Debris Orbits with Laser Ground Station and Accesses

Figure 49 is a summary of an STK access report for the laser ground station and the debris particles. In both cases, the mean duration of all accesses was over 700 sec. Therefore, the phase change calculations presented below can only be successful if the total time required is less than 700 sec.

```
Facility-Hawaii-To-Satellite-CrumpledAl:  Access Summary Report


Global Statistics
-----------------
Min Duration          32    5 Jul 2007 13:44:21.893    5 Jul 2007 13:45:50.135              88.242
Max Duration           6    2 Jul 2007 01:32:35.840    2 Jul 2007 01:48:05.964             930.124
Mean Duration                                                                              705.971
Total Duration                                                                           38122.413


Facility-Hawaii-To-Satellite-MLI:  Access Summary Report


Global Statistics
-----------------
Min Duration          19    4 Jul 2007 13:31:16.736    4 Jul 2007 13:32:46.909              90.174
Max Duration          11    3 Jul 2007 03:51:34.143    3 Jul 2007 04:09:02.743            1048.601
Mean Duration                                                                              709.407
Total Duration                                                                           27666.862
```

Figure 49.   Summary of an STK Access Report for MLI and Crumpled Aluminum
Debris With One Ground Station

3.   Calculations

The calculations that follow attempt to evaluate the thermal properties of a debris particle as it is heated in daylight by solar and laser illumination. The initial temperature of the debris was estimated using a Microsoft Excel spreadsheet, and these calculations are displayed in Appendix C. All of the other calculations were performed in the MATLAB program, and the program used is also included in Appendix C.

In the MATLAB code, a heat balance equation is established with inputs from solar and laser illumination and heat losses due to the radiation of thermal energy. The heat inputs due to the solar albedo and Earth's IR radiation are not evaluated. As a first approximation, this model did not account for the change in propagation range as the debris particle passes from horizon-to-horizon or for the change in radius of the debris particle as material is ejected. The laser intensity is calculated at a range of 700 km and held constant throughout the illumination time. If the concept does not succeed without accounting for the losses discussed above, then it surely will not succeed when they are completely modeled.

Figure 50 displays the thermal profile of a debris particle when illuminated by a 1 MW FEL with a beam radius at the target of 1.16 m. This laser uses similar parameters to the ship-borne FEL discussed in Chapter V, and the beam spot size at the target is entirely caused by the natural diffraction of the beam. As shown below, the intensities produced by this laser cannot even heat the debris particle to its melting temperature during one orbital pass.
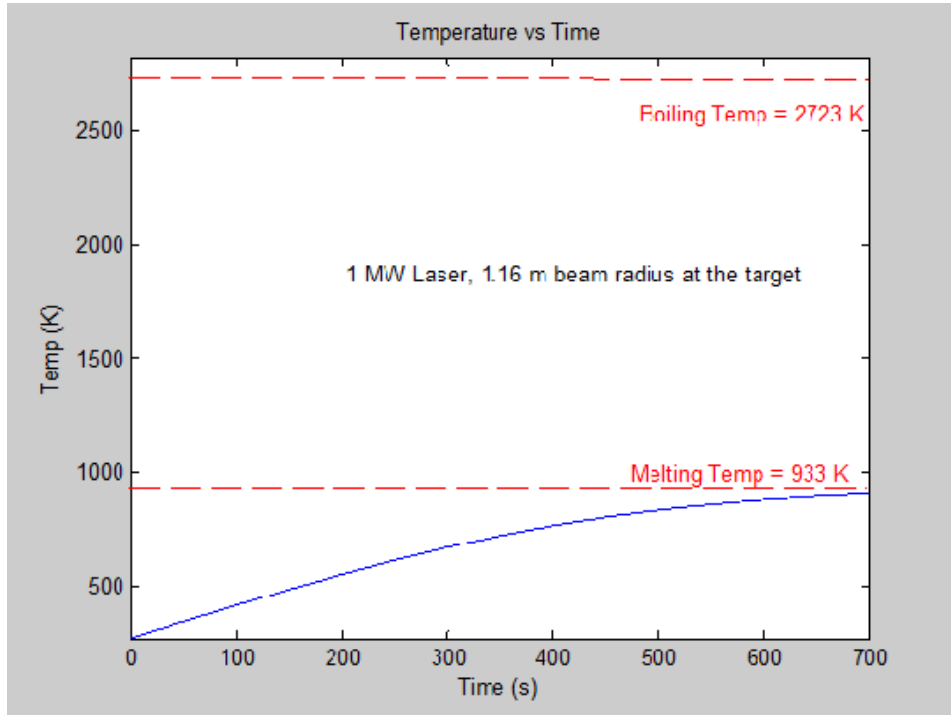

Figure 50. Debris Temperature Profile with a 1 MW Laser and a Beam Radius of 1.16 m at the Target

Figure 51 displays the thermal profile of a debris particle that is illuminated by a 1 MW FEL with a beam radius at the target of 0.25 m. This spot size could hypothetically be achieved using a spherical mirror that is at least 0.9 m in radius, i.e., this mirror could be a spherical version of the ship-borne mirror discussed above. By concentrating the beam to such a small area within the atmosphere, thermal blooming would have an even more critical effect on the beam propagation, but this simulation was intended to bound

the usefulness of a 1 MW laser. Even with this added intensity, the 1 MW laser still only heats the debris particle to about 2000 K before the heat input is matched by the radiated heat.
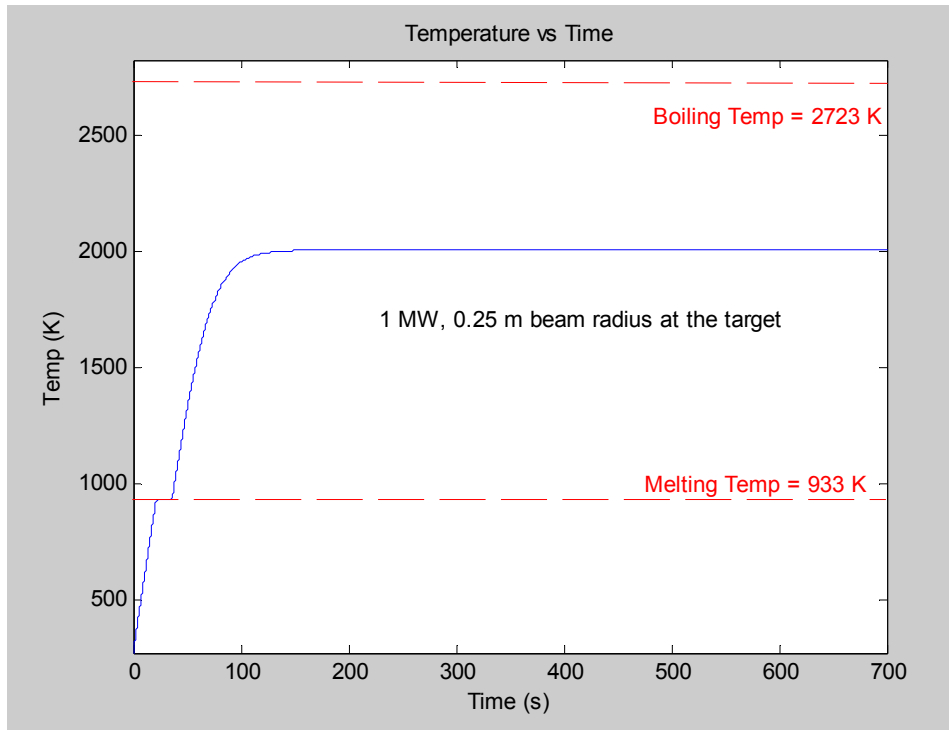

Figure 51.   Debris Temperature Profile with a 1 MW Laser and a Beam Radius of 0.25 m at the Target

Figure 52 displays the temperature profile of a debris particle being heated by a 10 MW FEL with a beam radius at the target of 0.4 m. Unlike the cases presented above, this laser does successfully heat the debris particle to its melting temperature and vaporize some, but not all, of the material that we hoped to remove. However, assuming the actual construction of a laser of this size, the successful atmospheric propagation of a laser beam with this cross-sectional area and power are questionable at best.
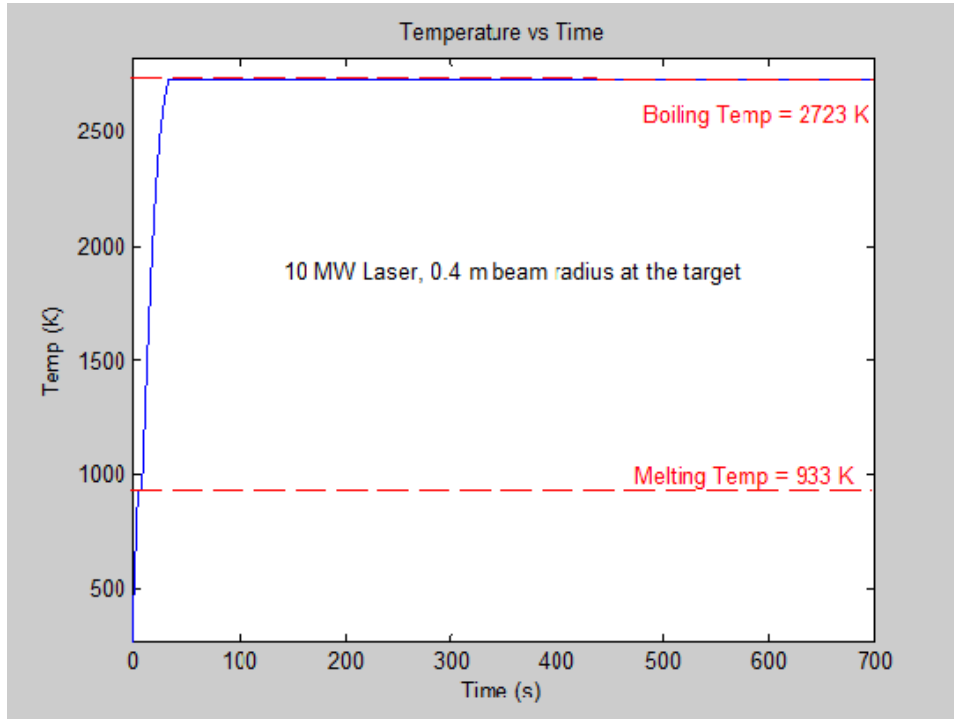
Figure 52.   Debris Temperature Profile with a 10 MW Laser and a Beam Radius of 0.4 m at the Target

4.   Discussion

The simulations conducted above utilized many favorable approximations and ignored some potential loss mechanisms in the illumination of a debris particle by an FEL. Even without these additional losses in laser intensity at the target, the figures above suggest that heating large quantities of orbiting material to induce vaporization is not feasible for a ground-based FEL. The removal of orbital debris using a laser is probably best accomplished by the ablation method described by Project Orion. However, a ground-based FEL might be able to assist in detecting small, non-metallic orbital debris through illumination and optical tracking.

VII.   ILLUMINATING EXTRATERRESTRIAL BODIES

Chapters V and VI investigated the near-term engineering applications of power beaming and orbital debris removal for a ground-based, next-generation FEL. Chapter VII will discuss the application of a similar FEL to illuminate the Lunar or Martian surfaces for scientific study. It will also discuss the development of a larger, futuristic FEL for interstellar communication. Due to the high spectral density of an FEL and the collimation of the laser beam, it is found to be possible to match or exceed the Sun's irradiance within a limited bandwidth over ranges extending out to the Martian orbit. Similarly, the distances involved in interstellar communications require a strongly collimated beam with good coherence and propagation properties. With the ability to run indefinitely at high-average powers, an FEL is an optimal laser to generate a repeating and distinctly intelligent signal for transmission to the growing number of detectable, "near-by" extra-solar planets that may have the ability to support life.

A.   ASSUMPTIONS

As in Chapters V and VI, this chapter will make a general assumption that atmospheric transmission for the FEL operating at 1 μm is 50%, so all of the laser powers are halved outside the atmosphere. These calculations will ignore turbulence and thermal blooming effects, but due to the length of propagation outside of the atmosphere, their effects may seriously affect the outcome of these applications. Likewise, some of the applications within this chapter assume the utilization of considerably larger lasers with powers that may not be feasible in the near future. Due to the futuristic nature of some of these applications, it may be possible that the laser could be constructed on the lunar surface to avoid these atmospheric losses or that some other unforeseen method of avoiding most atmospheric losses has been devised. A larger mirror that is already being considered for space exploration will use adaptive optics that can significantly reduce both thermal blooming and turbulence effects.

As in previous sections, this thesis will assume that accurate tracking and pointing mechanisms exist to maintain the laser beam on the targets in question. As a reference

for the interstellar applications in Section D, we can calculate the angular diameter of a planet-moon orbit similar to our own at interstellar ranges. The Moon orbits the Earth at approximately 3.8 x 10^8 m, and the range of the probable minimum distance to intelligent life is about 10 light years or 10^{17} m. At this range, the angular radius of the Moon's orbit would be about 0.00078 arc-seconds, approximately an order of magnitude smaller than the 0.0072 arc-seconds angular resolution capability of the Hubble Space Telescope [41]. For comparison, the W. M. Keck Observatory's Keck I telescope routinely achieves a pointing accuracy of 10 arc-seconds in azimuth [54].

For calculations regarding planetary distances and extrasolar distances, the distance between Earth and the other planets was based on a comparison of the semi-major axis of their orbits. This is a simplified model as the eccentricities and inclinations of the orbits lead to large variations in the interplanetary distances, however, it is assumed here that any illumination would be planned for optimal times when the orbital distance is small to aid the lasers propagation characteristics.

B.   SOLAR INTENSITY

Using the Planck's blackbody approximation given in Equation (V.2), the solar output within a limited bandwidth can be calculated. An FEL has a bandwidth of about 0.1 % of its wavelength, or 1 nm for an FEL operating at 1 μm, and the Sun emits only about 0.07 % of its total output in this band. Starting at the surface of the Sun, which is assumed here to be roughly 6.96 x 10^6m from the Sun's center, this power output can be translated into intensity for any desired radius. While the solar energy spreads over a uniform sphere, a laser beam would initially remain much more collimated, until diffraction effects began to grow. Therefore, it may be possible for a high power laser to match or exceed the solar intensity within its bandwidth over some ranges. Figure 53 displays the solar output as a function of wavelength when the sun is approximated as a blackbody with a temperature of 5800K. In Figure 53, the laser bandwidth is represented in red to show the relatively small portion of the spectrum that it occupies.
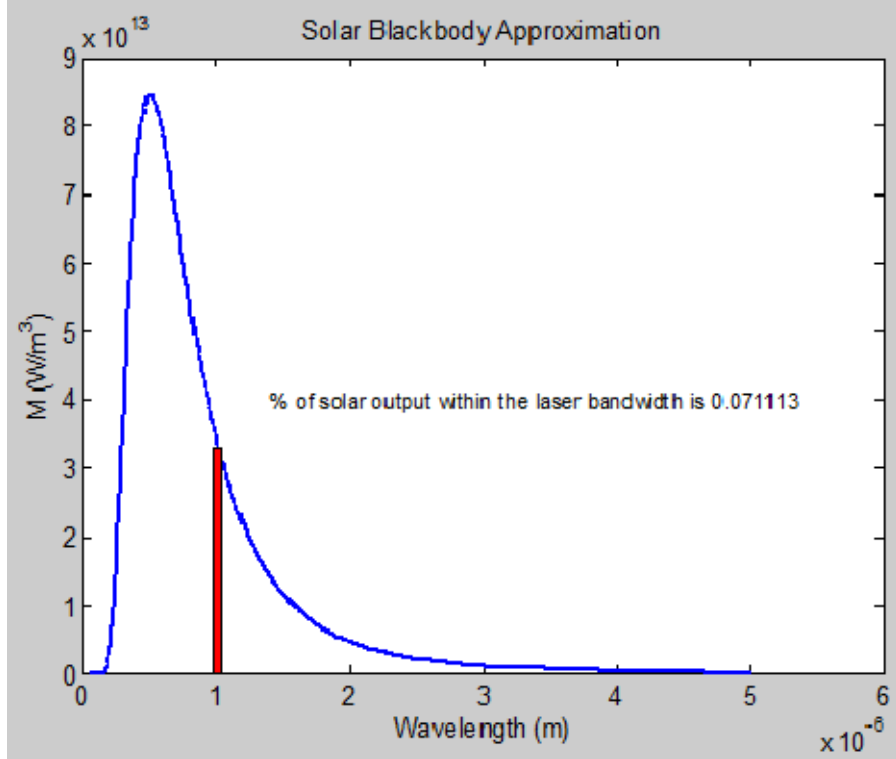
Figure 53.   Percentage of Solar Output within the Laser Bandwidth

C.   CALCULATION SETUP

The calculations of laser beam radius (w), area (A_s), and intensity (I) at the target are based on Equations (III.1) through (III.6) and the assumptions stated above. These equations are restated here for easy reference. The laser beam radius (w) is given in terms of the distance (z), beam waist (w_o), and wavelength (λ) by

$$w(z) = w_o \sqrt{\left[1 + \left(\frac{\lambda z}{\pi w_o^2}\right)^2\right]},$$ (VII.1)

and the laser beam's intensity (I) is

$$I = \frac{P}{A_s}, \text{ where}$$ (VII.2)

$$A_s = \pi w^2.$$ (VII.3)

115

D.   ILLUMINATING BODIES WITHIN THE SOLAR SYSTEM

Section D will investigate the use of two notional FELs for the illumination of extra-terrestrial bodies within the Solar System. These FELs include the next-generation, ship-borne, MW-class laser that was discussed earlier and a large and futuristic laser with parameters beyond currently achievable technology. Due to the relatively high spectral intensity of these lasers, the illumination provided by them could match or exceed the spectral intensity of the sun inside the laser's bandwidth. Using a specialized signal, the laser might even be detectable through a cross-correlation function at levels well below the solar, background noise. The FEL is continuously tunable so that a wide range of wavelengths could be used for scientific exploration or the detection of asteroids or meteoroids.

Two cases will be considered here, and both of them will be assumed to operate at a wavelength of 1 μm with a bandwidth of 0.1 % of the wavelength. The first utilizes the ship-borne, MW-class FEL discussed earlier that is likely to be deployed within the next twenty years. This laser is referred to here as Laser 1, and it produces ~1 MW of average power using a director mirror of about 1 m in radius. The second utilizes a similar, but ground-based, FEL, referred to here as Laser 2, with a larger director mirror that is equivalent to current optical tracking mirrors. This laser operates an average power of ~1 MW, but its director mirror is about 10 m in radius. Although development of this laser would combine state of the art technology for most of the components, it could realistically be built in the next twenty to thirty years assuming aggressive funding.

1.   Illuminating the Moon

For these calculations, an average lunar range of 3.84×10^8 m was assumed. Figure 54 and Figure 55 display the laser beams' respective radii at the lunar surface. Laser 1 has a radius of approximately 120 m, which could be used to illuminate specific topographical features of interest such as an impact crater, mountain, or canyon. Laser 2 has a radius of approximately 16 m, which could be used for more detailed study of lunar topography or for power beaming to a lunar base.
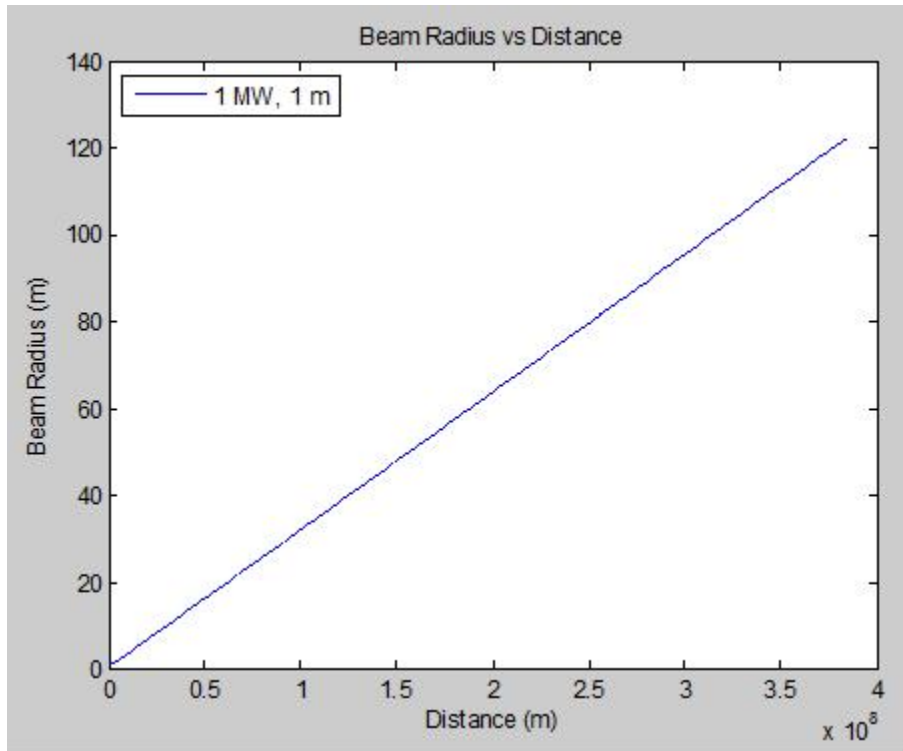
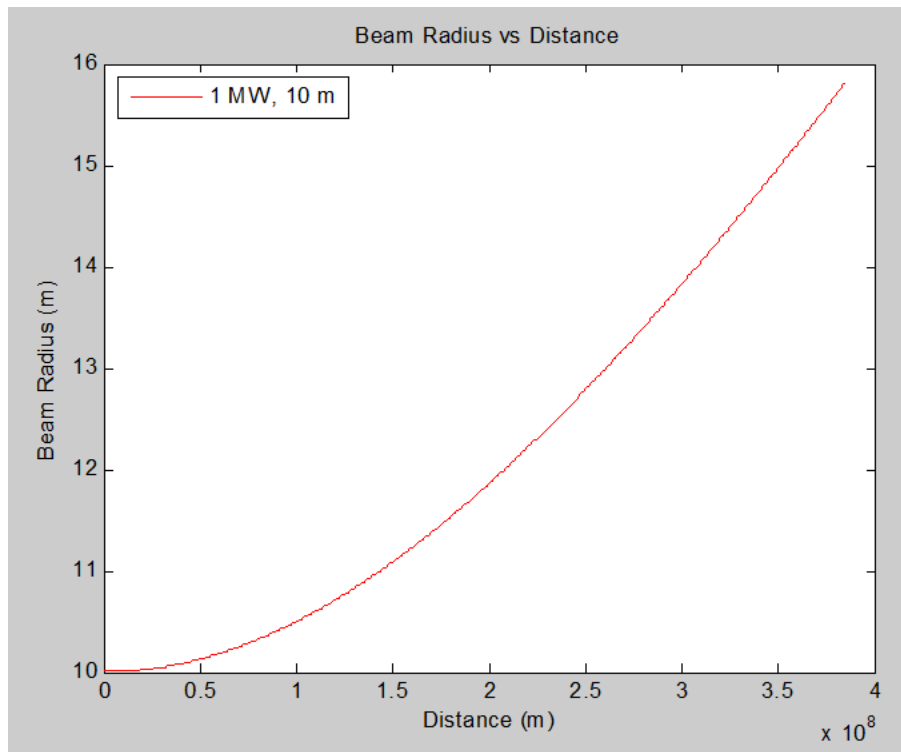Figure 54.   Laser 1 Beam Radius at the Moon

Figure 55.   Laser 2 Beam Radius at the Moon

Figure 56 and Figure 57 display the laser intensities over ranges extending from Earth to the lunar surface. At this long range, neither laser exceeds the total AM0 solar intensity of 1366 W/m^2, however, the spectral intensity of the sun is only about 96 W/m^2 within the lasers' bandwidth, which is less than an order of magnitude greater than Laser 1 and six times less than Laser 2.
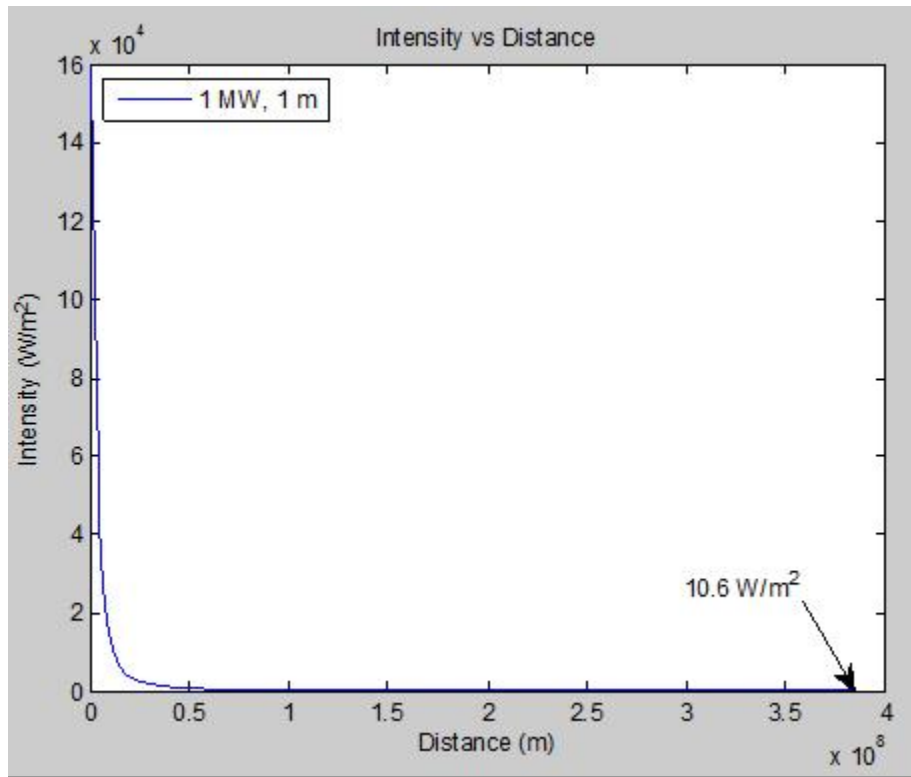

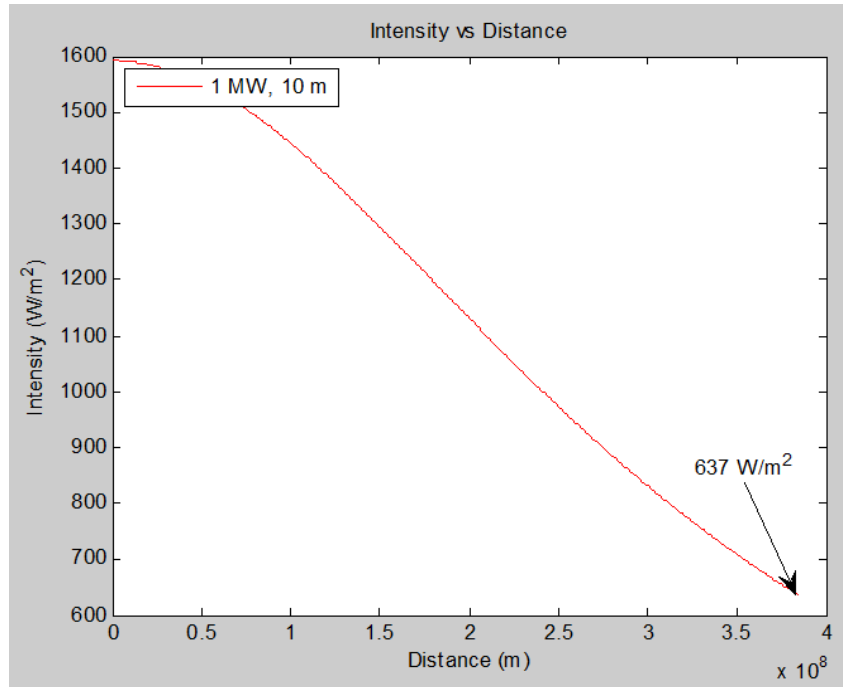Figure 56.   Laser 1 Intensity at the Moon

Figure 57.   Laser 2 Intensity at the Moon

In both examples, the advantages of laser illumination such as the pulse structure of an FEL and the ability to code the signal allows for radar-like imaging of the lunar surface. Likewise, in power beaming applications, the additional efficiency of solar cells under monochromatic illumination allows for the generation of equivalent electrical energy if the laser's intensity is roughly half of the AM0 solar intensity, like the 637 W/m^2 provided by Laser 2. Without considering atmospheric turbulence or thermal blooming, diffraction effects alone do not rule out the successful utilization of a laser like Laser 1 for scientific study of the lunar surface if a cross-correlation filter is used to process the return signal. Likewise, the futuristic Laser 2 produces sufficient intensity on the lunar surface to be an excellent candidate for beaming power to a lunar base, topographical mapping, or scientific illumination in the search of specific elements.

2.   Illuminating Mars

Following favorable results in lunar illumination applications, this section will seek to evaluate the utility of an FEL for illumination of objects as far as the Martian orbit. For this purpose, the Earth-Mars distance is approximated by the difference in the

119

semi-major axis of each orbit, about 78.3 million km, acknowledging that the Earth-Mars distance varies widely. It is assumed that these illuminations would be planned for times when the propagation distance is the smallest. In recent history, the range of closest approach between Earth and Mars has varied from the 55 million km approach in 2003 to the 101 million km approach in 1995 [55].

Figure 58 and Figure 59 display the laser beam radius for Lasers 1 and 2 at Mars. At these ranges, the approximate radii of Laser 1 and 2 are 80 km and 8 km respectively. These beam sizes are large, but they are probably still useful for the illumination of large topographic features or specific regions, such as a potential landing zone for a spacecraft.
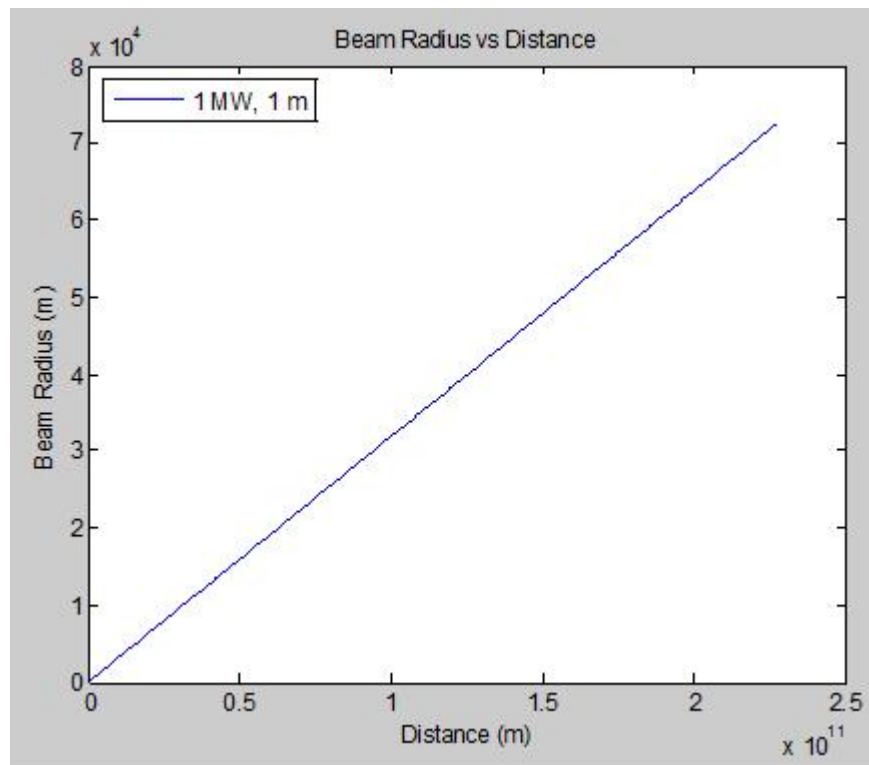

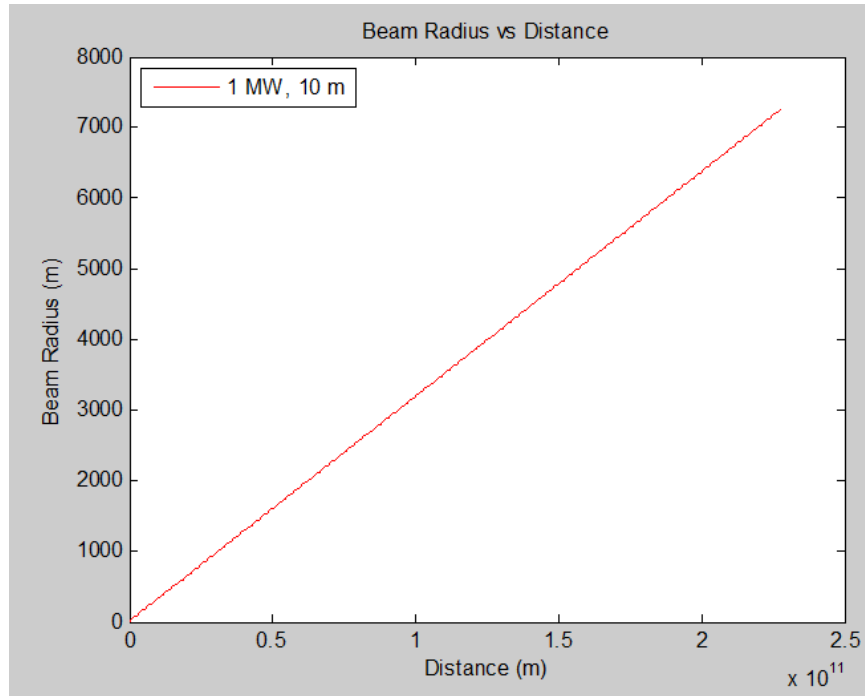Figure 58.   Laser 1 Beam Radius at Mars

Figure 59.　　　Laser 2 Beam Radius at Mars

Figure 60 displays a comparison of the laser and total solar intensities at the Martian surface. As is clearly shown, even high power lasers can only compete with the solar spectral intensity over a relatively limited range near the Earth. At longer ranges, the total solar intensity exceeds Laser 1 by about 3 orders of magnitude and Laser 2 by about one order of magnitude. As discussed in Chapter II, the pulse structure of a MW-class FEL produces a peak intensity that is about 1000 times greater than the average intensity, therefore, Laser 1 might match, and Laser 2 could exceed, the total solar intensity during the macro-pulse timescale. Also, in a process common to radar and lidar applications, the transmitted laser pulse could contain a specific signal pattern that would greatly improve the detector's signal to noise ratio (SNR) after passing through a cross-correlation filter.
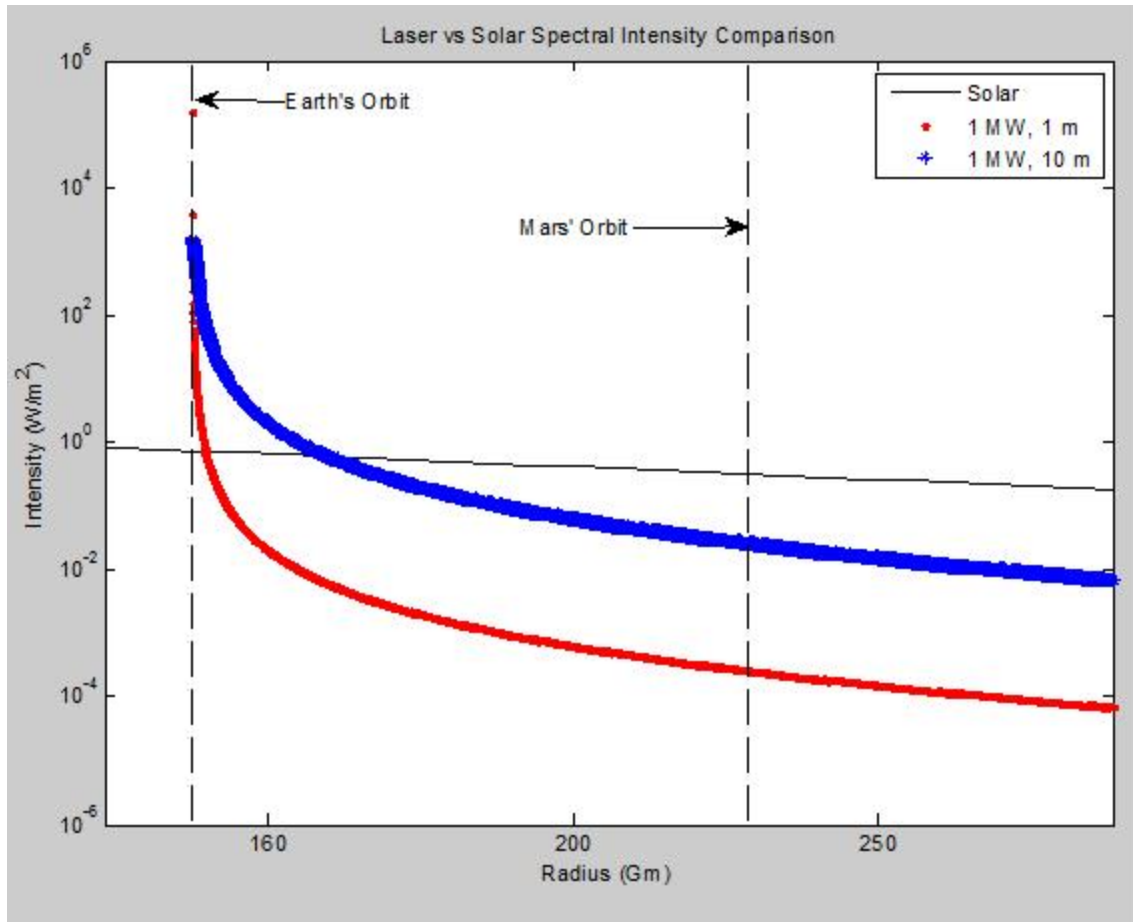
Figure 60.   Laser and Solar Intensities at Mars

E.   ILLUMINATING EXTRASOLAR BODIES

SETI, or the Search for Extraterrestrial Intelligence, is "a human project dedicated to explore, understand, and explain the origin, nature, and prevalence of life in the universe [56]." SETI runs a number of programs searching the electromagnetic spectrum for signs of extraterrestrial life, and, assuming the existence of such life, there may soon be a day when humans become aware of advanced civilizations elsewhere in the galaxy. Our current understanding of science indicates that given sufficient time and the right conditions, life could develop on other planets. Still, mankind has not yet developed or deployed efficient methods of communication over such large distances. This thesis will avoid the political implications of communication with an unknown and not-necessarily

peaceful extraterrestrial civilization. This section will seek to determine what laser characteristics might be necessary for successful interstellar propagation of a laser communications signal.

A casual survey of the night's sky indicates that light can travel across interstellar distances despite considerable losses. However, the power and size of a laser built for communication across interstellar distances would stretch the limits of our technology. The development of high-average power, continuous wave FELs, when paired with a hypothetical, large-radius director mirror, could offer the ability to successfully propagate a high-powered, laser beam through the atmosphere for interstellar communications. While other types of laser can offer similar average powers, they tend to operate in a pulsed mode with a large amount of energy per pulse. This leads to large losses within the atmosphere, and generally, it limits their utility for transmission over interstellar distances.

At extreme ranges, such as in transmission outside of the Solar System, a high-powered FEL can approach the spectral intensity of the Sun within its bandwidth, allowing for the possibility of interstellar communications. Extensions of the simulations presented below show that a lunar or orbiting laser of at least 10 MW with a 20 m director mirror will approximately match the solar spectral intensity at long ranges. While this is beyond current technologies, the constant development of laser, mirror, and space technologies indicate that a laser of this size may be achievable within the next century. Similarly, when combined with the previously discussed practical applications of high-powered lasers, it is reasonable to assume that another advanced civilization might already be utilizing a laser for these purposes. When beaming power for propulsion or communications within their own solar system, this hypothetical civilization may be emitting detectable signals in the direction of Earth. In this event, the simulations discussed here might provide some clue as to the nature of the incoming laser pulses.

These simulations model the propagation of a 10 MW FEL beam over interstellar distances. The laser is referred to as Laser 3, and it utilizes a director mirror with a radius

of 10 m. This system is a "pie-in-the-sky" design to estimate the laser characteristics required for interstellar communications and to possibly reduce the thermal blooming effects suffered by a smaller mirror.

The calculations provide estimates of beam diameter and intensities based solely on diffraction effects. As above, only 50% of the laser power is assumed to be transmitted through the atmosphere, but the additional beam spreading due to thermal blooming is not modeled. Similarly, these models assume perfect transmission across the interstellar medium.

Figure 61 displays the increase in beam radius due to diffraction versus the range of transmission. The closest star to our Sun, Alpha Centauri, is labeled at about 4 light-years away, and the probable minimum distance to other intelligent life, referred to here as the closest possible life, begins at least 10 light-years from Earth [57, p. 219]. For the 10 m mirror, the beam radius increases significantly over this range, growing to over 3.4 x 10^9 m. This radius is almost five times larger than the radius of our Sun (~6.96 x 10^8 m), but it is much smaller than our solar system, fitting easily inside of Mercury's orbital radius (~5.8 x 10^{10} m). Without knowing the configuration of any potential receiver or our pointing accuracy, it might be beneficial to produce a larger spot size to sweep out a larger portion of the target planetary system, but this would also further decrease the signal strength. Since habitable planets are expected to be within the limited orbital region where liquid water exists on a planet's surface, this spot size may be appropriate for targeting a specific orbital band within a distant solar system.
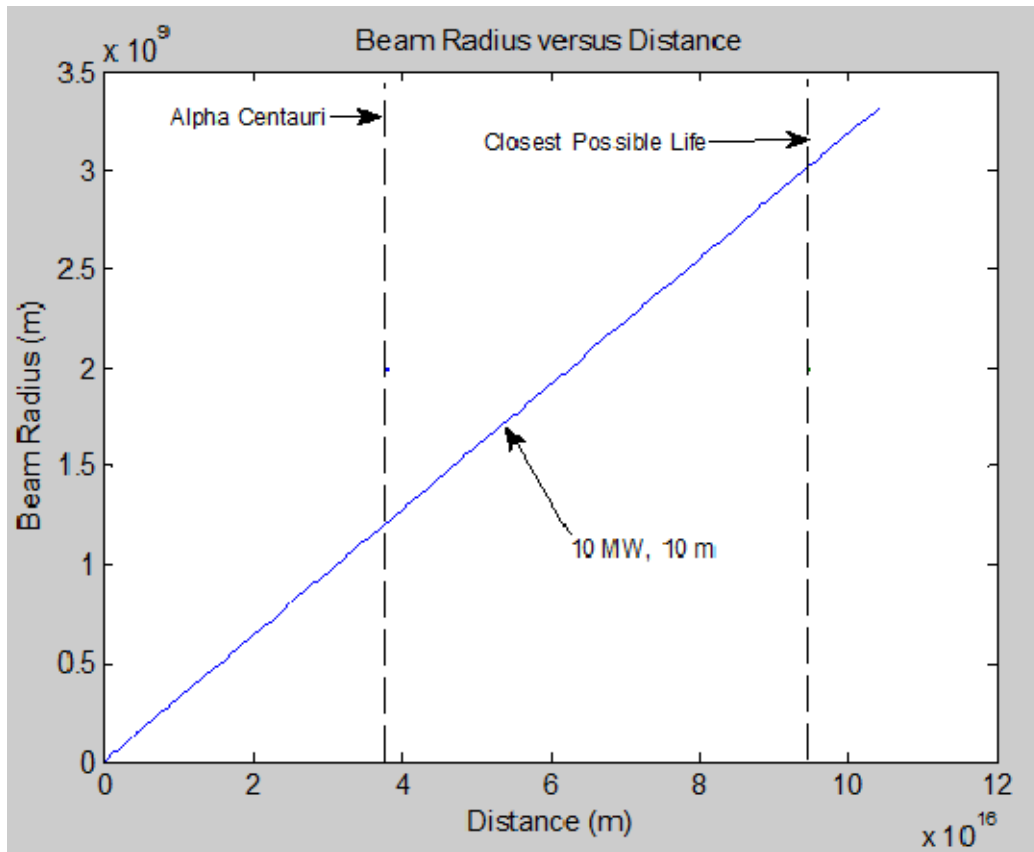
Figure 61.   Extrasolar Beam Radius Due To Diffraction

Figure 62 shows the comparison of average laser intensity and the total solar intensity. The laser is about four orders of magnitude below the total intensity of our Sun, but as displayed in Figure 63, the comparison of laser and solar spectral intensities presents a much more encouraging picture. At these ranges, the intensity of the Sun and the average laser intensity parallel each other with the laser remaining about one order of magnitude below the solar spectral intensity. The peak intensity of this laser should exceed the solar intensity by almost two orders of magnitude. With a SNR less than one, this laser signal will require advanced signal collection and processing to be recognized by a receiving civilization. The photons within these pulses should be detectable using a modern photon counter tube or photo-multiplier tube if gated properly to look at the right timing intervals. By setting a signal threshold to match the solar intensity, the receiver can isolate the laser transmitted photons and potentially detect the overlying signal.
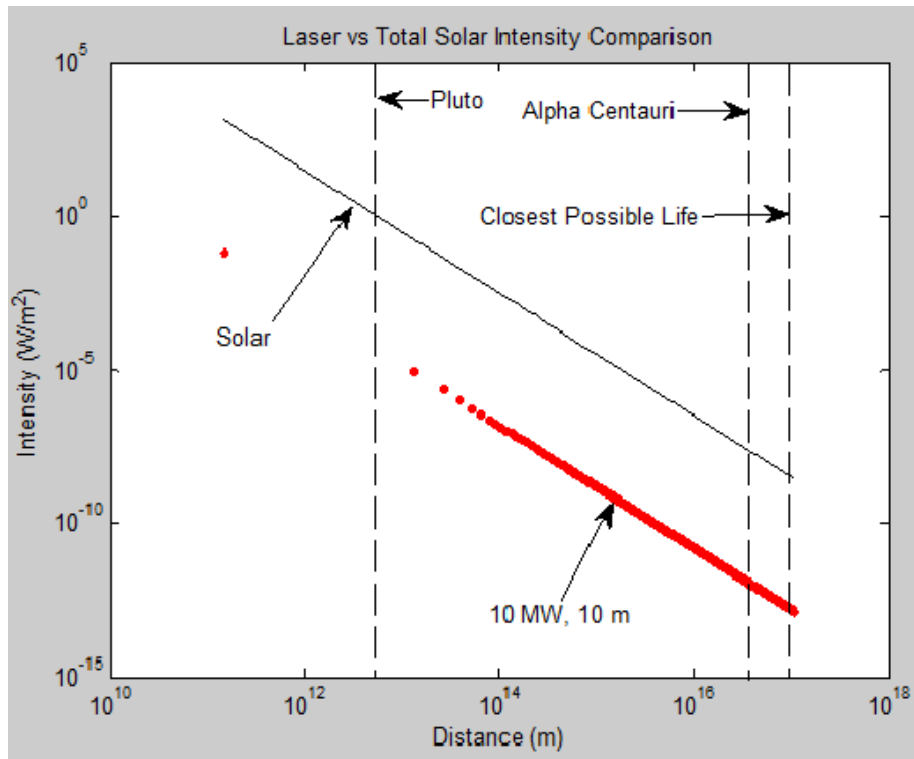
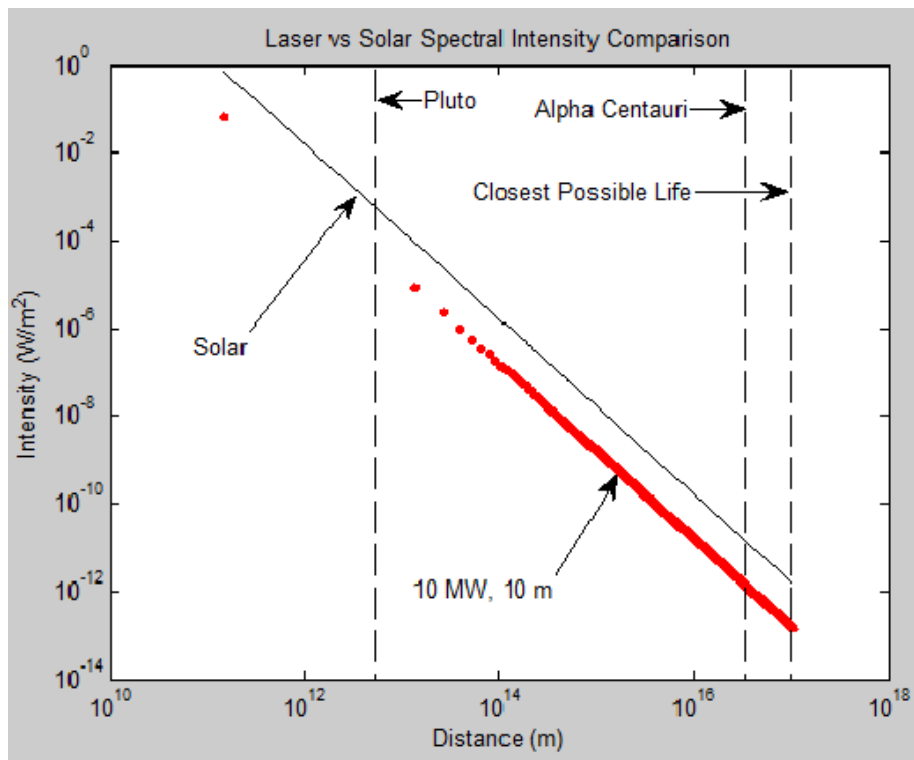Figure 62.   Extrasolar Total Intensity Comparison

Figure 63.   Extrasolar Spectral Intensity Comparison

126

For an advanced civilization with a receiving telescope similar to the Hubble Space Telescope (HST), the pulsation within these limited spectral bands might be within their ability to detect, but this is highly dependent on the signal processing methods utilized. The primary mirror of the HST is 1.2 m in radius [35, p. 82]. Equation (VII.1) displays a formula for the approximate number of photons received by a Hubble-like telescope that is 10 light years away from the Earth. For a wavelength of 1 μm, the number of photons per pulse is given by

$$\frac{\# photons}{pulse} = \frac{(5x10^9 W)(10^{-12} \sec)(1.6x10^{19} \; eV/J)}{(1.24 \; eV/photon)} \approx 6.5x10^{16}, \qquad \textbf{(VII.1)}$$

but these photons are spread over an extremely large beam radius. Therefore, the total number of photons per pulse collected by a hypothetical receiver is

$$\frac{\# photons\_received}{pulse} \approx 6.5x10^{16} \; \frac{photons}{pulse} \left(\frac{\pi (10m)^2}{\pi (3.4x10^9 m)^2} \right) \approx 1. \qquad \textbf{(VII.2)}$$

A Hubble-like telescope, 10 light years away from the Earth should receive about one photon per pulse from the signal transmitted by the laser. While this means that the receiver might not detect each individual pulse, the signal could be encoded over a timescale of tens of microseconds, allowing the receiver to collect millions of photons at a time. This method could presumably be used to provide an intelligent and non-random pattern and communicate the evidence of our existence to other advanced civilizations.

F.   DISCUSSION

In applications ranging from power beaming to the detection of Earth-threatening asteroids, the development and deployment of a high-powered, ground-based FEL could provide useful laser intensities at ranges stretching beyond the Martian orbit. For lunar illumination, the beam size and intensities support many possible applications, such as illumination for topographical mapping, scientific investigation of trace elements, and power beaming. At longer ranges near the Martian orbit, the laser intensities are less useful for power beaming but still offer many advantages for scientific illumination. Likewise, over the extreme ranges necessary for interstellar communications, the optical quality of an FEL beam allows for good propagation and provides the potential for eventual contact with extraterrestrial life. While the lasers required for these purposes are well beyond our current capabilities, the potential to detect and receive a similar signal transmitted to Earth exists and should be explored.

VIII. CONCLUSION

This thesis covered a broad range of space applications for a ground or sea based FEL. The beam quality, high-average power, and pulse structure of an FEL give it many advantages over other lasers in the illumination of samples at extremely long ranges. If utilized for power beaming to satellites, a limited ground infrastructure of one or two lasers could support specific missions or orbits, such as a sun-synchronous imaging satellite. Likewise, beaming power to many GEO satellites might be accomplished with relatively few ground stations placed in equatorial regions. However, it is concluded here that power beaming will not truly show its worth until satellites designed to receive laser illumination are constructed and deployed. By optimizing the satellite for power beaming, many of the complications in beam size, heating of the satellite body, and beam director pointing can be avoided or simplified. Due to these challenges, power beaming will probably first be utilized for propulsion of specialized spacecraft. The space tug discussed in Chapter V is a promising technology that could both reduce the costs of satellite launches and reduce the risks due to orbital debris by removing non-functional spacecraft from useful orbits.

Orbital debris is the most challenging problem facing mankind's future utilization of space. Some unmanned missions have already suffered catastrophic failures due to collisions with orbital debris, and the risks are mounting for future manned missions as the debris population grows. Recent implementation of debris reduction policies within NASA and throughout the international community will not reduce the current debris population or mitigate the growth of this population as older and larger objects continue to experience fragmentation events. The anticipated orbital lifetime of debris in the 800-1100 km range is on the order of 10,000 years, so some active removal method must be deployed to assure the safety of future space missions. This thesis proved that the FEL is not an effective option for the removal of space debris. The peak power of an FEL is too low to cause a Δv, due to the ablation of surface material, and the average power is not large enough to overcome the radiative losses of thermal energy and cause vaporization

of the debris particle. Still, an FEL may be useful to assist in the optical tracking of small debris particles, with sizes < 10 cm, that are difficult to track with radar alone.

A large, ground-based FEL could provide useful scientific illumination of extraterrestrial objects within the Solar System for ranges extending beyond the Martian orbit. There are many potential applications of this technology including the detection of asteroids, radar-like mapping of surface features, and the spectral search for specific elements. The assumed deployment of a MW-class FEL aboard future naval combatants offers a good opportunity to test the limits of this hypothetical system and demonstrate its scientific utility. Further research suggests that the optical quality of an FEL beam would be a suitable candidate for interstellar communications. Although the director mirrors and lasers discussed in Chapter VII slightly exceed our current technologies, interested Earth-bound researchers or organizations, such as SETI, might search for communications from extraterrestrial sources buried in the spectral content of their associated stars.

A.   FUTURE WORK

There exists a wide and interesting variety of scientific and engineering challenges within the topics discussed in this paper, but many of the findings presented here represent rough estimations of the capabilities of a high-energy FEL. This thesis was intended to guide future research in these fields toward topics that are theoretically feasible and away from those that are immediately proven impractical due to basic orbital motion or laser characteristics. In most cases, simplifying assumptions were made, most prominently in the atmospheric propagation of the laser, and future simulations or studies could more accurately measure the total effect of the many variables listed in each case.

In all cases, the atmosphere was assumed to remove about 50% of the laser power, based on the included atmospheric transmission graphs in Chapter III, but turbulence and thermal blooming effects were mostly ignored. Future research could simulate the propagation of a high power FEL beam when transmitted vertically through the atmosphere for the development of better modeling and mitigation methods for thermal blooming effects. Other possible continuations of this research are discussed below.

1. Power Beaming to Satellites

In Chapter V, this thesis discussed various terrestrial simulations and experiments utilizing the nearly monochromatic illumination of photovoltaic cells to deliver greater efficiencies. Future research could simulate the variation in laser intensity on the solar panels of an orbiting satellite. This intensity profile could then be translated into an actual power profile for the satellite. Similarly, as a collaboration with the NPS CubeSat program, future researchers could organize an experimental on-orbit illumination of a CubeSat by a ground based laser for measurement of the power delivered, tracking methods, and possibly attempt to anneal the solar cells of an older satellite.

2. Orbital Debris Removal

In Chapter VI, this thesis discussed the removal of orbital debris through laser illumination and heating. Although the simulations for this application seemed discouraging, significant heat can be delivered to a particle of debris. The calculations here restricted the debris to a pure aluminum sphere, whereas the actual debris population in much more complex and diverse. Depending on the specific composition of the targeted debris, laser illumination may be able to reduce the size of some types of orbital debris below the limits of current spacecraft shielding. Future research could model laser illumination of a more realistic debris particle to simulate the thermal and orbital effects or study the illumination of orbital debris to aid in detection of smaller debris particles.

3. Illuminating Extraterrestrial Bodies

In Chapter VII, this thesis discussed the illumination of extraterrestrial bodies with a high power FEL for scientific study. Future research could more accurately describe the desired signal and the cross correlation filter that would be required for radar-like applications within the solar system. The interstellar calculations were encouraging, but the lasers described represent a futuristic power and mirror size for the laser. Future research could better define the propagation effects of the interstellar medium and model the peak intensity of a laser for comparison to the solar intensity at long ranges.

THIS PAGE INTENTIONALLY LEFT BLANK

APPENDIX A: GLOSSARY

- **Albedo -** the direct reflection of solar energy from the Earth's surface that later illuminates and heats a satellite in Earth orbit

- **Apogee -** the point in an Earth orbit in which the orbiting object is farthest from the Earth

- **Argument of Perigee -** the angle between the line extending from the center of the Earth to the ascending node of an orbit and the line extending from the center of the Earth to the perigee point in the orbit measured from the ascending node in the direction of motion of the satellite

- **Attitude -** the orientation of a spacecraft as determined by the inclination of its axis with respect to a fixed reference point on Earth

- **Ascending Node -** the point on the ground track of a satellite's orbit where the subsatellite point (SSP) crosses the equator passing from the Southern to the Northern Hemisphere

- **Atmospheric Turbulence -** refers to fluctuations in the index of refraction resulting from small temperature fluctuations

- **Beam Waist -** the smallest spot size along the propagation path of a collimated or convergent beam where the on -axis irradiance is a maximum and the phase front radius of curvature is infinite

- **Beam Wander -** deflection of the beam centroid from the boresight of the optical wave

- **Coherence (spatial) -** the ability of a light beam to interfere with a spatially shifted version of itself

- **Coherence (temporal) -** the ability of a light beam to interfere with a delayed version of itself

- **Collimated Beam -** a Gaussian -beam wave with phase front radius of curvature that is infinite at the transmitter (beam waist is located at the transmitter)

- **Delta -V -** the change in velocity vector of an object

- **Descending Node -** the point on the ground track of a satellite's orbit where the subsatellite point (SSP) crosses the equator passing from the Northern to the Southern Hemisphere

- **Downlink -** the communications link from a satellite down to one or more ground stations

- **Eccentricity -** a fixed constant for each type of conic section representing an orbit's "roundness"

- **Ecliptic -** the apparent path that the Sun traces out in the sky during the year
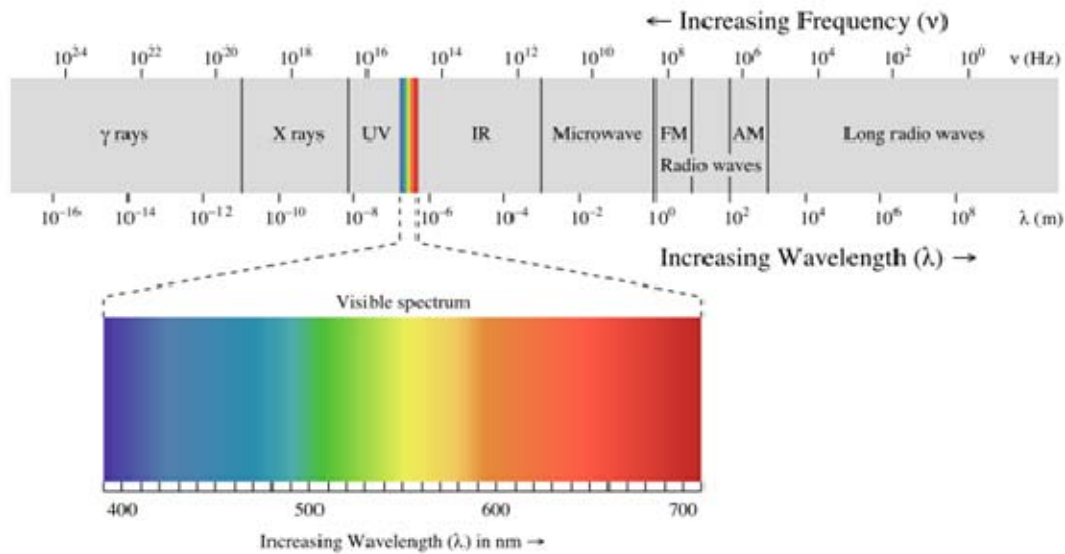
- **Electromagnetic Spectrum -**

Figure 64.   Electromagnetic Spectrum. From [58]

- **Ephemeris -** a table of values that gives the positions of astronomical objects in the sky at a given time

- **Epoch -** specifies the reference time for a set of orbital elements

- **Elliptical Orbit -** a Keplerian orbit with an eccentricity of less than one; this includes the special case of a circular orbit, with an eccentricity of zero

- **Far Field -** also called the Fraunhofer Region.

- **Fraunhofer Region -** the region outside the near -field region where the angular field distribution is essentially independent of distance from the source

- **Fresnel Region -** the close -in region of an antenna where the angular field distribution is dependent upon the distance from the antenna

- **Gaussian Beam -** a beam of electromagnetic radiation whose wave front is approximately Gaussian (parabolic) at any point along the path and whose transverse field intensity over any wavefront is a Gaussian function of distance from the beam axis (refers to the lowest order mode)

- **Geostationary Orbit -** an orbit at zero degrees inclination at an altitude of 35,687 km that precisely matches the Earth's angular velocity, thereby keeping the satellite at a stationary point in the sky when viewed from the ground

- **Ground Station -** a terrestrial terminal station designed for communication with spacecraft

134

- **Ground Track -** the path on the surface of the Earth traced out directly below a satellite

- **Heterodyning -** mixing or multiplying two oscillating waveforms, used in modulating or demodulating signals

- **Inclination -** the angle the orbit plane makes with the equatorial plane

- **Index of Refraction -** the ratio of the phase velocity of light in a vacuum to that in a specified medium

- **Intensity -** a measure of the power per unit area of an illumination source

- **I_{sp} -** specific impulse; a way to describe the efficiency of jet or rocket engines. It represents the change in momentum per unit amount of propellant used

- **Keplerian Elements -** seven numbers used to describe the orbit of an object. These numbers define an ellipse, orient it about the Earth, and place the satellite on the ellipse at a particular time. The basic orbital elements are: epoch, orbital inclination, RAAN, argument of perigee, eccentricity, mean motion, and mean anomaly

- **Lorentz Force -** the force on a point charge due to electromagnetic fields, given by the equation $\vec{F} = q\left(\vec{E} + \vec{v} \times \vec{B}\right)$

- **Near -Field Region -** also called the Fresnel Region

- **Orbital Debris -** any man -made object in Earth orbit which no longer serves a useful purpose

- **Orbital Elements -** see Keplerian elements

- **Perigee -** the point in the orbit that is nearest the Earth

- **Perturbation -** deviation from a normal, idealized, or undisturbed motion

- **Phase front -** a surface of constant phase (also called a wave front)

- **Plane Wave -** a wave in which the phase fronts form parallel planes

- **Rayleigh Range (z_R) -** defines the distance along the propagation axis on either side of the beam waist up to the point where the beam spot size doubles

- **Refraction -** a change in the direction of propagation of any wave

- **Resolution -** the ability of an optical system to resolve details in an object being imaged

- **Right Ascension of the Ascending Node (RAAN) -** the angle between the line extending from the center of the Earth to the ascending node of an orbit and the line extending from the center of the Earth to the vernal equinox measured from the vernal equinox eastward in the Earth's equatorial plane

- **Scintillation -** refers to either temporal or spatial fluctuations in the irradiance of an optical wave (e.g., star twinkle)

- **Spontaneous Emission -** the process by which an electron, initially in a higher energy state, spontaneously drops to a lower energy state by emitting a photon whose energy exactly matches the difference in states

- **Spot Size -** refers to the $1/e$ beam radius of a Gaussian beam

- **Stimulated Emission -** the process by which an electron, stimulated in the presence of an electromagnetic wave, emits a photon with the same phase, frequency, polarization, and direction of travel as the original wave

- **Sub -Satellite Point -** the point on the Earth's surface directly below a satellite, i.e., on a line between the center of the Earth and the satellite center

- **Sun Soak/Bathe -** When a satellite orients its solar panels towards the sun for maximum battery charging. Often, mission requirements might require prolonged periods of operation without the solar arrays optimally aligned, normal to the incident solar rays.

- **Sun -Synchronous Orbit -** a satellite orbit that matches the precession of perigee to counter the daily orbital motion of the Earth around the Sun; this produces an orbit that passes overhead at the same local time

- **Synchrotron Radiation -** electromagnetic radiation generated by the acceleration of relativistic charged particles by a magnetic field

- **Vernal Equinox -** the direction of the Sun in space when it passes from the southern hemisphere to the northern hemisphere and appears to cross the Earth's equator (about 20 March). The vernal equinox is the reference point for measuring angular distance along the Earth's equatorial plane (right ascension), and one of two angles used to locate objects in orbit the other is declination)

- **Wave front -** see phase front

APPENDIX B: SIMULATION SETTINGS & RESULTS

This appendix outlines the specific settings within STK version 8 that were utilized in the simulations of Chapter V. All simulations were conducted with a Coordinate Epoch of 1 Jan 2000 11:58:55.816 UTCG for each scenario, and the scenarios ran over a one week period from 1 Jul 2007 to 8 Jul 2007.

Figure 65.   Sun Synchronous Satellite from Simulation One

Figure 66.   Ship with Laser in Simulation One

```
Global Statistics      Time (UTCG)          Azimuth (deg)   Elevation (deg)   Range (km)
------------------   --------------------   -------------   ---------------   ------------
Min Elevation        3 Jul 2007 15:59:36.365    179.779          10.000        1844.238511
Max Elevation        7 Jul 2007 16:03:20.787    269.881          89.964         561.991758
Mean Elevation                                                   31.181
Min Range            7 Jul 2007 16:03:20.787    270.675          89.964         561.991759
Max Range            1 Jul 2007 16:07:45.866      0.223          10.001        1844.425758
Mean Range                                                                     1245.531267
```

Figure 67.   Global In-View Azimuth, Elevation, and Range Summary for Simulation One

Figure 68.   Sun Synchronous Satellite from Simulation Two

Figure 69.   Laser Equipped Ship in Simulation Two

138

Global Statistics	Time (UTCG)	Azimuth (deg)	Elevation (deg)	Range (km)
Min Elevation	3 Jul 2007 16:04:22.712	313.247	10.000	1842.811122
Max Elevation	7 Jul 2007 14:27:54.598	89.232	17.184	1437.429344
Mean Elevation			13.106	
Min Range	7 Jul 2007 14:27:54.598	89.232	17.184	1437.429344
Max Range	7 Jul 2007 16:05:17.145	315.257	10.000	1843.723943
Mean Range				1658.704517

Figure 70.   Global In-View Azimuth, Elevation, and Range Summary for Simulation Two

Figure 71.   Mid-Inclination Satellite with Zero RAAN from Simulation Three

Figure 72.   Laser Equipped Ship DDL1 from Simulation Three

139

Figure 73.   Laser Equipped Ship DDL2 from Simulation Three

Figure 74.   Laser Equipped Ship DDL3 from Simulation Three

Figure 75.   Laser Equipped DDL4 from Simulation Three

```
Imager3-To-DDL1
----------------

Global Statistics        Time (UTCG)         Azimuth (deg)    Elevation (deg)    Range (km)
-----------------   ------------------------  -------------    ---------------    ----------
Min Elevation       5 Jul 2007 17:40:42.273        87.221            -60.386      464.860113
Max Elevation       4 Jul 2007 17:00:34.009       235.251            -22.075     1439.835159
Mean Elevation                                                       -28.410
Min Range           5 Jul 2007 17:40:42.275        87.225            -60.386      464.860113
Max Range           4 Jul 2007 17:00:34.009       235.251            -22.075     1439.835159
Mean Range                                                                       1105.574154

Imager3-To-DDL2
----------------

Global Statistics        Time (UTCG)         Azimuth (deg)    Elevation (deg)    Range (km)
-----------------   ------------------------  -------------    ---------------    ----------
Min Elevation       5 Jul 2007 11:30:14.516       267.316            -74.207      416.740603
Max Elevation       5 Jul 2007 11:33:28.652       182.080            -22.075     1439.835168
Mean Elevation                                                       -29.046
Min Range           5 Jul 2007 11:30:14.542       267.224            -74.207      416.740561
Max Range           5 Jul 2007 11:27:00.407       352.327            -22.075     1439.835173
Mean Range                                                                       1105.875317

Imager3-To-DDL3
----------------

Global Statistics        Time (UTCG)         Azimuth (deg)    Elevation (deg)    Range (km)
-----------------   ------------------------  -------------    ---------------    ----------
Min Elevation       4 Jul 2007 06:14:36.701        87.123            -74.456      416.198676
Max Elevation       5 Jul 2007 05:16:43.221       337.233            -22.075     1439.835167
Mean Elevation                                                       -29.254
Min Range           4 Jul 2007 06:14:36.730        87.224            -74.456      416.198626
Max Range           5 Jul 2007 05:16:43.221       337.233            -22.075     1439.835167
Mean Range                                                                       1093.305861

Imager3-To-DDL4
----------------

Global Statistics        Time (UTCG)         Azimuth (deg)    Elevation (deg)    Range (km)
-----------------   ------------------------  -------------    ---------------    ----------
Min Elevation       6 Jul 2007 22:56:20.087        87.214            -89.319      400.030061
Max Elevation       6 Jul 2007 22:59:34.890       176.998            -22.075     1439.835168
Mean Elevation                                                       -29.681
Min Range           6 Jul 2007 22:56:20.087        87.219            -89.319      400.030061
Max Range           4 Jul 2007 00:00:57.016       347.212            -22.075     1439.835171
Mean Range                                                                       1061.801251
```

Figure 76.   Global In-View Azimuth, Elevation, and Range Summary for Simulation Three

141

THIS PAGE INTENTIONALLY LEFT BLANK

APPENDIX C: ORBITAL DEBRIS THERMAL ESTIMATE

Figure 77 is a Microsoft Excel spreadsheet used to approximate the initial temperature of the aluminum sphere in Chapter VI.

Item	Symbol	Debris	Units	Source	Cell Equations
Altitude	H	700.0	km	Given	
Inclination	i	90			
Solar/orbit angle	β	0			
Orbit angle from SSP	vo	0			
Earth angular radius	rho	1.122	radians	Eq. 5-16	=ASIN(Re/(Reo+Ho))
Earth view factor=(1-cosp)/2	Fe	0.283	----	pg448 data	=(1-COS(rho))/2
Albedo view factor=Fecos(β)cos(vo)	Fa	0.283			=Feo*COS(bo)*COS(E5)
Surface area (main body only)	A	0.008	m^2	Geometry	=4*PI()*(Do/2)^2
Diam. of equivalent sphere	D	0.050	m		
Daytime Laser power input	Qeqmax	0	W		
Night time laser illumination	Qeqmin	0	W		
MaxEarth IR emission @ surface	Emax	258	W/m^2	SMAD	
Min Earth IR emission @ surface	Emin	216	W/m^2	SMAD	
Direct solar flux	S	1366	W/m^2	SMAD	
Albedo	al	0.35		Given	
Emmisivity	em	0.7	---	by design	
Absorptivity (solar)	af	0.6	---	by design	
Sphere x-section area=πD^2/4	Ap	0.002	m^2	Geometry	=PI()*Do^2/4
Solar input	Ap*S*af	1.6	W	calc	=Apo*So*afo
Environme Earth input	A*Fe*Emax*em	0.4	W	calc	=Ao*Feo*Emaxo*emo
Albedo input	A*Fa*S*al*af	0.6	W	calc	=Ao*Fao*So*alo*afo
	em*A	0.005498	m^2	calc	=emo*Ao*(1)
Worst case hot temp (w/o mass)	Tmax*	303.6	C	calc	=((E20+E21+E22+Qeqmaxo)/(sgo*emo*Ao))^0.25
Worst case cold temp (w/o mass)	Tmin	181.2	C	calc	=((Ao*Feo*Emino*emo+Qeqmino)/(sgo*emo*Ao))^0.25
Orbit period	Po	5926.4		calc	=2*PI()/SQRT(muo/(Reo+Ho)^3)
Eclipse period	Pe	2117.2		calc	=IF(rhoo>bo, Poo*ACOS(COS(rhoo)/COS(bo))/PI(),0)
Sunlight period	Ps	3809.2		calc	=Poo-Peo
Mean temperature ~K	Tm	276.5	K	calc	=((Pso*(Tmaxo)^4+2117*(Tmno)^4)/Poo)^0.25
Particle mass ~ kg	m	0.177	kg	given	
Particle heat capacity ~ J/kg.K	cp	900	J/kg.K	given	
Day time constant	Ks	5.10E-02	K/s	calc	=((E20+E21+E22+Qeqmaxo)+3*sgo*emo*Ao*Tm^4)/mo/cpo
Night time constant	Ke	3.64E-02	K/s	calc	=((Ao*Feo*Emino*emo+Qeqmino)+3*sgo*emo*Ao*Tm^4)/mo/cpo
Slope ~ 1/sec	k	1.66E-04	s^{-1}	calc	=4*emo*sgo*Ao*Tm^3/mo/cpo
Upper temperature (w/ mass)	Tu	285.8	K	calc	=(Ks+(Keo-Ks)*eo^(-ko*Pso)-Keo*eo^(-ko*Poo))/ko/(1-eo^(-ko*Poo))
Lower temperature (w/ mass)	Tl	266.4	K	calc	=(Tuo*eo^(-ko*Peo) + Keo*(1-eo^(-ko*Peo))/ko

Re 6378.1
mu 398600.4
S-B sigma 5.67E-08
e 2.718282

Figure 77.   Thermal Temperature Calculations for a 5 cm Sphere of Aluminum at an Altitude of 700 km

The following MATLAB code was used to calculate the temperature of a debris particle illuminated during the daylight. The results are discussed and included in Chapter VI.

```matlab
% LCDR Benjamin Wilder
% Master's Thesis Work- Time to vaporize a debris particle
% Summary- This MATLAB m file was created in MATLAB 7.7.0 (R2008b).  It
% assumes a homogeneous, spherical debris particle of pure aluminum.

clear all; close all; clc;
% Constants
To = 270;                         % Initial Temp in K
da = 2.702;                       % Density of aluminum in g/cm^3
d = da*(100^3)/1000;              % Density of aluminum in kg/m^3
cs = 0.910*1000;                  % Specific Heat Capacity in J/K-kg
Tm = 933;                         % Melting Temp in K
Lf = 397*1000;                    % Latent Heat of Fusion in J/kg
Tb = 2723;                        % Boiling Temp in K
Lv = 11400*1000;                  % Latent Heat of Vaporization
sigma = 5.67e-8;                  % Boltzman's constant in W/m^2-K^4
e = 0.7;                          % emissivity of aluminum

% Inputs
r = 2.5/100;                      % Initial radius of the debris in m
rf = 1/100;                       % Final radius of the debris in m
Plt1 = 5e6;                       % Power of the laser at the target
rbt1 = 0.4;                       % Beam radius at the target in m

% Calculations
Vo = 4*pi*(r^3)/3;                % Initial volume of the debris in m^3
Ao = pi*r^2;                      % Cross sectional area of the debris
As = 4*pi*r^2;                    % Surface area of the particle
m = Vo*d;                         % Mass of the particle in kg
Vf = 4*pi*(rf^3)/3;               % Final volume of the debris in m^3
mf = Vf*d;                        % Final mass of the particle in kg

Ilaser1 = Plt1/(pi*rbt1^2); % Laser 1 intensity at the target in W/m^2

Pin1 = Ilaser1*Ao+1366*Ao; % Power received by the debris particel in W

% Calculate the time to heat to melting temperature
T(1) = To;                        % Initialize temp
t(1) = 0;                         % Initialize time in seconds
deltat=0.01;                      % Time step in seconds
n = 1;                            % Creates an array number for t and T
while T(n) < Tm
    n = n + 1;
    t(n) = t(n-1) + deltat;           % Current time in seconds
    Prad = e*sigma*((T(n-1)-3)^4)*As;% Radiated power by the particle
    Pdif = (Pin1-Prad);               % Power difference
    deltaT = Pdif*deltat/(m*cs);   % Change in temp due to power (in K)
    T(n) = T(n-1) + deltaT;        % Current temp
    if t(n) > 700
```

144

```matlab
        break
    end
end
T(n)
t(n)

% Calculate the time to complete the phase transition (melting)
Q = 0;                                  % Initializing the Q counter
Qm = m*Lf;                              % Heat required to melt in J
while Q < Qm
    if t(n) > 700
        break
    end
    n = n +1;
    t(n) = t(n-1) + deltat;             % Time counter in seconds
    Prad = e*sigma*((T(n-1)-3)^4)*As;   % Radiated power by the particle
    Pdif = (Pin1-Prad);                 % Power difference
    Q1 = Pdif*deltat;                   % Change in temp due to power (in K)
    Q = Q + Q1;                         % Heat counter in J
    T(n) = Tm;                          % Keeps track of T for t
end

% Calculate the time to heat to boiling temperature
while T(n) < Tb
    n = n + 1;                          % Counter
    t(n) = t(n-1) + deltat;            % Current time in seconds
    Prad = e*sigma*((T(n-1)-3)^4)*As;  % Radiated power by the particle
    Pdif = (Pin1-Prad);                % Power difference
    deltaT = Pdif*deltat/(m*cs);       % Change in temp due to power (in K)
    T(n) = T(n-1) + deltaT;            % Current temp
    if t(n) > 700
        break
    end
end

% Calculate the time to complete the phase transition (boiling)
Q2 = 0;                                 % Initializing the Q counter
Qb = m*Lv;                              % Heat required to melt in J
while Q2 < Qb
    if t(n) > 700
        break                          % ends the loop if program is too long
    end
    n = n + 1;
    t(n) = t(n-1) + deltat;           % Time counter in seconds
    T(n) = Tb;
    Prad = e*sigma*((T(n-1)-3)^4)*As;  % Radiated power by the particle
    Pdif = (Pin1-Prad);                % Power difference
    Qdif = Pdif*deltat;                % Change in temp due to power (in K)
    Q2 = Q2 + Qdif;                    % Heat counter in J
End
% Plot the results
figure(1); plot(t,T);
title('Temperature vs Time'); ylabel('Temp (K)'); xlabel('Time (s)');
axis([0 700 270 Tb+100]); Tmline(1); Tbline(1); Tbtext(1); Tmtext(1);
```

145

THIS PAGE INTENTIONALLY LEFT BLANK

APPENDIX D: ILLUMINATION MATLAB CODE

The following code was created in support of the calculations discussed in Chapter VII. The contributions of LCDR Sean Niles and LT Justin Jimenez in programming advice and debugging are greatly appreciated. [59] [60]

```matlab
% LCDR Benjamin Wilder, USN
% Masters thesis work- Illumination of extraterrestrial bodies
% This work was conducted within MATLAB 7.7.0 (R2008b)
% Summary- This m file will utilize Planck's analytical expression for
% the Stefan-Boltzman Law to calculate the irradiance of the Sun by
% approximating it as a blackbody with a temperature of 5800 K.
% Specifically, the power is calculated within the limited 1 nm
bandwidth
% of an FEL operating at 1 micrometer.  This irradiance is plotted
versus
% radius from the Sun and compared to the irradiance of free elctron
% lasers of varying mirror size and total power

% The contributions of LCDR Sean Niles and LT Justin Jimenez in
programming
% advice and debugging is greatly appreciated.

clear all; close all; clc; format long e;

%% Constants and Parameters
% FEL paramters
wo1 = 1;                        % Mirror radius in m
wo2 = 10;
wo3 = 20;
Pl = 0.5e6;                      % Power of the Laser outside the
atmosphere
Pl3 = 5e6;
wavelength = 1e-6;              % wavelength in m
zo1 = pi*wo1^2/wavelength       % Rayleigh Range
zo2 = pi*wo2^2/wavelength;
zo3 = pi*wo3^2/wavelength;
bandwidth = 0.1;                % bandwidth in %
% Given or Assumed Constants
h = 6.6260693e-34;             % Planck's Constant in J-sec
k = 1.380658e-23;              % Boltzman's cosntant in J/K
c = 2.9978e8;                  % Speed of light in m/sec
T = 5800;                       % Blackbody Temperature in Kelvin

%% Create the total blackbody curve

% wavelength range
lambda = linspace(0.5e-7,5e-6,1000);

% compute intensity per m at each point
```

```matlab
M = (2*pi*c^2*h)./(lambda.^5).*1./(exp((h*c)./(lambda.*k*T))-1);


% integrate area under curve
I_func =
@(lambda)(2*pi*c^2*h)./(lambda.^5).*1./(exp((h*c)./(lambda.*k...
    *T))-1);
I_band  = quad(I_func,0.9995e-6,1.0005e-6)
I_tot   = quad(I_func,0.5e-6,11e-6)


Percentage = I_band*100/I_tot;          % The percentage of solar output
                                        % within the laser bandwidth


%% Calculate the Sun's total power for later comparison output to the
laser

% Constants from Orbital Mechanics Textbook
Rs =     6.96e8;                    % Solar Radius in m
Re =    149.6e9;                    % Earth Orbital Semi-major Axis
Rmoon = 384.4e6;                    % Lunar Semi-major Axis
Rmars = 227.9e9;                    % Mars Orbital Semi-major Axis
Rjupt = 778.6e9;                    % Jupiter Orbital Semi-major Axis
Rsatn = 1.433e12;                   % Saturn Orbital Semi-major Axis
Ruran = 2.872e12;                   % Uranus Orbital Semi-major Axis
Rnept = 4.495e12;                   % Neptune Orbital Semi-major Axis
Rpluto = 5.87e12;                   % Pluto Orbital Semi-major Axis


Psun = 4e26;                        % The estimated total solar power
output
Isunsurf = Psun/(4*pi*((Rs)^2))  % The Total Solar Intensity at the
surface
%% Creating the laser and solar intensity comparison

FF = 8001;                          % Number of steps to be calc'd
Minradius = 1.4e11;
Maxradius = 3e11;
Diffradius = (Maxradius-Minradius)/(FF-1);
for F=1:FF
r = Minradius + (F-1)*Diffradius;
R(F) = r;
Isuntot(F) = Isunsurf*(Rs/r)^2;     % Total solar intensity at r in
W/m^2
Iband(F) = I_band*(Rs/r)^2;         % Spectral solar intensity at r in
W/m^2
if r>= Re
    w1 = wo1*sqrt(1+((r-Re)/zo1)^2);
    Ilaser(F) = Pl/(pi*(w1)^2);  % Laser Intensity at radius r
    w2 = wo2*sqrt(1+((r-Re)/zo2)^2);
    Ilaser2(F) = Pl/(pi*(w2)^2);  % Laser Intensity at radius r
    w3 = wo3*sqrt(1+((r-Re)/zo3)^2);
    Ilaser3(F) = Pl3/(pi*(w3)^2);  % Laser Intensity at radius r
else
end
end
```

```matlab
%% Plot the results
figure(1);
plot(lambda,M,'-b', 'linewidth',2);
xlabel('Wavelength (m)');
ylabel('M (W/m^3)');
title('Solar Blackbody Approximation');
hold on; laserbandwidth(1);
annotation('textbox', [0.3 0.4 0.3 0.1],...
    'Interpreter','tex','Edgecolor','none',...
    'String',['% of solar output within the laser bandwidth is ' ...
    num2str(Percentage)],'FitBoxToText','on');

figure(2);                              % plot  total solar intensity vs
laser
loglog(R, Isuntot, '-k', R, Ilaser, '.r', R, Ilaser2, '*b', Re, 1e5,
...
    'ob', Rmars, 1e5, 'ob');
h = legend('Solar','1 MW, 1 m','1 MW, 10 m',1); earthbox(2);
marsbox(2);
hold on;
title('Laser vs Total Solar Intensity Comparison');
ylabel('Intensity (W/m^2)'); xlabel('Radius (m)');

figure(3);
loglog(R, Iband,'-k', R, Ilaser, '.r', R, Ilaser2, '*b', Re, 1e5, 'ob',
...
    Rmars, 1e5, 'ob');
h = legend('Solar','1 MW, 1 m','1 MW, 10 m',1); earthbox(3);
marsbox(3);
hold on;
title('Laser vs Solar Spectral Intensity Comparison');
ylabel('Intensity (W/m^2)'); xlabel('Radius (m)');

%% Compute and plot the Spot Size versus distance
O=8001;
Rmin=1e3;
Rmax=Rmars;
Diffradius = (Rmax-Rmin)/(O-1);
for F=1:O
r = Rmin + (F-1)*Diffradius;
R1(F) = r;
w1(F) = wo1*sqrt(1+(r/zo1)^2);            % Beam radius in m
A1(F) = (pi*(w1(F))^2);                   % Spot size in m^2
Ilaser(F) = Pl/A1(F);                     % Laser Intensity at radius
r
w2(F) = wo2*sqrt(1+(r/zo2)^2);            % Beam radius in m
A2(F) = (pi*(w2(F))^2);                   % Spot size in m^2
Ilaser2(F) = Pl/A2(F);                    % Laser Intensity at radius
r
w3(F) = wo3*sqrt(1+(r/zo3)^2);            % Beam radius in m
end

% plot the results
figure(4);
plot(R1,w1,'-b');
```

149

```
h = legend('1 MW, 1 m',2);
set(h,'Interpreter','none');
xlabel('Distance (m)');
ylabel('Beam Radius (m)');
title('Beam Radius vs Distance');

figure(5);
plot(R1,A1,'-b'); hold on;
h = legend('1 MW, 1 m',2);
set(h,'Interpreter','none');
xlabel('Distance (m)');
ylabel('Spot Size (m^2)');
title('Spot Size vs Distance');

figure(6);
plot(R1,Ilaser,'-b'); hold on;
h = legend('1 MW, 1 m',2);
set(h,'Interpreter','none');
xlabel('Distance (m)');
ylabel('Intensity (W/m^2)');
title('Intensity vs Distance');

figure(7);
plot(R1,w2,'-r');
h = legend('1 MW, 10 m',2);
set(h,'Interpreter','none');
xlabel('Distance (m)');
ylabel('Beam Radius (m)');
title('Beam Radius vs Distance');

figure(8);
plot(R1,A2,'-r'); hold on;
h = legend('1 MW, 10 m',2);
set(h,'Interpreter','none');
xlabel('Distance (m)');
ylabel('Spot Size (m^2)');
title('Spot Size vs Distance');

figure(9);
plot(R1,Ilaser2,'-r'); hold on;
h = legend('1 MW, 10 m',2);
set(h,'Interpreter','none');
xlabel('Distance (m)');
ylabel('Intensity (W/m^2)');
title('Intensity vs Distance');
```

The following m file supports the Extrasolar illumination discussions in Chapter VII, Section E.

```
% LCDR Benjamin Wilder, USN
% Masters thesis work- Illumination of extraSOLAR bodies
% This work was conducted within MATLAB 7.7.0 (R2008b)
% Summary- This m file will compare the spectral intensities of the
laser
% and the Sun within the laser bandwidth at extreme ranges.  Further
plots
% will show the laser spot size versus range from the Earth at star
systems
% of interest.

clear all; close all; clc; format long e;

%% Constants and Parameters
% FEL paramters
wo1 = 10;                        % Futuristic Mirror radius in m
wo2 = 100;                       % Pie-in-the-sky Mirror radius in m
Pl = 5e6;                  % Power of the Laser outside the atmosphere
wavelength = 1e-6;               % wavelength in m
zo1 = pi*wo1^2/wavelength;       % Rayleigh Range
zo2 = pi*wo2^2/wavelength;
bandwidth = 0.1;                 % bandwidth in %
% Given or Assumed Constants
h = 6.6260693e-34;               % Planck's Constant in J-sec
k = 1.380658e-23;                % Boltzman's cosntant in J/K
c = 2.9978e8;                    % Speed of light in m/sec
T = 5800;                        % Blackbody Temperature in Kelvin

%% Create the total blackbody curve

% wavelength range
lambda = linspace(0.5e-7,5e-6,1000);

% compute intensity per m at each point
M = (2*pi*c^2*h)./(lambda.^5).*1./(exp((h*c)./(lambda.*k*T))-1);

% integrate area under curve
I_func =
@(lambda)(2*pi*c^2*h)./(lambda.^5).*1./(exp((h*c)./(lambda.*k...
    *T))-1);
I_band  = quad(I_func,0.9995e-6,1.0005e-6)
I_tot  = quad(I_func,0.5e-6,11e-6)

%% Calculate the Sun's total power for later comparison output to the
laser
Rs =     6.96e8;                     % Solar Radius in m
Re =    149.6e9;                     % Earth Orbital Semi-major Axis
Rpluto = 5.87e12;                    % Pluto Orbital Semi-major Axis
Rpluto = Rpluto-Re;          % Shortest range to pluto from earth in m
Ralphacentari=4;             % Range to alpha centari in light years
```

```matlab
Rlife= 10;                        % Probable distance to nearest intelligent
                                  % life in light years
Rac = Ralphacentari*9.4605284e15; % Rac in m
Rlife= Rlife*9.4605284e15;        % Rlife in meters


Psun =    4e26                    % The estimated total solar power output
Isunsurf = Psun/(4*pi*((Rs)^2))% Total Solar Intensity at the surface
%% Creating the laser and solar intensity comparison

FF = 8001;                        % Number of steps to be calc'd
Diffradius = (Rlife*1.1-Re)/(FF-1);
for F=1:FF
r = Re + (F-1)*Diffradius;
R(F) = r;
Isuntot(F) = Isunsurf*(Rs/r)^2;  % Total solar intensity at r in W/m^2
Iband(F) = I_band*(Rs/r)^2;      % Spectral solar intensity at r in W/m^2
    w1(F) = wo1*sqrt(1+(r/zo1)^2);   % Beam radius in m
    Ilaser(F) = Pl/(pi*(w1(F))^2);   % Laser Intensity at radius r
    w2(F) = wo2*sqrt(1+(r/zo2)^2);   % Beam radius in m
    Ilaser2(F) = Pl/(pi*(w2(F))^2);  % Laser Intensity at radius r
end

%% Plot the results
% Plot the laser beam radius versus distance
figure(1);
plot(R,w1,'-b', Rac, 2e9, Rlife, 2e9);
createline1(1); createline2(1); actext1(1); cpitext1(1);
mirr1(1);
xlabel('Distance (m)');
ylabel('Beam Radius (m)');
title('Beam Radius versus Distance');

% plot the laser intensity versus the total solar intensity
figure(2);
loglog(R, Isuntot, '-k', R, Ilaser, '.r');
hold on;  plutotext2(2); plutoline2(2); actext2(2); acline2(2);...
    cpitext2(2); cpiline2(2); solar2(2); mirror1(2);
title('Laser vs Total Solar Intensity Comparison');
ylabel('Radius (m)'); xlabel('Distance (m)');

% plot the laser intensity versus the solar intensity in the laser
% bandwidth
figure(3);
loglog(R, Iband,'-k', R, Ilaser, '.r');
hold on; plutoline3(3); acline3(3); solar3(3);
cpiline3(3); plutotext3(3); cpitext3(3); actext3(3); mirror3(3);
title('Laser vs Solar Spectral Intensity Comparison');
ylabel('Intensity (W/m^2)'); xlabel('Distance (m)');
```

LIST OF REFERENCES

[1]   J. Hecht, *Beam: The Race to Make the Laser*. New York, NY: Oxford University Press, 2005.

[2]   J. Hecht, *Laser Pioneers*. New York, NY: Academic Press, 1992.

[3]   W.B. Colson, C. Pellegrini, and A. Renieri, *Free Electron Laser Handbook*. Amsterdam, The Netherlands: Elsevier Science Publishing Company, Inc, 1990.

[4]   A.E. Siegman, *LASERS*. Sausalito, CA: University Science Books, 1986.

[5]   J. R. Schneider *et al*. (2007, May 10). "The free electron laser in Hamburg," Deutsches Elektronen-Synchrotron [Online]. Available:http://pr.desy.de/e113/index_eng.html (accessed 20 Nov 09).

[6]   L. Merminga, D. R. Douglas, and G. A. Krafft. (2003, April). SRF-Based Energy-Recovering Linear Accelerators, Thomas Jefferson National Lab [Online]. Available:http://www.jlab.org/highlights/acc.html (accessed 02 Dec 09).

[7]   H. Bluem, A. M. M. Todd, and G. R. Neil, "Superconducting RF injector for high-power free electron lasers (FEL)," in *Proceedings of the 2001 Particle Accelerator Conference*, Chicago, IL, 2001.

[8]   B. Rusnak, RE: Y2K or Why 2 K? Available email: from brusnak@nps.edu (accessed 30 Nov 09).

[9]   "Unique properties of liquid He*,"* NHMFL Cryogenics Group, Florida State University [Online], Available:www.eng.fsu.edu/cryolab/Cryogens/helium.html (accessed 29 Nov 09).

[10]   W. F. Venon. (2004). "The physics of superfluid helium*,"* CERN Accelerator School: Superconductivity and Cryogenics for Accelerators and Detectors [Online]. Avaialble:http://documents.cern.ch/cgi-bin/setlink?base=cernrep&categ=Yellow_Report&id=2004-008 (accessed 30 Nov 09).

[11]   "Quadrupole," University of California Los Angeles, Particle Beam Physics Lab [Online]. Available:http://pbpl.physics.ucla.edu/Research/Technologies/Magnets/Electromagnets/Quadrupoles (accessed 1 Dec 09).

[12]   "What is the undulator," C-Band Corporation [Online]. Available:http://www-xfel.spring8.or.jp/cband/e/Undulator.htm (accessed 12 Jan 09).

[13]   R. Willingale. (2007). *"Lasers and quantum optics,"* University of Leicester, Department of Physics and Astronomy Lecture Notes [Online]. Available:http://www.star.le.ac.uk/~rw/courses/lect4313.html (accessed 11 Nov 09).

[14]   M. Wiseman, C. K. Sinclair, R. Whitney, and M. Zarecky. (1997). "High power electron beam dumps at CEBAF*," in 17th Particle Accelerator Conference*, Vancouver, Canada.

[15]   W. B. Colson, "Free electron lasers & accelerator physics," PH-4055 Class Notes: Naval Postgraduate School. Monterey, CA: 2009.

[16]   L. Andrews, and R. Phillips, "Laser beam propagation through random media." Bellingham, WA: SPIE Optical Engineering Press, 1998.

[17]   F. L. Pedrotti, and L. S. Pedrotti, "Introduction to optics," Second Edition. Upper Saddle River, NJ: Prentice Hall, 1993.

[18]   "Gaussian beam." Answer.com Web site, McGraw-Hill [Online]. Available:www.answers.com/topic/gaussian-beam (accessed 19 Jan 10).

[19]   H. Weichel, "Laser beam propagation in the atmosphere." Bellingham, WA: SPIE Optical Engineering Press1990.

[20]   R. Nave. (ND). "Blue sky and rayleigh scattering" [Online]. Available:http://hyperphysics.phy-astr.gsu.edu/Hbase/atmos/blusky.html (accessed 21 Jan 10).

[21]   D. J. Griffiths, *Introduction to Electrodynamics,* Third Edition. Upper Saddle River, NJ: Prentice Hall, 1999.

[22]   R. A. McClatchey and J. E. Selby. "Atmospheric attenuation of laser radiation from 0.76 to 31.25/um*,"* Air Force Cambridge Research Labs, Environmental Research Paper 460, Jan. 03, 1974.

[23]   "Absorption of electromagnetic radiation," AccessScience Web site, McGraw-Hill [Online]. Available:http://www.accessscience.com (accessed 22 Jan 10).

[24]   W. Colson, RE: blooming, Available e-mail: from wbcolson@nps.edu (accessed 28 Feb 10).

[25]   D. Leslie, and M. Belen'kii, "Wavelength selection and propagation analysis for shipboard free electron laser," in *SPIE,* vol. 5413, pp. 125–136, Bellingham, WA, 2004.

[26]   National Research Council of the National Academies, *Scientific Assessment of High-Power Free-Electron Laser Technology*. Washington, DC: The National Academies Press, 2001.

[27]   M. Capderou, *Satellites—Orbits and Missions*. Verlag, France: Springer, 2005.

[28]   O. Montenbruck and E. Gill, *Satellite Orbits—Models, Methods, and Applications*. Verlag, France: Springer Science & Business Media, 2005.

[29]   D. A. Vallado, *Fundamentals of Astrodynamics and Applications*, Second Edition. El Segundo, CA: Microcosm Press and Kluwer Academic Publishers, 2001.

[30]   "Regional Recovery of the Gravity Field from SST Observations," University of Stuttgart—Institute of Geodesy Web site [Online]. Available:http://www.uni-stuttgart.de/gi/research/projects/project8/index.en.html (accessed 03 Feb 10).

[31]   V. L. Pisacane, *Fundamentals of Space Systems,* Second Edition. Oxford, England: Oxford University Press, 2005.

[32]   T. Berger and B. Hajek. (2001). "The Space Radiation Environment" [Online]. http://www.ati.ac.at/~vanaweb/spacerad.html (accessed 09 Feb 10).

[33]   R. C. Olsen, *Remote Sensing From Air and Space*. Bellingham, WA: SPIE Optical Engineering Press, 2007.

[34]   R. C. Olsen, "Introduction to the Space Environment," PH-2514 Class Notes: Naval Postgraduate School, Monterey, CA, 2005.

[35]   C. C. Chao, *Applied Orbit Perturbation and Maintenance*. El Segundo, CA: The Aerospace Press, 2005.

[36]   A. Milani, A. M. Nobili, and P. Farinella, *Non-Gravitational Perturbations and Satellite Geodesy*. Bristol, England: Adam Hilger, 1987.

[37]   "Free electron laser," Office of Naval Research [Online]. Available:http://www.onr.navy.mil/en/Media-Center/Fact-Sheets/Free-Electron-Laser.aspx (accessed 20 Feb 10).

[38]   B. Leonard, "Spacecraft design I," AE-4870 Class Notes: Naval Postgraduate School, Monterey CA, 2009.

[39]   J. D. G. Rather, "Power beaming research at NASA," *SPIE, Intense Laser Beams,* vol. 1628, pp. 267–289, Bellingham, WA, 1992.

[40]   H. W. Friedman, "Near-term feasibility demonstration of laser power beaming," *SPIE, Laser Power Beaming*, vol. 2121, pp. 232–242, Bellingham, WA, 1994.

[41]   "Hubble Space Telescope," National Aeronautics and Space Administration [Online]. Available:http://hubble.nasa.gov/missions/sm3b.php (accessed 20 Feb 10).

[42]   B. N. Agrawal, *Design of Geosynchronous Spacecraft.* Englewood Cliffs, NJ: Prentice-Hall, 1986.

[43]   "Sunlight," Wikipedia [Online]. Available:http://en.wikipedia.org/wiki/Sunlight (accessed 08 Feb 10).

[44]   G. W. Zeiders, "Laser-powered orbital transfer," *SPIE*, vol. 2376, pp. 178–187, Bellingham, WA, 1995.

[45]   J. D. G. Rather, "Power beaming research at NASA," *SPIE,* vol. 1628, pp. 276–289, Bellingham, WA, 1992.

[46]   H. E. Bennett, "DOD and Navy applications for laser power beaming," *SPIE*, vol. 2376, pp. 21–30, Bellingham, WA, 1995.

[47]   U.S. Office of Science and Technology Policy, The National Science and Technology Council Committee on Transportation Research and Development, "Interagency report on orbital debris," pp. 19–39, Washington, D.C.: Government Printing Office, 1995.

[48]   National Aeronautics and Space Administration, Orbital Debris Program Office [Online]. Available:http://orbitaldebris.jsc.nasa.gov/index.html (accessed 22 Feb 10).

[49]   Committee on Space Debris, Aeronautics and Space Engineering Board, Commission on Engineering and Technical Systems, National Research Council, "Orbital Debris- A Technical Assessment." Washington, D.C.: National Academy Press, 1995.

[50]   W. S. Wolfner, "Orbital debris: cost impact on setting policy," Naval Postgraduate School, Monterey, CA, 1996.

[51]   National Aeronautics and Space Administration, *Orbital Debris Quarterly News*, v. 14, Issue 1, January 2010.

[52]   C. Phipps, "Orion: challenges and benefits," *SPIE*, vol. 3343, pp. 575–582, Bellingham, WA, 1998.

[53]   Campbell, J.W., "Project ORION: orbital debris removal using ground-based sensors and lasers," National Aeronautics and Space Administration, Technical Memorandum 108522, October 1996.

[54]   B. Goodrich, "Keck I pointing issues," *Keck Observer's Newsletter*, issue 4, pp. 9, Winter 2008.

[55]   N. Greene, "Mars closest approach to Earth in 50,000 years." About.com Web site, McGraw-Hill [Online]. Available:www.about.com (accessed 18 Mar 10).

[56]   "SETI overview," SETI Institute [Online]. Available:http://www.seti.org/Page.aspx?pid=1366 (accessed 28 Feb 10).

[57]   B. M. Oliver, "Some potentials of optical masers," in *Proceedings of the Institute of Radio Engineers*, 50, 135, 1962.

[58]   "Electromagnetic radiation," Wikipedia [Online]. Available:http://en.wikipedia.org (accessed 12 Feb 10).

[59]   S. P. Niles, Lieutenant Commander, United States Navy, private communication, 26 Feb 10.

[60]   J. Jimenez, Revised Version, Available e-mail: from jcjimene@nps.edu (accessed 26 Feb 10).

THIS PAGE INTENTIONALLY LEFT BLANK

INITIAL DISTRIBUTION LIST

1.   Defense Technical Information Center
      Ft. Belvoir, Virginia

2.   Dudley Knox Library
      Naval Postgraduate School
      Monterey, California